Visualization of vortex-lattice melting transition and transport current flow in $Bi_2Sr_2CaCu_2O_8$ with differential magneto-optical technique

Thesis presented for the degree of
Doctor of Philosophy
by

Alex Soibel

Supervisor: Prof. Eli Zeldov

Submitted to the Scientific Council of the
Weizmann Institute of Science
Rehovot, Israel

May 2001

Acknowledgements

I want thank those involved whose contribution to the current work can not be overestimated. First of all I want to thank my supervisor Prof. Eli Zeldov who provided the opportunity to join his group and start working on new fascinating project. His consistent guidance and stimulating assistance helped me to overcome the most difficult stages in the work and introduced me into a new field of physics. The most considerable is that Eli succeeded to make all time spent in his lab to be very pleasant.

I would like to thank Dr. Michael Rappaport for his great contribution to the construction of the magneto-optical system and for the willingness to discuss all technical issues. Special thanks to Dr. Yuri Myasoedov for his assistance in crystal preparation and his constant desire to help.

I want to express my gratitude to Prof. Tsuyoshi Tamegai and Dr. Shuuichi Ooi who supplied most of the crystals without which this research would be impossible to carry out.

I want to thank Dr. Marcin Konczykowski and Dr. C. J. van der Beek for a fruitful collaboration and a great time in Paris.

Special acknowledgment should be expressed to Dr. V. Geshkenbein and Dr. D. Feldman for the help with theoretical questions.

I appreciate the stimulating discussions with my examinators Dr. A. Stern and Dr. A. Yacoby.

Last, but not least, I want to thank all members of our group: Dr. D. Fuchs, Dr. B. Khaykovich, Y. Paltiel, N. Avraham, and Dr. S. Banerjee.

1. ***Preface***

The main goal of our research was the study of the first-order vortex-lattice melting transition in high-T_c superconductors. We have developed a novel differential method for magneto-optical imaging, which improves the field sensitivity of the technique by two orders of magnitude. The extremely high sensitivity of the developed differential method allows a direct two-dimensional imaging of the vortex-lattice melting process and visualizes complex nucleation and propagation of the transition. The images of the melting process reveal that the underlying disorder and inhomogeneities govern the properties of the vortex-lattice melting and result in the observed complex behavior. Furthermore, the properties of the transition vary significantly along the melting line due to the competing contributions of various types of disorder. In addition, we have visualized the flow of the transport current using differential magneto-optical imaging and have observed unexpected phenomena. Also the simultaneous magneto-optical and resistivity measurements provide a unique tool to study the correlation between the magnetic and the transport properties at the transition.

The thesis is organized in the following order: Section 2 presents a general introduction and the background to the research. Section 3 describes the experimental method and the description of the magneto-optical systems. A special attention is given to the explanation of the developed differential method and to the analyses of the factors limiting the field sensitivity. In Section 4 the main experimental results are discussed in three subsections. The first subsection shows the observed behavior of the vortex-lattice melting transition and explains the major role of disorder. The next subsection demonstrates the changes in the properties of the transition along the melting line due to the complex interplay of various types of disorder. The last subsection discusses how the introduction of the artificial disorder modifies the vortex-lattice melting. The attached appendices describe additional directions of our research. Appendix I analyzes a possible formation of laminar structure of solid-liquid domains in clean crystals due the intrinsic instability of the vortex-lattice melting. Appendix II shows the visualization of the transport current with differential magneto-optical technique. The correlation between the melting propagation, the

current flow, and the resistivity onset at the transition is discussed in Appendix III. The observed current redistribution near T_c is presented in Appendix IV.

2. Introduction

The high-T_c superconductors (HTSC) are type-II superconductors. The basic theory explaining the behavior of type-II superconductors in the presence of magnetic field was developed by Abrikosov[1] and is based on the Ginzburg-Landau theory[2]. It shows that the magnetic field above the first critical field H_{c1} penetrates into superconductor in a form of quantum magnetic flux lines or vortices. Each vortex contains one quantum of magnetic flux $\phi_0 = 2.07 \times 10^{-7}$ G cm^2. The superconductivity order parameter, which reflects the local density of the superconducting electrons, is suppressed in the vortex core of the size ξ, and the magnetic field of the vortex decays on the characteristic distance of the London penetration length λ. In type-II superconductors $k = \lambda/\xi > \sqrt{2}$ and is typically of the order of 100 in HTSC. The HTSC are also anisotropic superconductors with an anisotropy parameter $\varepsilon = \xi_c / \xi_{ab} = \lambda_{ab} / \lambda_c$, where ξ_{ab} and λ_{ab} are the parameters for vortex parallel to the c-axis of the crystal. The important parameters of $Bi_2Sr_2CaCu_2O_8$ crystals, which are the subject of current study, are $\lambda_{ab} \approx 2000$ • , $\xi_{ab} \approx 20 - 40$ • , $T_c = 90$ K, $\varepsilon \approx 1/150$.

Due to repulsive interactions, the vortices form a periodic hexagonal Abrikosov lattice. In conventional superconductors the vortex phase diagram was believed to consist of only one phase[1] – vortex lattice that exists between H_{c1} and H_{c2} (Fig. 2.1a). In HTSC thermal fluctuations play an important role and lead to a first-order vortex-lattice melting transition in clean systems. The long-range crystalline order of the solid phase is destroyed at the transition and a new vortex-liquid phase is formed[3] (Fig. 2.1b). The melting process can be understood in terms of a simplified cage model[4]. In this model, the vortex line is confined in a harmonic cage defined by intervortex interactions. The thermal fluctuations cause transverse deflections of the vortex line, the characteristic value $\langle r^2 \rangle$ of which can be calculated by comparing the energy $E(\langle r \rangle)$ associated with the transverse deflection of distance $\langle r \rangle$ and thermal energy $k_B T_m$. Melting occurs when the characteristic deflection reaches a certain fraction of the lattice constant, namely $\langle r^2 \rangle = (c_L a_0)^2$, where the Lindemann constant c_L is typically 0.10-0.15 and a_0 is the intervortex spacing. The resulting simplified equation of the melting transition is $B_m(T) = B_0(1-T/T_c)^2$, which has a negative slope of the melting curve and means that at higher fields the melting occurs at lower temperatures.

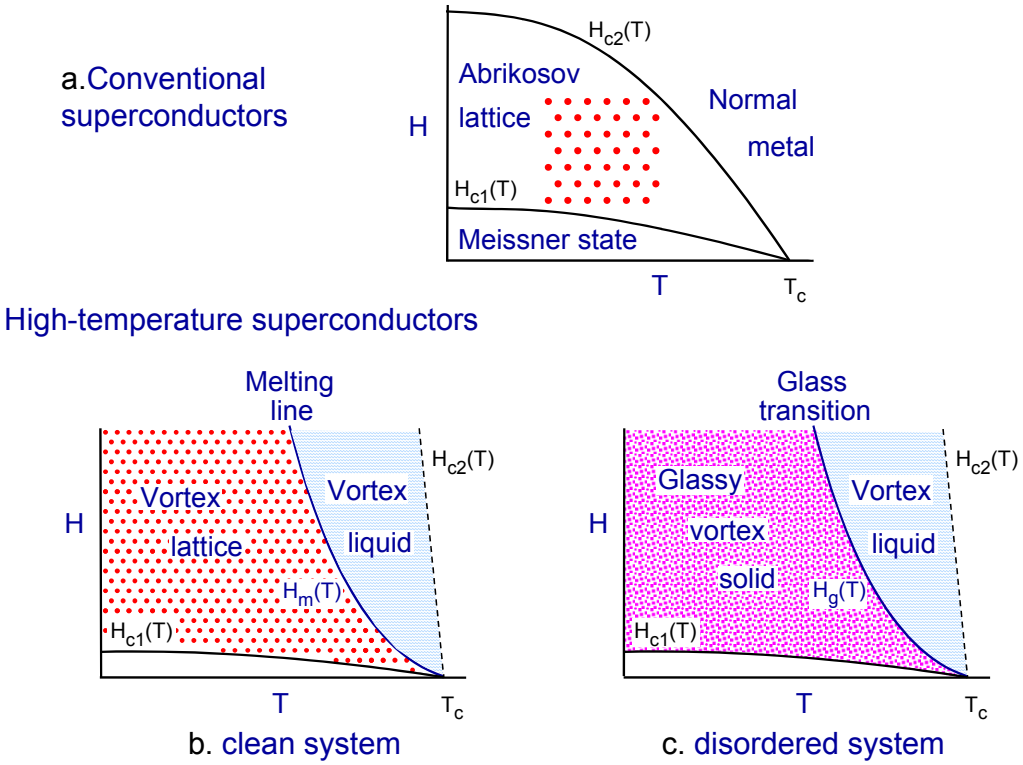

Figure 2.1. Theoretical *H-T* phase diagram of type-II superconductors. a) Low-T_c superconductor. b) HTSC without disorder. c) HTSC in the presence of strong disorder.

The vortex-lattice melting was first observed by resistivity measurements on clean $YBa_2Cu_3O_7$ crystals[5,6,7]. The current flowing in the superconductor exerts a Lorenz force on the vortices. The vortex motion induced by this force is the origin of the resistivity in type-II superconductors in the presence of magnetic field. Inhomogeneities and defects in the crystals can prevent motion of vortices since they act as pinning centers. The pinning is much more efficient in the solid phase than in the liquid, resulting in pronounced difference in resistivities of the two phases. A sharp drop to zero resistivity was observed in the experiments and it was associated with the vortex-lattice melting[5,6,7,8,9]. The drop occurs along a well-defined line on the *B-T* diagram and the onset of a hysteric behavior at the melting indicates the first-order nature of the transition[5,6,7,8,9]. The strong pinning in the vortex solid phase results in nonlinear current-voltage behavior observed in the experiments.

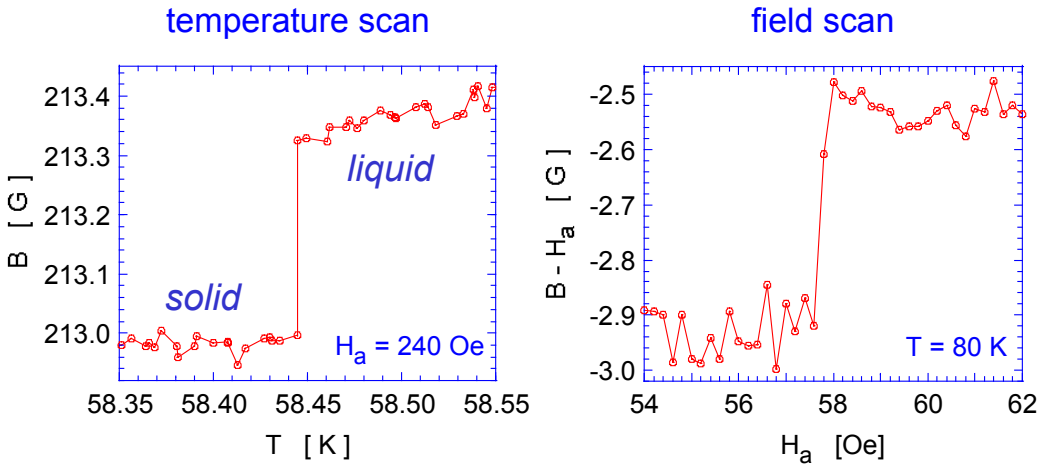

Figure 2.2. Magnetization step at the vortex-lattice melting in BSCCO measured with Hall sensor technique (from Zeldov, E. *et al.*, *Nature* **375**, 373 (1995)).

The first-order nature of the vortex-lattice melting was confirmed in thermodynamical measurements of the magnetization[10,11,12,13] and the latent heat[14,15]. The local magnetization exhibits a sharp step at the vortex-lattice melting in $Bi_2Sr_2CaCu_2O_8$ (BSCCO) as shown in Fig. 2.2. The local magnetization reflects a step of the local magnetic field or equivalently a change in the local vortex density, which is a direct manifestation of a first-order transition. The observed step in the local magnetic field ΔB depends on the quality of the crystal and is typically $\Delta B \approx 0.1$-0.4 G. The vortex density in the liquid phase is higher than in the solid, namely the vortices contract upon melting. Such behavior is very unusual and resembles ice that melts into water. This phenomenon follows from the negative slope of the melting line in the pressure (magnetic field) - temperature diagram, which in turn reflects the soft, long-range interaction nature of the logarithmic repulsion between vortices[4]. The Clausius-Clapeyron equation predicts $\frac{\partial p(T)}{\partial T} = \frac{\Delta s}{\Delta v}$, where p is the pressure (magnetic field) and $\Delta s = s_l - s_s$ and $\Delta v = v_l - v_s$ are the entropy and the volume differences per

particle between the liquid (l) and solid (s) phases across the transition. Since the liquid phase exists at higher temperature, the entropy of the liquid phase is higher than of the solid, and hence $\Delta s > 0$. If $\partial p(T)/\partial T$ is negative, then $\Delta v < 0$ and the liquid phase is denser than solid.

An important issue of the vortex lattice melting follows from the layered structure of HTSC. In the liquid phase, the wandering of the flux lines along the field direction is important. When the line wanders a distance equal to the intervotex spacing, the vortex lines become entangled. In the entangled state, the cutting and reconnection processes of the vortex lines are significant and govern the properties of the vortex phase. The entanglement length l_e depends on the temperature and on the applied magnetic field. When l_e becomes equal to the distance between two sets of CuO_2 planes, the longitudinal correlation of the flux line is lost and vortex segments in the different planes decouple. In this case, the liquid phase behaves as a set of planes of weakly interacting point-like pancake vortices[16]. Indeed the loss of the correlation along c-axis upon melting was observed in flux transformer[17,18] and Josehpson plasma resonance measurements[19,20,21], but still the question whether the vortices are entangled or decoupled (namely the size of l_e) remains open. Also the question of whether the decoupling and melting occur simultaneously or as two distinct transitions is still unclear.

In the discussion above we have considered a clean system and have neglected the influence of disorder on the phase diagram of the vortex matter. It has been predicted[22] that even the presence of weak disorder destroys the long-range crystalline order of the vortex lattice beyond the correlation length L_c, within which there is a long-range correlation. Since each region of vortices can move without considerable interaction with other regions, non-zero ohmic resistivity should be observed at any temperature. However, it has been argued[23,24] that a strong disorder transforms the vortex-lattice into a vortex glass phase. In the vortex glass the translational order decays exponentially and the disorder favors formation of dislocations[24]. In this model the vortices are not mobile and the ohmic linear resistivity should be zero due to diverging barriers. The vortex glass melts into a liquid through a continuos glass transition (Fig. 2.1c). Indeed, it was observed that introduction of an artificial disorder by ion or electron irradiation changes the order of the transition[25,26]. The sharp drop of the resistivity and the hysteresis disappear in the irradiated crystals, giving way to a

broad transition[25]. Also the magnetization step at the vortex-lattice melting is destroyed and gradual transformation between solid and liquid phase is observed[26].

In recent years a substantial progress has been made in the understanding of the properties of the vortex lattice in the presence of weak point disorder[27,28,29,30]. It has been demonstrated that disorder produces algebraic growth of displacements at short length scales, but periodicity takes over at large scales and the decay of the translational order is at most algebraic[29]. The quasi long-range order of this new glass phase survives due to the absence of dislocations and it exhibits Bragg peaks[31,32,33] similarly to a prefect lattice and therefore is named Bragg glass. This phase exists at low fields and undergoes a transition into another phase upon increasing the field, which could be liquid or another disordered glass (vortex glass). Since the Bragg glass is nearly as good as a perfect lattice as far as the transnational order is concerned, it should melt through first-order transition. The linear resistivity of Bragg glass vanishes at low temperature, since the vortex creep can occur only collectively.

Even the presence of weak disorder or small concentration of strong pinning centers can significantly modify the vortex-lattice melting. It has been demonstrated that irradiation with a very small dose does not change the order of transition but shifts the position of the melting on the phase diagram[34]. Change of the oxygen stoichiometry has a similar effect, it modifies the T_c and shifts the melting line[35]. The disorder should also have an important effect on the nucleation and propagation of the melting process. It is important to note that the behavior of the first-order transition in the presence of disorder is a general problem in condensed matter physics and is still poorly understood[36,37]. The vortex lattice has several experimental advantages for investigation of these phenomena on the microscopic as well as on the macroscopic scales since the temperature and particle density can be readily varied.

Figure 2.3 shows the experimental *B*-*T* phase diagram of the vortex matter in BSCCO plotted on logarithmic scale from few Gauss to 10 Tesla. Three distinct vortex phases can be clearly seen. The exact nature of the phases is still not clear but in general they are referred to as rather ordered solid (quasi-lattice), disordered solid, and liquid. The vortex-liquid phase can be either liquid of vortex line or a gas of pancake vortices. This phase diagram can be understood in terms of relevant energies[38,39], which are E_{pin}, E_{el} and E_T. E_{el} is the elastic energy of the lattice, E_{pin} is the energy describing the interaction of vortices with disorder-induced potential, and E_T is the thermal energy. The ordered solid phase is defined by $E_{el} > (E_{pin}, E_T)$, the

disordered solid exists when $E_{pin} > (E_{el}, E_T)$, and the thermal fluctuations are mainly important in the liquid phase $E_T > (E_{pin}, E_{el})$. The disordered solid apparently melts through a second order transition into a liquid phase when $E_{pin} = E_T$. The disorder-driven solid-entanglement transition happens when $E_{pin} = E_{el}$ and it was generally considered to be a second order transition which is seen as a second magnetization peak[35]. Recently, observation of the magnetization step at the transition has been reported, which indicates the first-order nature of the transition[40]. In our work we mainly concentrate on the first-order vortex-lattice melting at which a rather ordered solid melts into a liquid phase ($E_{el} = E_T$).

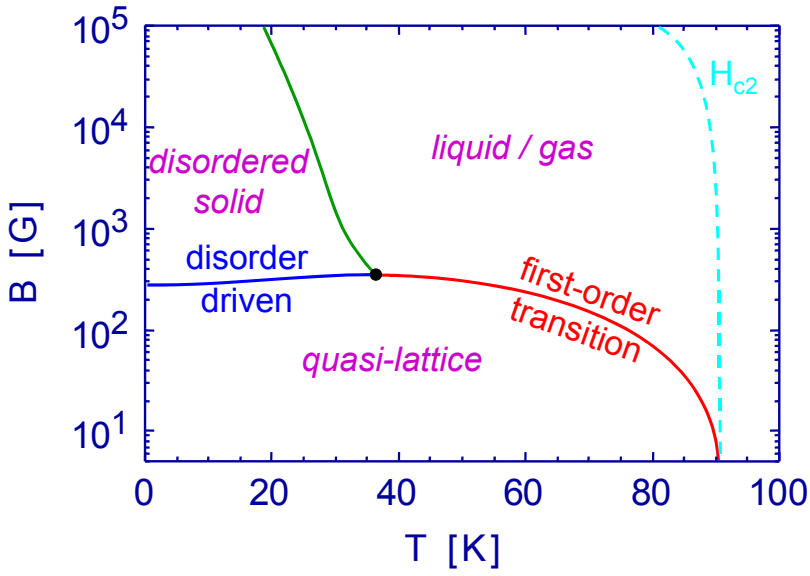

Figure 2.3. Experimental *B*-*T* phase diagram of the vortex matter in BSCCO.

3. Experimental

3.1 Magneto-optical technique

Most of the magneto-optical techniques for study of magnetic field distribution in superconductors are based on the Faraday effect. Farady effect is the ability of certain materials to rotate the polarization plane of the transmitted light in the presence of magnetic field. For a linearly polarized light propagating in the medium parallel to the direction of the magnetic field, the angle of rotation is given by $\alpha = V\,l\,B$, where V is Verdet constant defined by the medium and l is the thickness of the medium. The Fraday effect results from the change in the carrier motion induced by the applied magnetic field. In the presence of the magnetic field, the **k** vector of the carrier rotates around the Fermi sphere in the **k**-space. In regular space it corresponds to the orbital motion of the carriers in direction that is defined by the charge polarity of the carriers and the direction of the applied field. As a result, the propagation velocity of the light with left- and right-handed circular polarization is different. A linearly polarized light can be considered as a superposition of left- and right-handed circularly polarized waves. The phase shift between the waves, which results from the difference in the propagation velocity, causes the observed rotation of the polarization.

There are several extensive reviews of the development and application of magneto-optical techniques for study of superconductors[41]. Following is a summary of the principle of the magneto-optical technique and a description of the differential method that we have developed.

Figure 3.1 shows a schematic layout of the magneto-optical system. The magneto-optical indicator, which is a garnet film with an in-plane magnetization, is placed on top of the superconductor. A linearly polarized light is reflected from the bottom mirror of the indicator and undergoes Faraday rotation on passing through the indicator. The angle of rotation is proportional to the local magnetic field. After passing through the analyzer, that is set perpendicular to the polarizer, a real time optical image is obtained in which the local brightness is directly related to the value

of local magnetic field. The typical field sensitivity of such a system is several Gauss, which is not sufficient to observe the vortex-lattice melting.

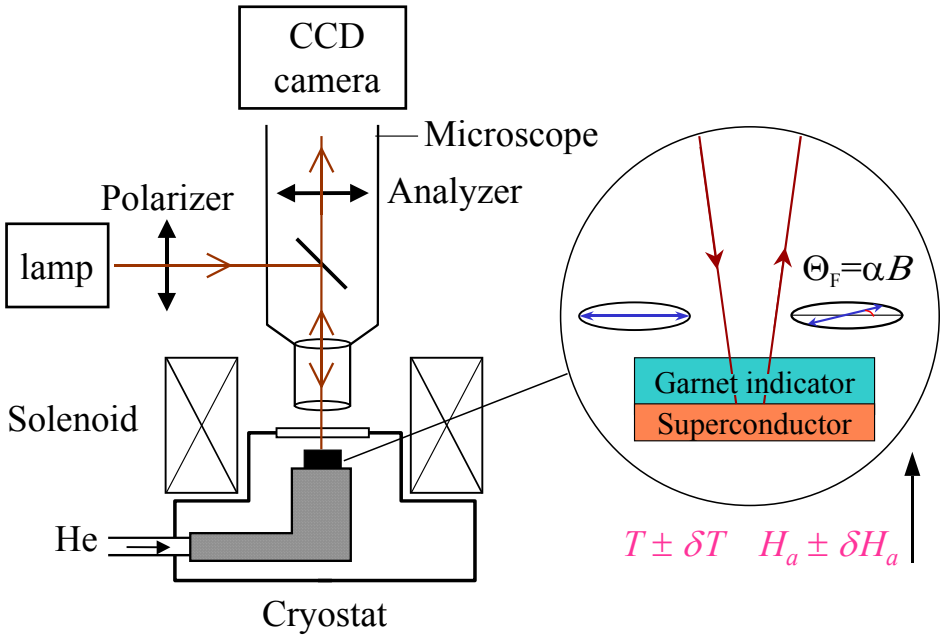

Figure 3.1. Schematic drawing of the magneto-optical system.

The magneto-optical indicator consists of a Bi-doped yttrium iron garnet film (YIG) grown by liquid phase epitaxy on a gallium-gadolinium-garnet (GGG) substrate and is coated by a reflective Al layer of several hundred nanometers. The Al mirror is covered by a thin protective layer of Al_2O_3 and we often evaporate an extra layer of TiO_2 to provide additional protection from scratches. The typical thickness of YIG layer is 6 μm, which allows to observe magnetic structures down to about 2 μm. The rotation angle of the polarization is proportional to the applied magnetic field up to the saturation field which is typically ranging between 500 and 1000 Oe. The characteristic value of rotation angle is 1 - 2 deg at H_a = 100 Oe which depends on the thickness of the indicator and Bi content and almost does not change with temperature in the range of interest, T = 4 - 100 K. The angle of rotation is strongly wavelength dependent with a maximum rotation at about 500 nm and we use a green filter in order to work with a monochromatic light at the maximum of the rotation.

3.2 Differential method for magneto-optical imaging

3.2.1 Experimental procedure

One of our main goals was magneto-optical visualization of the vortex-lattice melting transition. This task requires a field sensitivity that allows detection of local field variations of $\Delta B \approx 0.1$ G on a background field of several hundred Gauss. In order to achieve such high sensitivity we have developed the differential method. In this method we first fix the applied field and the temperature, and acquire a set of images and average them. Then the magnetic field or temperature is increased by a very small amount and another set of images is acquired and averaged. We than subtract the first averaged image from the second one and obtain the resulting differential image. This process is repeated and averaged typically 100 times in order to improve the signal to noise ratio. By a careful design and fabrication of the system we have achieved sensitivity as low as 30 mGauss, which is an improvement by more than two orders of magnitude as compared to conventional magneto-optical systems. By recording the differential images in a sequence of fields or temperatures a movie of the melting process is obtained.

3.2.2 Noise considerations

The field sensitivity of magneto-optical (MO) technique is typically several Gauss. The factors limiting the effective sensitivity of the MO imaging are mainly non-uniform illumination, differences in the CCD pixel response, inhomogeneity of the indicator, and dust that is always present on the optical parts of the system. For example, light intensity variation of 1% at $H_a = 200$ Oe corresponds to $\delta B \approx 1$ G. The influence of these extrinsic factors can be strongly reduced by applying the differential technique thus allowing to approach the fundamental intrinsic limits of the MO imaging.

The intrinsic noise in MO imaging is the photon shot noise. The main source of the shot noise in the differential MO imaging arises from the large background signal due to dc magnetic field H_a. First, we want to estimate the signal-to-noise S/N_0 of one captured frame, which is the ratio of vortex-lattice melting signal I_Δ and the shot noise I_s. At a given temperature, the vortex-lattice melting occurs at field H_a, which results in background signal

$$I_{count} = I_0 \sin^2(\alpha H_a) \approx I_0 (\alpha H_a)^2 \qquad \text{(Eq. 3.2.2.1)}$$

where I_{count} is the number of photons per pixel counted by the CCD camera, and I_0 is the coefficient defined by the light intensity, exposure time, etc. The angle of Farady rotation is αH_a, where α is the angle of rotation per unit field defined by the indicator sensitivity. If we increase the applied magnetic field by $\delta H_a << H_a$, the vortex lattice in some parts of the crystal will melt resulting in a step ΔB in the local magnetic field. The differential signal resulting from the vortex-lattice melting can be found as following. In the regions where the melting occurs due to the change of the magnetic field by δH_a, the differential signal is given by

$$I_{melt} = I_0 \sin^2[\alpha(H_a + \delta H_a + \Delta B)] - I_0 \sin^2[\alpha H_a] \approx 2 I_0 \alpha^2 H_a (\Delta B + \delta H_a).$$

In the regions without the melting transition, the differential signal is given by

$$I_{\text{nomelt}} = I_0 \sin^2[\alpha(H_a + \delta H_a)] - I_0 \sin^2[\alpha H_a] \approx 2 I_0 \alpha^2 H_a \delta H_a$$

We need to distinguish between the regions that melt and the regions that do not undergo the transition, and therefore the desired melting signal is given by

$$I_\Delta = I_{melt} - I_{\text{nomelt}} \approx 2 I_0 \alpha^2 H_a \Delta B, \qquad \text{(Eq. 3.2.2.2)}$$

while the shot noise is

$$I_s = \sqrt{I_{count}} \approx \alpha H_a \sqrt{I_0}\ . \qquad \text{(Eq. 3.2.2.3)}$$

The signal-to-noise ratio in one single frame:

$$S/N_0 = I_\Delta / I_s \approx \frac{2 I_0 \alpha^2 H_a \Delta B}{\alpha H_a \sqrt{I_0}} \approx 2 \Delta B \alpha \sqrt{I_0}\ . \qquad \text{(Eq. 3.2.2.4)}$$

The maximal possible I_{count} in one frame is defined by the full-well capacitance of the CCD pixel I_{fw}, which is about 4×10^4 electrons (or detected photons) in our camera. Substituting $I_{count} = I_{fw}$ in Eq. 3.2.2.1 and deriving I_0, we find

$$I_\Delta \approx \frac{2 \Delta B I_{fw}}{H_a} \quad \text{and} \quad S/N_0 \approx \frac{2 \Delta B \sqrt{I_{fw}}}{H_a}, \qquad \text{(Eq. 3.2.2.4)}$$

which gives $S/N_0 \approx 0.5$ for typical values of $H_a = 150$ Oe and $\Delta B = 0.2$ G. Thus, in a single frame, the shot noise is higher than the signal of interest and additional averaging is required in order to improve the signal-to-noise ratio.

The signal-to-noise ratio in the averaged image is $S/N_N = \sqrt{N} \times S/N_o$, where N is the number of the averaged frames and S/N_o is the signal-to-noise of a single frame at the full-well capacity. In the discussed case of $H_a = 150$ Oe, we need to average $N \approx 400$ frames in order to achieve $S/N_N = 10$ or equivalently noise level of 20mGauss.

We can estimate how long does it take to obtain the desired signal-to-noise ratio. From Eq. 3.2.2.1

$$I_{fw} \approx I_0 (\alpha H_a)^2 \approx \gamma W \tau (\alpha H_a)^2 \qquad \text{(Eq. 3.2.2.5)}$$

where W is number of photons reaching a single pixel per unit time for parallel configuration of the polarizer and analyzer, γ is the quantum efficiency of the CCD and τ is the exposure time. Thus the exposure time necessary for reaching the full-well capacity is

$$\tau \approx \frac{I_{fw}}{\gamma W (\alpha H_a)^2}. \qquad \text{(Eq. 3.2.2.6)}$$

The minimal exposure time is limited by $\tau_{min} = 1/f_{max}$, where f_{max} is the maximal frame rate of the camera. The maximum field, which can be applied for reaching the full-well capacitance of the CCD during the minimal exposure time

$$H_{max} = \sqrt{\frac{f_{\max} I_{fw}}{\gamma W \alpha^2}}. \qquad \text{(Eq. 3.2.2.7)}$$

At $H_a > H_{max}$ attenuation filters are therefore required to be inserted into the microscope in order to adjust the intensity of the light W and to avoid pixel saturation.

The light intensity that reaches the CCD of the camera is measured to be of the order of 0.5 mWatt or equivalently $W \approx 1\times10^9$ photons/pixel sec for our CCD of 1024×1024 pixels. Taking the typical value of $\alpha = 4\times10^{-4}$ rad/Oe, quantum efficiency of our camera for green light $\gamma \approx 0.08$, and $f_{max} = 5$ Hz, we can find $H_{max} \approx 150$ Oe. This value is in good agreement with our experimental evaluation $H_{max} \approx$ 100-250 Oe.

Next, we want to find how the time of the experiment t depends on the applied magnetic field H_a at fixed parameters of the indicator and intensity of illumination. From Eqs. 3.2.2.6 and 3.2.2.7 the exposure time is given by:

$$\tau = \frac{1}{f_{\max}} \left(\frac{H_{\max}}{H_a} \right)^2 \ (H_a < H_{max}) \quad \text{or} \quad \tau = \frac{1}{f_{\max}} \ (H_a \geq H_{max}) \qquad \text{(Eq. 3.2.2.8)}$$

The time of the measurement t is given:

$$t = 2\tau N = 2\tau \left(\frac{S/N_N}{S/N_0} \right)^2 \qquad \text{(Eq. 3.2.2.9)}$$

From Eqs. 3.2.2.4, 3.2.2.6 and 3.2.2.8 follows:

$$t_{low} \approx \frac{(S/N_N)^2}{2\gamma W (\alpha \Delta B)^2} \approx (S/N_N)^2 \left(\frac{H_{\max}^2}{2 f_{\max} (\Delta B)^2 I_{fw}} \right) \ (H_a < H_{max}) \qquad \text{(Eq. 3.2.2.10a)}$$

$$t_{high} \approx (S/N_N)^2 \frac{H_a^2}{2 f_{\max} (\Delta B)^2 I_{fw}} = t_{low} \left(\frac{H_a}{H_{\max}} \right)^2 \quad (H_a \geq H_{max}) \quad \text{(Eq. 3.2.2.10b)}$$

The resulting time t to get $S/N_N = 10$ (or noise level 20 mGauss) is plotted vs. H_a in Fig. 3.2.1. For $H_a < H_{max}$ the t (we call it t_{low}) does not depend on the applied magnetic field, while for $H_a > H_{max}$ the required measurement time increases quiadratically with the field. The independence of the measurement time on H_a at low fields follows from the following simple argument. The required number of frames N to achieve the desired S/N is proportional H_a^2, while the time to acquire a frame at the full-well capacity $\tau \propto 1/H_a^2$, which implies that the resulting time of experiment $t = N\tau$ does not depend on H_a. At high fields the required number of frames N is still proportional to H_a^2 while τ is limited by the frame rate of the camera, resulting in $t \propto H_a^2$. Equation 3.2.2.10 also underlines the specifications of the camera which are important for the differential magneto-optical imaging in various regimes. At low fields, the quantum efficiency of the CCD, the light intensity, and the Faraday rotation of the indicator determine the time of the experiment, while at high fields the limiting factors are the full-well capacitance and the frame rate of the camera.

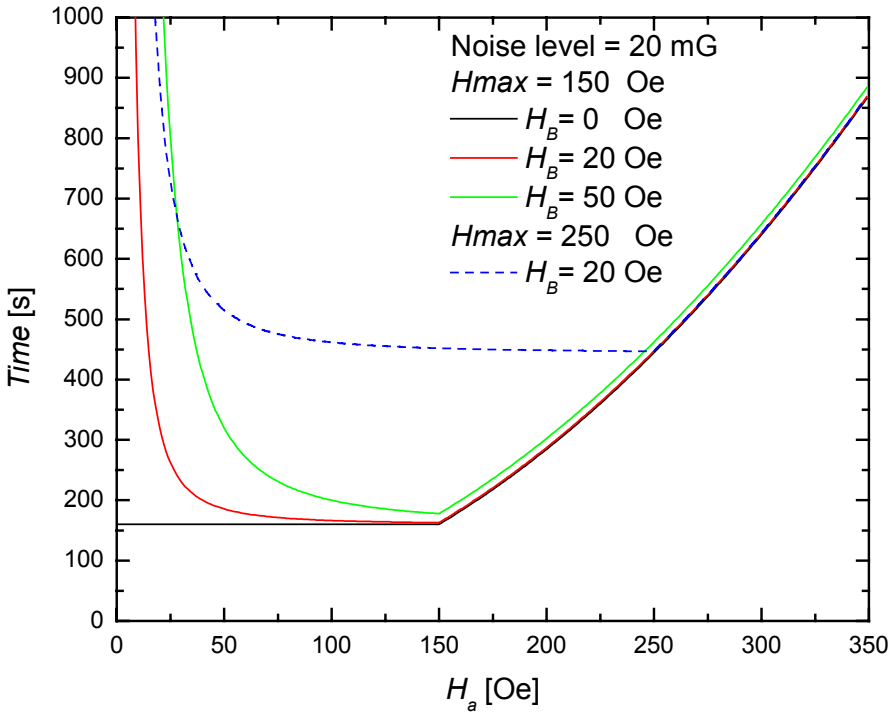

Figure 3.2.1. Estimated time of measurement to achieve shot noise level of 20 mGauss vs. applied magnetic field.

The above simple estimate neglects other sources of noise like the read-out noise of the camera, dark current, etc., that increase the required time of averaging. Another important factor that limits the signal-to-noise ratio at low fields is the presence of a parasitic background signal at zero applied magnetic field. This signal results mainly from the rotation of the light polarization induced by the cryostat window and the optical components of the microscope. We can associate this background signal I_B with the effective magnetic field H_B, such that $I_{count} = I_0 \sin^2(\alpha H_a) + I_B = I_0 [\sin^2(\alpha H_a) + \sin^2(\alpha H_B)]$. From our measurements we estimate $H_B \approx 10$ - 50 Oe. Repeating the calculation we obtain:

$$S / N_0^B \approx I_\Delta / I_s \approx \frac{2\Delta B \sqrt{I_{fw}}}{H_a} \frac{H_a^2}{H_a^2 + H_B^2} \approx S/N_o \frac{H_a^2}{H_a^2 + H_B^2}, \quad \text{(Eq. 3.2.2.11)}$$

$$\tau_B = \tau \left(\frac{H_a^2}{H_a^2 + H_B^2} \right) \quad \text{and} \quad t_B = t \left(\frac{H_a^2 + H_B^2}{H_a^2} \right) \quad \text{(Eq. 3.2.2.12)}$$

where t, τ, and S/N_0 are the time of the measurement, exposure time, and the signal-to-noise ratio at $I_B = 0$ as calculated above. The resulting t_B for $H_B = 10$ and 40 Oe is plotted in Fig. 3.2.1. The presence of the background signal strongly increases the required time of the experiment at low fields.

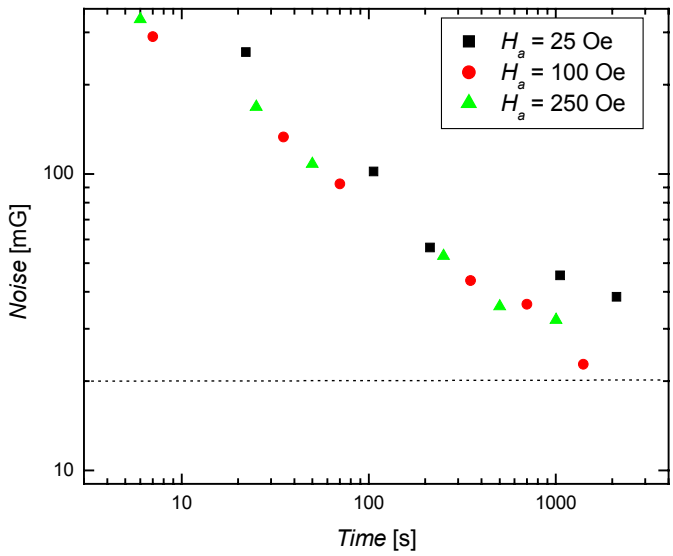

Figure 3.2.2. The measured noise vs. time of the measurement at $H_a = 25$, 100, and 250 Oe. The dotted line shows the noise level of 20 mGauss.

Figure 3.2.2 shows the measured noise in the differential images vs. time of the measurement at different applied fields H_a = 25, 100, and 250 Oe. The noise decreases as a square root of the time as expected. The noise is maximal at H_a = 25 Oe, which indicates the strong influence of the background signal I_B. The almost equal noise level at H_a = 100 and 250 Oe reflects the high value of $H_{max} \approx 250$ Oe and implies that the number of photons counted by the camera per unit time is less than estimated from the illumination intensity. The estimated time of the measurement at low fields $H_a < H_{max}$ increases with H_{max} according to Eq. 3.2.2.10a and the time calculated for H_{max} = 250 Oe (dotted line in Fig. 3.2.1) is in the better agreement with the experimental results plotted in Fig. 3.2.2.

3.2.3 Differential MO imaging with temperature modulation

At temperatures below about 55 K the increase in vortex pinning results in long relaxation times of the magnetic field inside the samples and makes the field modulation ineffective for performing differential imaging. In order to perform the measurements at low temperatures, we have introduced small temperature modulation instead of field modulation. It is more difficult technically to modulate the temperature of the sample than the applied field. We have therefore fabricated a small copper sample holder with incorporated AlGaAs temperature sensor and a wound heater, which allows an accurate temperature control. In order to ensure a reliable thermal contact, the sapphire substrate with the crystal are glued to the sample holder using silver paint, which has excellent thermal conductivity at low temperatures. Since the temperature of the sample holder is regulated separately from the temperature of the cold finger of the cryostat, the thermal coupling between them should be low. It was achieved by incorporating a thin layer of nanodecan between the sample holder and the cold finger, which has a medium thermal conductivity. The temperature difference between the sample holder and the cold finger is ΔT = 1 - 3 K when the heater is off, and can reach ΔT = 10 – 15 K with the heater active. The temperatures of the sample holder and the cold finger are maintained independently by two temperature controllers, LakeShore 340, that allow variation of the sample temperature without changing the temperature of the cold finger. In order to obtain a differential image the temperature of the sample holder is modulated by δT, and the corresponding differential image is acquired using a procedure similar to δH_a

modulation described in section 3.2.1. This set-up with two independent temperature controllers in combination with helium transfer system, which keeps the helium flow constant, allows achieving temperature stability of few mK. In order to measure the melting process as a function of temperature, the temperatures of the cold finger and the sample holder are varied simultaneously while maintaining the desired temperature difference between them.

3.2.4 Visualization of the transport current with MO technique (self-field measurements)

We have applied the differential magneto-optical technique to study the transport current flow in high-T_c superconductors. The developed method is a very powerful tool for such investigation since it provides a two-dimensional visualization of the flow of small transport currents with extremely high resolution that is not available in other techniques. The current flow can be visualized by differential MO technique as following. The difference between the magneto-optical images taken with and without the current flowing in the crystal provides an image of the self-induced magnetic field generated by the current. The two-dimensional current flow can be derived from the self-field by inversion of the Biot-Savart law[42,43,44]. In fact, in our experiments the image of self-field is obtained from difference between the magneto-optical images taken with a positive and a negative current flowing in the crystal. This procedure prevents possible artifact, which may result from sample heating by the current. We have also visualized the second derivative of the self-field which can be found as SecondDerivative = [Image(Positive Current) - Image(noCurrent)] + [Image(Negative Current) - Image(noCurrent)]/2.

3.2.5 Calibration of self-field or temperature modulation images

The differential MO images of self-field or of temperature modulation are calibrated in order to derive magnetic field values from the grayscale of MO image. For this calibration, an additional differential image is acquired in which the magnetic field is modulated by a known amount δH_a (typically δH_a = 1 Oe). This image

provides a grayscale reference which corresponds to a change in the local magnetic field $\delta B = \delta H_a$. The signal is given by Eq. 3.2.2.2:

$$I_{\delta H} = 2I_0 \alpha^2 H_{aH} \delta H_a, \qquad \text{(Eq. 3.2.5.1)}$$

where H_{aH} is the dc field at which the reference image is taken. The remaining images can than be calibrated according to:

$$\delta B = \frac{I_{image}}{I_{\delta H}} \frac{H_{aH}}{H_a} \delta H_a, \qquad \text{(Eq. 3.2.5.2)}$$

where I_{image} is the image to be calibrated and H_a is the dc field at which the image was acquired.

3.3 Experimental set-up

3.3.1 Optical cryostat

The optical cryostat is a modified RC102 continuous flow cryostat manufactured by CRYO Industries of America. The cryostat is made of stainless steel and has inner cold part made of cooper and surrounded by aluminum radiation shield. A wound heater and AlGaAs temperature sensor are mounted at the end of the cold part near the sample space. We have replaced the cold finger in the sample space with a home-made one, which extends above the plane of the cryostat and into the tube of the cover lid. The crystals are mounted in the center of an electro-magnet coil. A 44-pin chip carrier socket is mounted at the top of the cold finger and wired to two standard 26-pin connectors that allow to perform simultaneous MO and transport or Hall sensor measurements. The wires are wound around the cold finger and the cold part of the cryostat in order to reduce thermal coupling. The cover lid is also home-made and has a central tube that surrounds the cold finger. A fused silica window with AR coating manufactured by VLOC is mounted on the top of the lid tube using an O-ring and a clamp.

3.3.2 Helium transfer and control system

We use a standard helium storage vessel containing 110 liters, which allows up to five days of continuos measurements. The helium is transferred to the cryostat using a transfer line and it exits through a flow meter into the helium recovery line.

The flow meter is equipped with control valve, which allows a fine tuning of the helium flow in addition to the main valve of the transfer tube. A steady helium flow is achieved by keeping the gas pressure in the vessel on a level of 3-5 psi, which is maintained by a pressure release valve connecting the vessel to the recovery line. The helium flow is kept constant during the measurement and is monitored by the flow meter.

3.3.3 Microscope

We use commercial Leica DMR microscope designed for work with polarized light. The objectives (x2.5, x5 and x10) are objectives for polarized light which were specially inspected to be strain-free and have a long-working distance. The beamsplitter is a Smith prism, which gives optimal extinction for the vertical or horizontal polarization of the incident light. The microscope is equipped with two light sources - halogen lamp and mercury lamp, which is controlled by a stabilized power supply. All the measurements are performed with the mercury lamp, which has strong radiation lines in green. The microscope is equipped with three green filters of different bandwidth and a hot mirror which blocks the UV and IR radiation and protects the polarizes and the optics.

3.3.4 CCD camera

The CCD camera is a cooled, digital, frame-transfer Pluto camera made by PixelVision. The CCD chip has 2048x1028 pixels (1024x1024 active pixels) and the pixel size is $12\times12\mu m^2$ square. The chip is thermoelectrically cooled down to $-32\ ^0C$. The image is digitized by four 14-bit ADC converters located on the chip and transferred by 4 fiber-optical cables to the computer. The camera is able to acquire up to 32 frames per second, but in this regime the noise is extremely high resulting in the maximal practical rate of 5 frames per second.

3.3.5 Electro-magnet

The external magnetic field is created by water-cooled copper wire coil. The coil has two windings: internal (25 Oe/A) and external (225 Oe/A), calibrated by

commercial Toshiba sensor in the center of the coil. The internal winding is used to make small field modulation and the external serves as a source of dc magnetic field. The windings are driven by separarte current sources and work independently. The water cooling allows to perform long measurements with magnetic field of up to 600 Oe without substantial heating of the coil. The copper bore that supports the coil windings was cut vertically and glued back with insulating glue. The vertical cut prevents generation of Eddy currents, which may otherwise screen AC magnetic field generated by the inner coil.

3.3.6 Electronics

The MO system has electronic equipment, which allows performing simultaneous magneto-optical and electrical measurements in a wide range of temperatures and applied magnetic fields. The temperature of the cryostat and the MO sample holder are controlled by two LakeShore340 temperature controllers. The power supply for the external winding of the coil is Yokogawa 7651, which controls Toelner 8751. The internal winding is driven by Yokogawa 7651. Valhalla, which is controlled by SR850 lock-in amplifier and Yokogawa 7651 voltage source, is used as a source for the transport current in the crystal. The SR850 lock-in amplifier is used to measure the resistivity of the crystal.

3.3.7 Data acquisition and processing

The instruments and camera are controlled using LabView program through GPIB interface or by calling a DLL (camera). All measurements are carried out automatically by executing LabView programs, namely the experiments may perform over several days without a need for human intervention. The acquired MO images are saved as 16-bit TIF files. Additional image processing is performed after the measurement, which includes filtering, illumination correction, calibration (for temperature modulation and self-field measurements) and the final image is saved as 8 bit file. The final image can be analyzed using Photoshop and Image-Pro software packages and the movie of the melting process is created from the images at sequence of fields or temperatures using Ulead Video Studio or Fast Movie Processor software.

3.4 Heavy ion irradiation

We have irradiated BSCCO crystals by high-energy heavy ions in order to create localized regions of pinning centers. The irradiation was performed at GANIL heavy-ion accelerator using 1 GeV Pb ions, which are known to produce columnar defects along the ion trajectory within the sample[45]. Prior to irradiation, the samples were covered by a metallic mask designed to restrict the pinning centers only to some defined locations (Fig. 3.4). The desired thickness of the masks and the crystals was determined by Monte-Carlo simulation code TRIM[46] in such way, that the mask blocks the irradiation completely while in the unmasked regions the ions pass through the crystal without changing their trajectory.

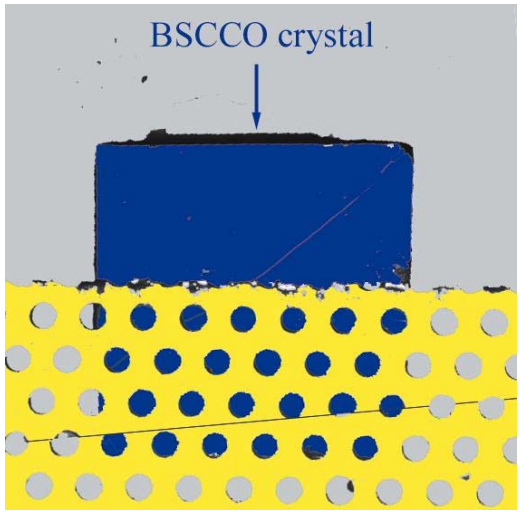

Figure 3.4. Image of a BSCCO crystal, colored in blue, which is covered by a special mask for evaporation (yellow).

3.5 Fabrication of the electrical contacts

We have developed a method of fabrication of thin metallic contacts on the top of the crystals, which do not disturb the magneto-optical imaging. Freshly cleaved BSCCO crystals are glued to sapphire substrate with pre-evaporated contact pads. The glue is applied specifically to provide effective planarization of the structure. The crystal is covered by a shadow mask, which is fabricated using photolithography and etching and includes designed pattern for the contacts. A thin gold layer is evaporated through the mask that creates electrical contacts on the top of the crystal and connects them to the pads on the sapphire. The pads are wired to the 44-pin holder by bonding technique and the resistance of the contacts is typically less than several Ohm. BSCCO crystal with evaporated gold contacts is shown in Fig. 3.5.

Figure 3.5. Image of a BSCCO crystal, colored in blue, with evaporated golden contacts on the top (yellow).

4. Experimental results and discussion

4.1 Visualization of the vortex-lattice melting in BSCCO crystals

4.1.1 Predicted melting behavior in clean system

We address initially the expected 'mean-field' vortex-lattice melting process in the absence of disorder. Under equilibrium magnetization conditions in a thin platelet-shaped sample in perpendicular applied field $H_a||z$, the internal fields $B(x,y)$ and $H(x,y)$ across the sample have a dome-shaped profile with a maximum at the center and a minimum near the edges[47]. This is due to the fact that in this geometry, in the absence of bulk pinning, the equilibrium shielding currents flow only along the sample edges. The melting transition occurs when the local field reaches some characteristic value $H_m(T)$. As the applied field or temperature is increased the field in the central part of the sample reaches $H_m(T)$ first. As a result a small round 'puddle' of vortex liquid should be formed in the center, surrounded by vortex solid. Due to the first-order nature of the transition, the vortex-lattice melting is associated with a discontinuous step in the equilibrium magnetization, $4\pi\Delta M=\Delta(B-H)$. Since in our geometry the field H is continuous across the solid-liquid interface, the field B in the vortex liquid is thus enhanced by ΔB relative to the solid. In BSCCO crystals ΔB is typically 0.1 to 0.4 G.

In the ideal case, as the field is increased by δH_a, the radius of the vortex-liquid puddle in the center of the sample should increase by δR, determined by the gradient of the dome-shaped profile $H(x,y)$. The differential image in this case should show a bright ring on a dark background, which indicates the location of the expanding solid-liquid interface (Fig. 4.1.1). In the rest of the image almost no change in the field should occur, except the uniform background signal of δH_a. The intensity of the ring is ΔB above the background[48], independent of δH_a, whereas the width of the ring reflects the distance δR over which the interface expands due to field modulation δH_a. Some additional small broadening of the ring occurs due to the finite thickness (6 μm) of the MO indicator. Note that the described process is the expected equilibrium coexistence of the solid and liquid phases. This phase separation is a result of the intrinsic gradient of the internal field, which is equivalent to a chemical potential gradient, and is similar to the phase separation of water and ice in the

presence of a gravitational field. Ice floats on top of the water and both phases are in equilibrium at the same temperature but there is a pressure gradient from the top to the bottom. Here we have a vortex liquid puddle floating inside a solid due to the dome-shaped equivalent chemical potential. As described below, however, we observe that the phase separation is governed by disorder, and that the dome-shaped field profile is of secondary importance and mainly results in a delay of melting near the sample edges. The equilibrium phase separation differs from the nonequilibrium dynamic nucleation and growth in the case of supercooling or superheating. We discuss first the equilibrium behavior, and then address the specific features related to supercooling and hysteresis.

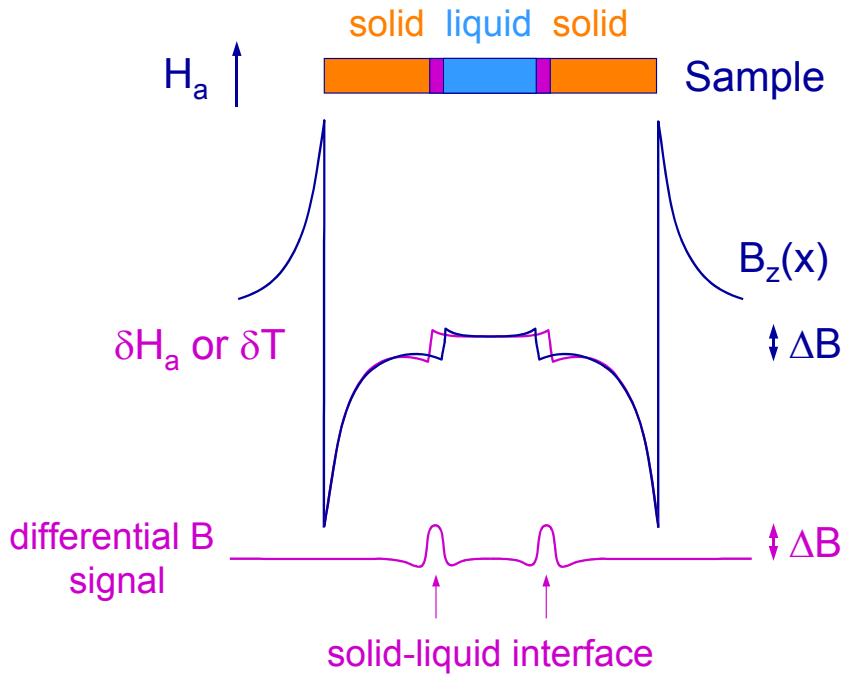

Figure 4.1.1. Schematic illustration of differential magneto-optical visualization of vortex-lattice melting.

4.1.2 Melting propagation in BSCCO crystal

We have investigated a number of high quality BSCCO crystals ($T_c \approx 91$ K) that show almost perfect critical state flux penetration at low temperatures in the MO images. The crystals were grown by the traveling solvent zone method and most of

the crystals were obtained from Tokyo University[49] and some from Leiden University[50]. Figure 4.1.2.1 shows several differential magneto-optical images of the vortex lattice melting process in a BSCCO crystal of area 0.35 × 0.27 mm^2 at T=60 K. (The movies of the melting process can be seen at http://www.weizmann.ac.il/home/fnsup). The gray scale reflects the field intensity which spans about 0.2 G from black (low) to white (high). The region outside the sample is bright. The differential images are obtained by subtracting the image at field H_a-δH_a/2 from the image at H_a+δH_a/2, with δH_a=1 Oe. At H_a = 159.0 Oe the entire sample is in the vortex solid phase. As the field is increased to 159.5 Oe a small liquid puddle is nucleated, seen as a bright spot in the upper-right part. Note that in contrast to expectations, the puddle is not in the center of the sample, nor is it round, but instead a rather rough shape of the vortex liquid domain is observed. These irregularities are found in the all investigated samples.

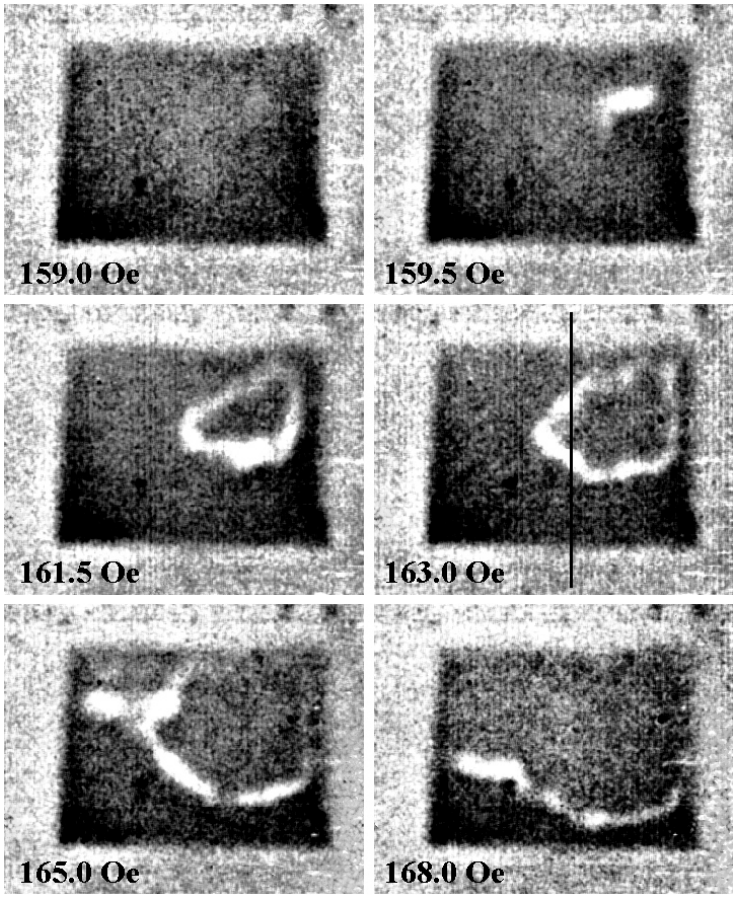

Figure 4.1.2.1. Differential MO images of the melting process in a BSCCO crystal (T_c=91 K) of area 0.35 × 0.27 mm^2 at T=60 K, δH_a=1 Oe and H_a || c-axis.

As the field is increased to 161.5 and 163.0 Oe, a ring-like bright object is obtained. This is the solid-liquid interface separating the liquid from the surrounding vortex solid phase. Differential-field profile across the ring (black line) of the 163.0 Oe image is shown in Fig. 4.1.2.2. The intensity of the solid-liquid interface signal reflects the height of the magnetization step at the FOT, $\Delta B \approx 0.15$ G in this sample. The shape of the ring is irregular, and moreover, the ring width is highly nonuniform. At 165 Oe a 'tongue' of the liquid protrudes sharply to the left side. By 168 Oe the upper part of the sample is entirely in the liquid phase, with a rough interface separating the liquid from the narrow solid region at the bottom. In our measurements we took the data during the sweep up and down of the magnetic field. By comparing the images at sweep up and down (not shown) we found the melting patterns at corresponding fields are almost identical which indicates the reversibility of the melting process (see §4.1.7 for non-equilibrium effects).

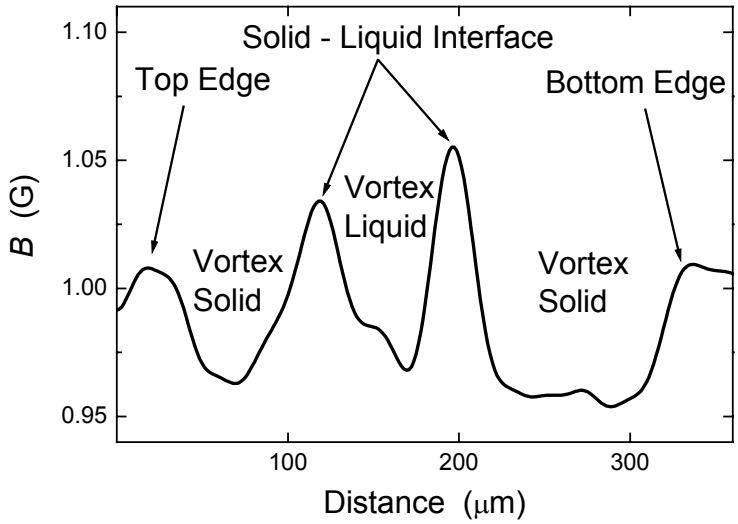

Figure 4.1.2.2. Differential-field profile across the crystal through the melting ring of the 163.0 Oe image (black line in Fig. 4.1.2.1).

Figure 4.1.2.3 shows more clearly the corresponding outer contours of the liquid phase at a series of applied fields at 0.5 Oe intervals. The solid-liquid interface displays a high degree of corrugation. The contours overlap in various regions showing the places where the interface is pinned whereas a large separation between contours indicates regions with high interface mobility. As H_a is increased from 159.5

(red) to 160.0 Oe (yellow), for example, the interface remains pinned at the right and left edges, but expands upwards and downwards. The upper part then remains pinned at 160.5 (green) and 161.0 Oe (cyan), then expands abruptly at 161.5 Oe and gets pinned again at 162.0 Oe. So instead of expanding uniformly, the liquid appears to expand by a sequence of abrupt local protrusions and pinning.

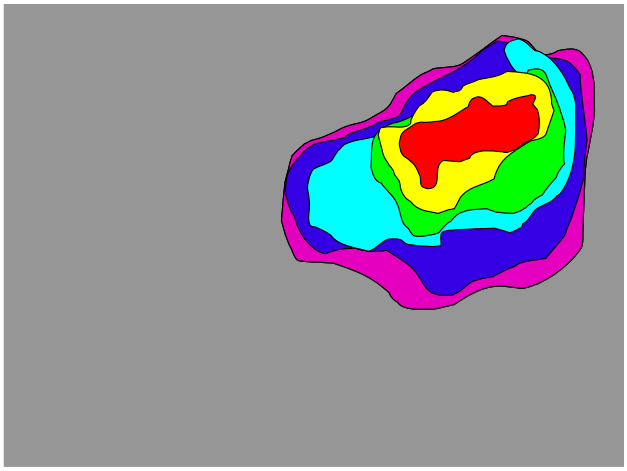

Figure 4.1.2.3. Contours of the expanding liquid phase at H_a = 159.5, 160.0, 160.5, 161.0, 161.5 and 162.0 Oe.

4.1.3 Melting propagation in crystal #5

Figure 4.1.3 shows the melting propagation in a crystal with an extended defect in a form of a step in the thickness. The upper part of the crystal is thicker than the lower one. The vortex solid and liquid regions have been colored artificially in brown and blue, respectively, for clarity. The procedure for introducing the color is as following. First, a threshold function is applied to create 1-bit image of melting contours from the differential image. In the 1-bit image pixels have value of 1 in the areas where melting happens in the corresponding differential image, and 0 otherwise. This assignment is the most sophisticated part of the analysis and usually requires

additional image processing. After the differential melting contours for each image have been determined, the area of the liquid phase at a given field (temperature) is found by performing consecutive logical sum (OR operation) of the differential melting contours at fields (temperatures) below the field (temperature) of interest. The final color image is created in HSB (hue, saturation, brightness) mode. The values of hue (color) are selected to designate solid and liquid, which are usually brown for solid and blue for liquid. The final HSB pixel value is set in the following way – hue is defined by the contour image of the liquid area (hue of solid or liquid), saturation is 100%, and brightness is given by the original differential image. Such procedure allows coloring of solid and liquid areas while preserving the original information of the differential image. The different stages of the process are made using IMAQ vision, PhotoShop, and Image-Pro Plus software packages.

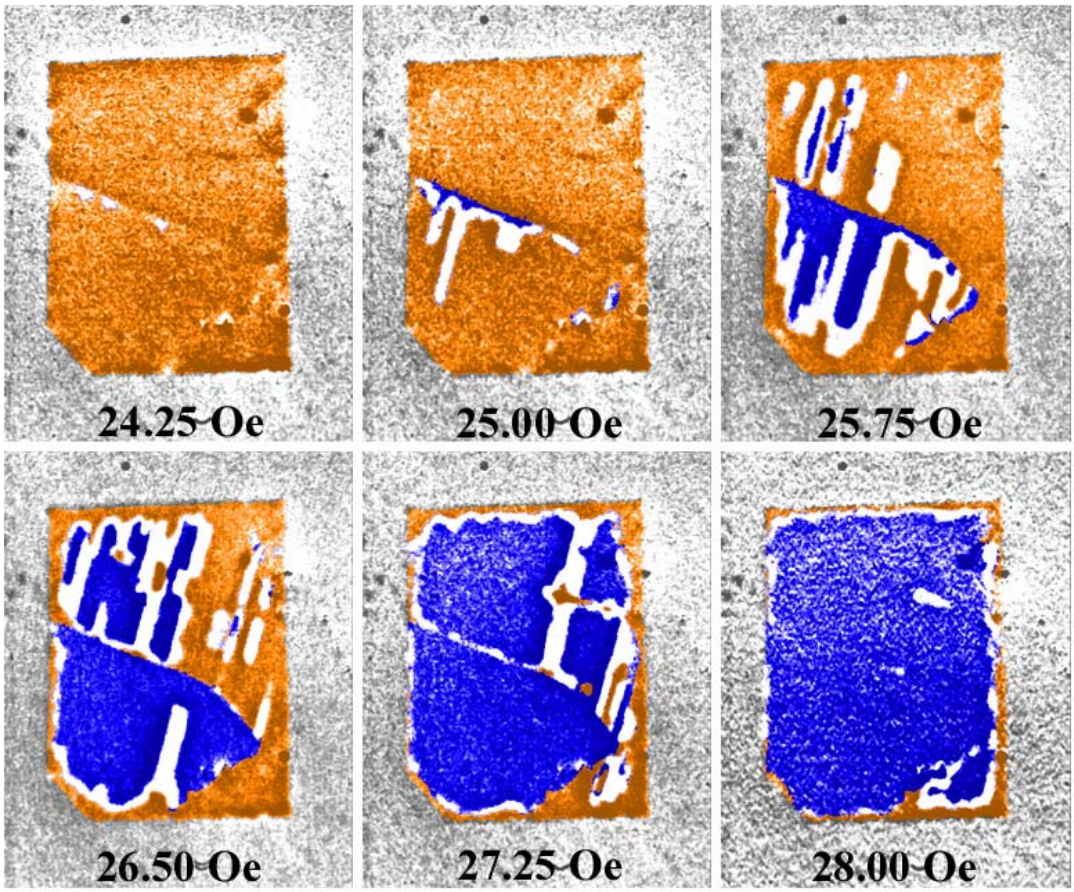

Figure 4.1.3. Differential MO images of the melting process in a BSCCO crystal (T_c=91 K) of area 0.46 × 0.64 mm^2 at various fields and T=84 K, δH_a=0.5 Oe, and H_a || c-axis. The solid and liquid regions are colored in brown and blue, respectively.

The nucleation of the liquid phase in Fig. 4.1.3 starts at the defect (H_a = 24.25 Oe) since H_z has a maximum at the thinner side near of defect. In the beginning the vortex liquid propagates downward in a finger-like structure (H_a = 25.00 Oe). The lower boundary of the liquid propagates with increasing the field but upper boundary is fully pinned at the defect. As a result no differential signal (bright ring) is seen at the top solid-liquid interface along the defect. At higher fields (H_a = 25.75 and 26.50 Oe) the melting nucleates independently in the upper (thick) part of the crystal and the melting propagation is very complex. At H_a = 27.25 Oe almost the entire central part of the crystal is in the liquid phase except for small regions in the upper part and near the defect. Finally (H_a = 28.00 Oe) only a small solid island remains within the liquid phase, which disappears in the next field step (not shown). If we look at the melting contours we find that they have well defined preferential direction perpendicular to the extended defect. We find that this is a common situation in most of the crystals indicating that the melting patterns are related to the crystallographic directions. As a summary for the melting propagation in this crystal, we should note the pronounced influence of the macroscopic defects on the melting process and possible correlation between the melting direction and the crystallographic axis of the crystal.

4.1.4 Disorder-induced melting landscape and rounding of the transition

We now illustrate that the observed complexity of the melting process is the result of disorder. It is well known that disorder and anisotropy can significantly modify the mean-field melting temperature[26,35]. Since these parameters have a broad distribution on a microscopic scale, the melting field or the melting temperature should therefore be position dependent, resulting in some rough $T_m(x,y)$ or $H_m(x,y)$ 'landscape' in the entire volume of the sample . Theoretical analysis[37] of a first-order transition in the presence of moderate disorder that causes spatial variations of the melting temperature, suggests that melting can occur locally in small domains. The local transition occurs when the free energy gain due to local liquid formation is larger than the energy cost of solid-liquid interface creation. These phase fluctuations will result in smearing of the global phase transition around the mean-field H_m^0, and the distribution function of the local melting field $f_m(H)$ develops characteristic tails on both sides of the mean-field H_m^0. Figure 4.1.4.1 shows a schematic one-dimensional profile of $H_m(x,y)$ and its distribution function. Consider that we start

with a situation where the field H_a is below the H_m distribution. In this case the entire sample is in the vortex solid phase. As the field is increased into the bottom of H_m distribution, liquid droplets will nucleate at the local minima of H_m. The liquid regions expand with increasing of H_a, until only few small solid islands remain at the peaks of H_m, and finally the entire sample becomes liquid. By measuring the volume fraction of the liquid as a function of field we can evaluate the $f_m(H)$ distribution function.

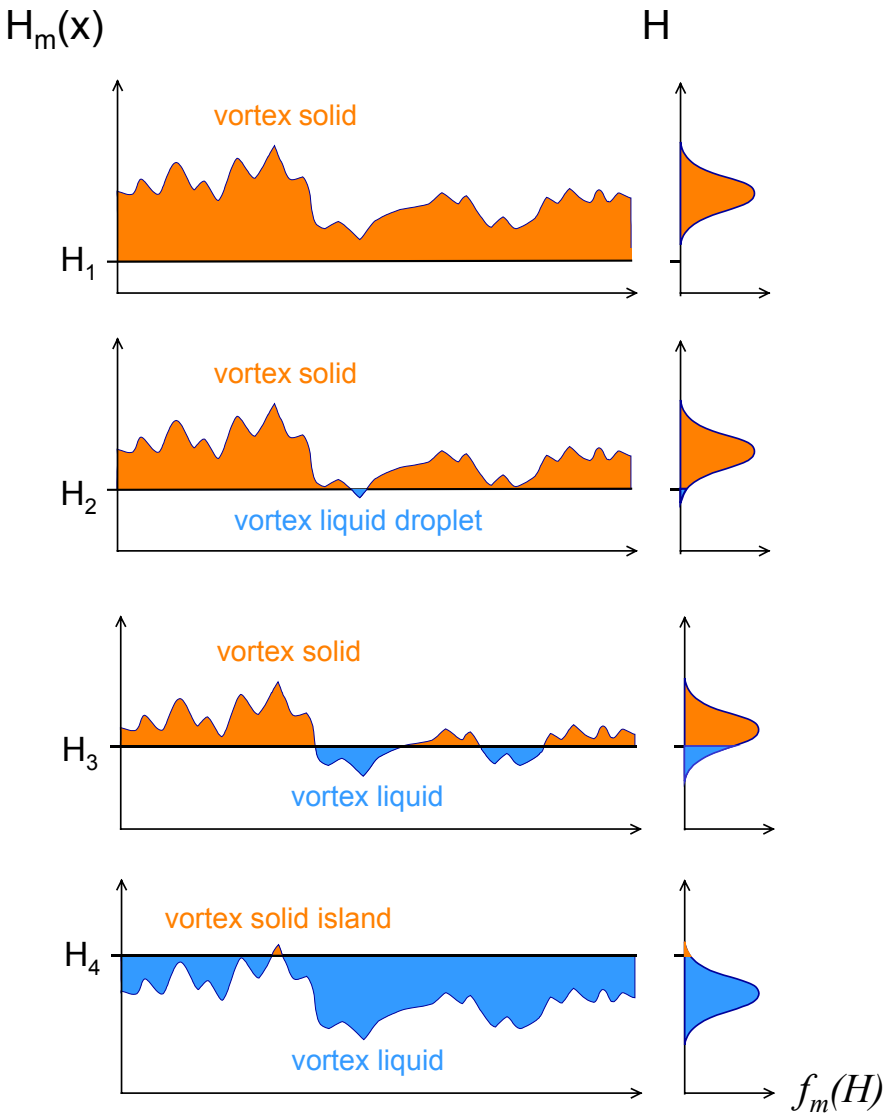

Figure 4.1.4.1. Schematic plot of $H_m(x)$ landscape and the distribution function $f_m(H)$, for various values of the field H.

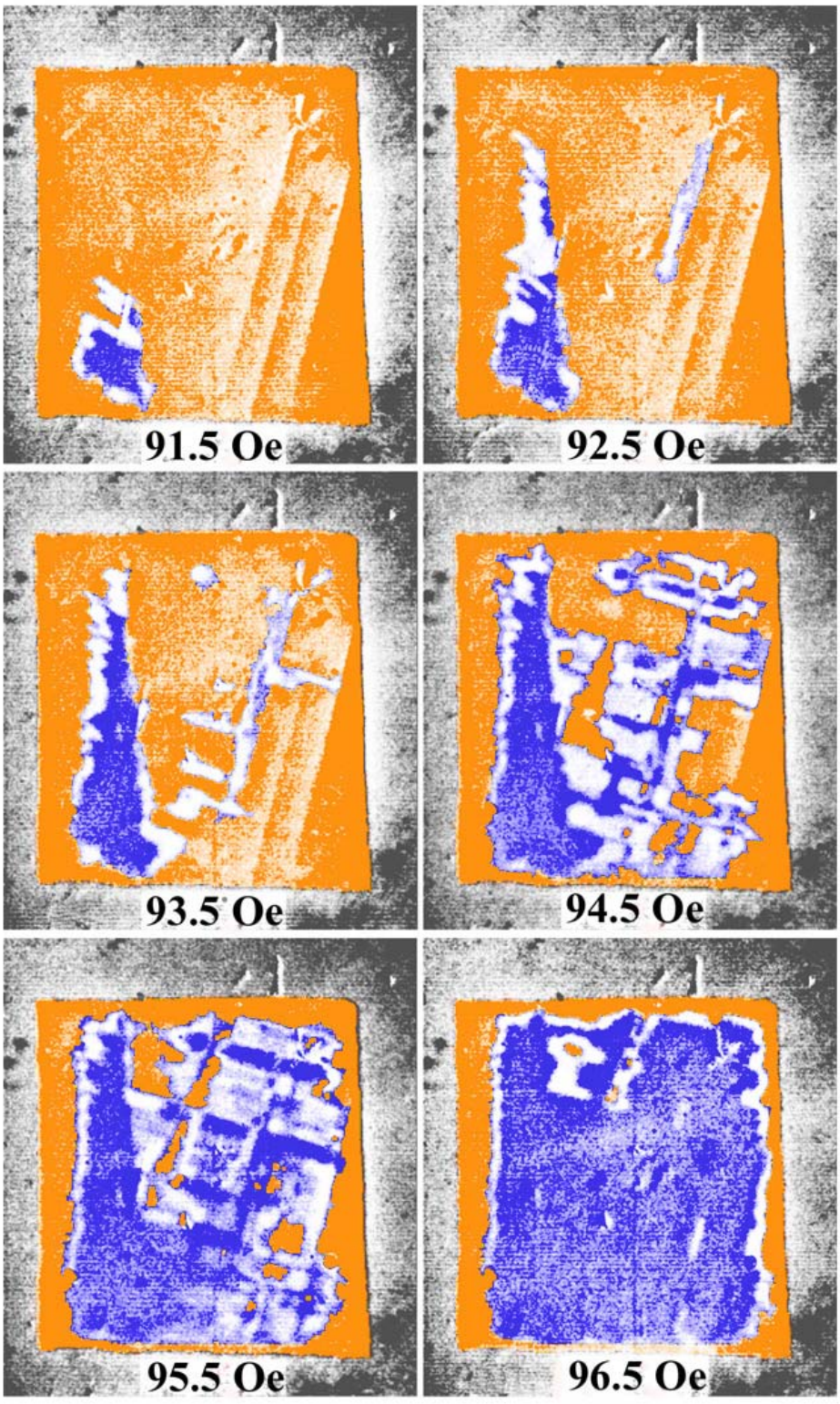

Figure 4.1.4.2. Melting process in a large BSCCO crystal of 1.1×1.2×0.025 mm^3 at T=70 K and δH_a = 1 Oe, demonstrating the effects of disorder. The solid and liquid regions are colored in brown and blue, respectively (see http://www.weizmann.ac.il/home/fnsup for the full movie).

In order to analyze this process quantitatively, Fig. 4.1.4.2 shows a partial set of melting images in a large BSCCO crystal at T= 70 K and δH_a = 1 Oe. The size of the crystal is 1.1×1.2×0.025 mm^3 and it has three crystallographic defects seen as parallel lines. None of these defects are visible in a regular optical microscope. The defects can only be resolved in the differential MO imaging or in the image of the time-dependent magnetic field penetration at low T. The solid and liquid regions are colored in brown and blue, respectively. The vortex-liquid phase of a very irregular shape is formed initially at the lower left corner (blue). At 92.5 Oe a separate liquid region appears along one of the defects. With increasing H_a very complex patterns of intermixed solid and liquid regions are formed at 93.5, 94.5, and 95.5 Oe. The dominant effect of the crystallographic disorder is clearly visible in Fig. 4.1.4.2, since the melting patterns have well defined preferential directions aligned parallel and perpendicular to the defects. At 96.5 Oe a large liquid region is present in the center, with a few solid islands in the top part. The edges remain in the solid phase due to the dome-shaped field profile. Also, the crystallographic defects are not seen when the vortices are in the liquid phase.

Figure 4.1.4.3a presents the volume fraction of the liquid vs. H_a, which allows a derivation of the distribution function $f_m(H)$ shown in Fig. 4.1.4.3b. Although locally the melting is a sharp first-order transition, the global solid-liquid transformation is completely rounded, and $f_m(H)$ displays pronounced tails extending both below and above H_m^0. This general form of $f_m(H)$, which we observe in all the samples, is in agreement with the theoretical predictions. The dashed line in Fig. 4.1.4.3a shows for comparison the calculated melting behavior in the absence of disorder resulting from the fit to the experimental dome-shaped field profile across the sample (see comment below). In this case the melting should set in abruptly, and most of the volume should melt within a few Oe from H_m^0. Thus clearly the disorder has a dominant role in the observed rounding of the transition and in the development of $f_m(H)$ tails. The characteristic radius of the liquid droplets in the images is less than several hundred vortices, which can be compared to the melting visualization in regular solids on the scale of few nm. The presented images are therefore a direct observation on a mesoscopic scale of the rounding process of the first-order transition.

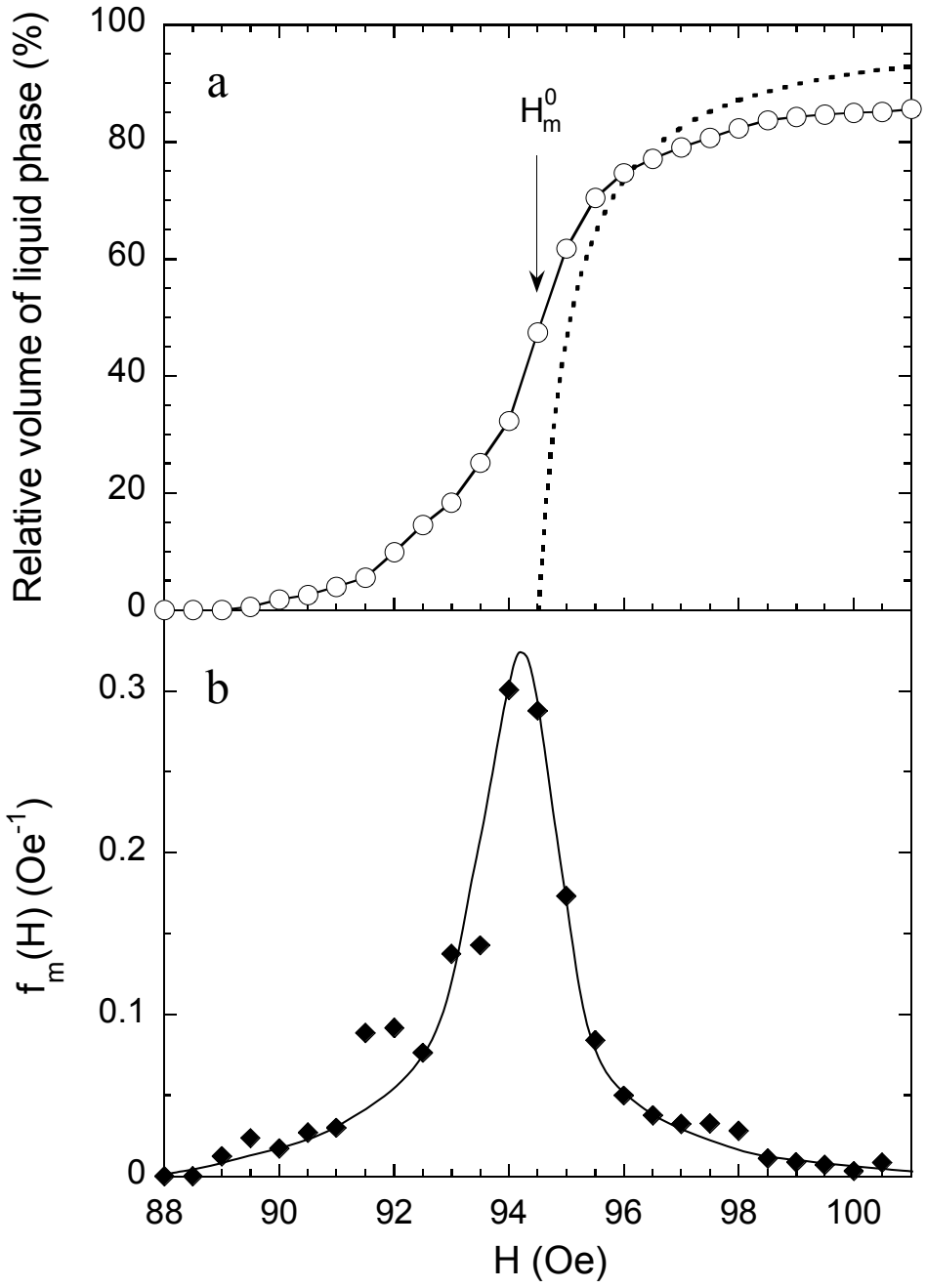

Figure 4.1.4.3. a) Liquid volume fraction vs. H_a obtained from the full melting sequence, showing the global rounding of the melting transition with characteristic tails above and below the mean-field H_m^0. The dashed line shows the calculated liquid fraction in the absence of disorder, due to the dome-shaped internal field profile. b) The experimental distribution function of the melting field $f_m(H)$ obtained by taking the derivative of the vortex liquid volume in (a) with respect to the field H. The solid line is a guide to the eye.

Comment: In order to calculate the rounding due to the dome-shape profile, regular MO images of the crystal were analyzed and the dome shape profile of

magnetic field across the sample was measured. The dome shape profile results from the screening currents flowing at the edges of the crystal. Assuming such current distribution, the magnetic field in the middle of the indicator, 3μm above the surface of the crystal has been calculated using Biot-Savart law. The amplitude of the screening currents has been found by matching the calculated and measured profiles of magnetic field across the sample. Then, the magnetic field in the middle of the crystal was calculated using Biot-Savart law, which allows calculation of the volume fraction of the liquid phase vs. applied magnetic field, presented in Fig. 4.1.4.3a.

4.1.5 Examples of melting behavior

We now present several examples of the melting features in various crystals. Figure 4.1.5.1 shows an enlarged view of nucleation of two liquid droplets in the low-field tail of $f_m(H)$ in a small part of BSCCO crystal at H_a =25.75 Oe and T = 84 K.

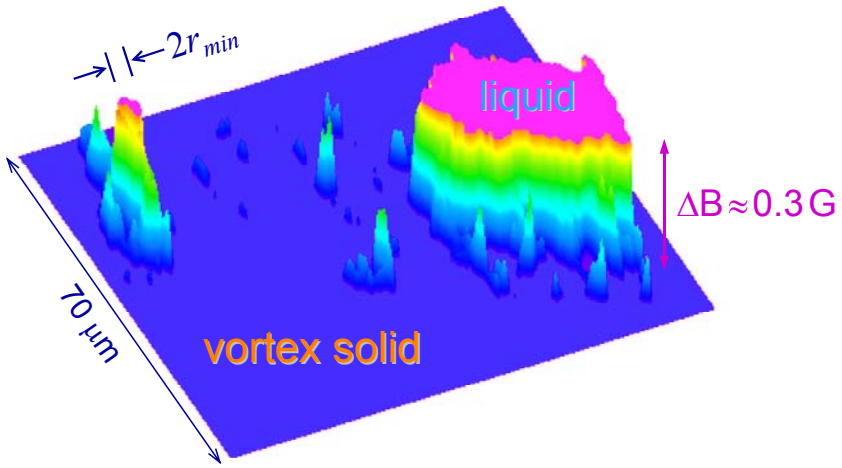

Figure 4.1.5.1. Three-dimensional representation of the differential image in a selected part of BSCCO crystal, T = 84 K, H_a = 25.75 Oe, δH_a=0.5 Oe. The field scale from blue to magenta is about 0.1 G. Two liquid droplets (magenta) are surrounded by vortex solid (blue). The smaller droplet on the left is only about 7 vortices wide, demonstrating that disorder-assisted melting occurs on the scale of inter-vortex distance.

The width of the smaller droplet is below 6 μm (close to our resolution limit), which means that this droplet is less than 7 vortices wide. This image is a striking demonstration that the disorder-nucleated melting occurs on a mesoscopic level. Furthermore, it shows that the solid-liquid surface tension is very low, as addressed below. Such liquid droplets, formed at local minima of $H_m(x,y)$ (see Fig. 4.1.4.1), are found to behave reversibly with field, in contrast to solid islands at maxima of $H_m(x,y)$, as described below. Another example of liquid nucleation in a different BSCCO crystal is shown in Fig. 4.1.5.2. Here the nucleation occurs simultaneously in three adjacent regions, demonstrating specific correlations in the distribution of disorder quenched during the crystal growth. The characteristic width of the solid and liquid patterns is about 25 μm (34 vortices), further indicating low surface tension. High surface tension would prevent such proximity of microscopic domains, favoring formation of a single larger liquid region.

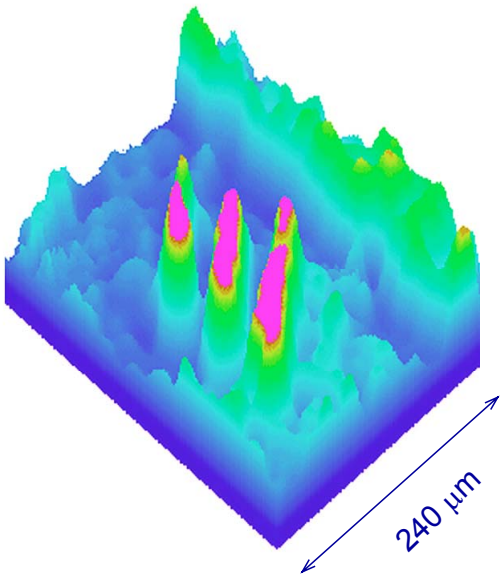

Figure 4.1.5.2. Three-dimensional representation of the differential image at the nucleation of the vortex-lattice melting, T = 80 K, H_a = 38.5 Oe, δH_a=1.0 Oe. Vortex liquid nucleation (magenta) occurring simultaneously in three adjacent finger-like regions. The field scale from blue to magenta is about 0.3 G. The top right side of the image shows one of the sample edges (green).

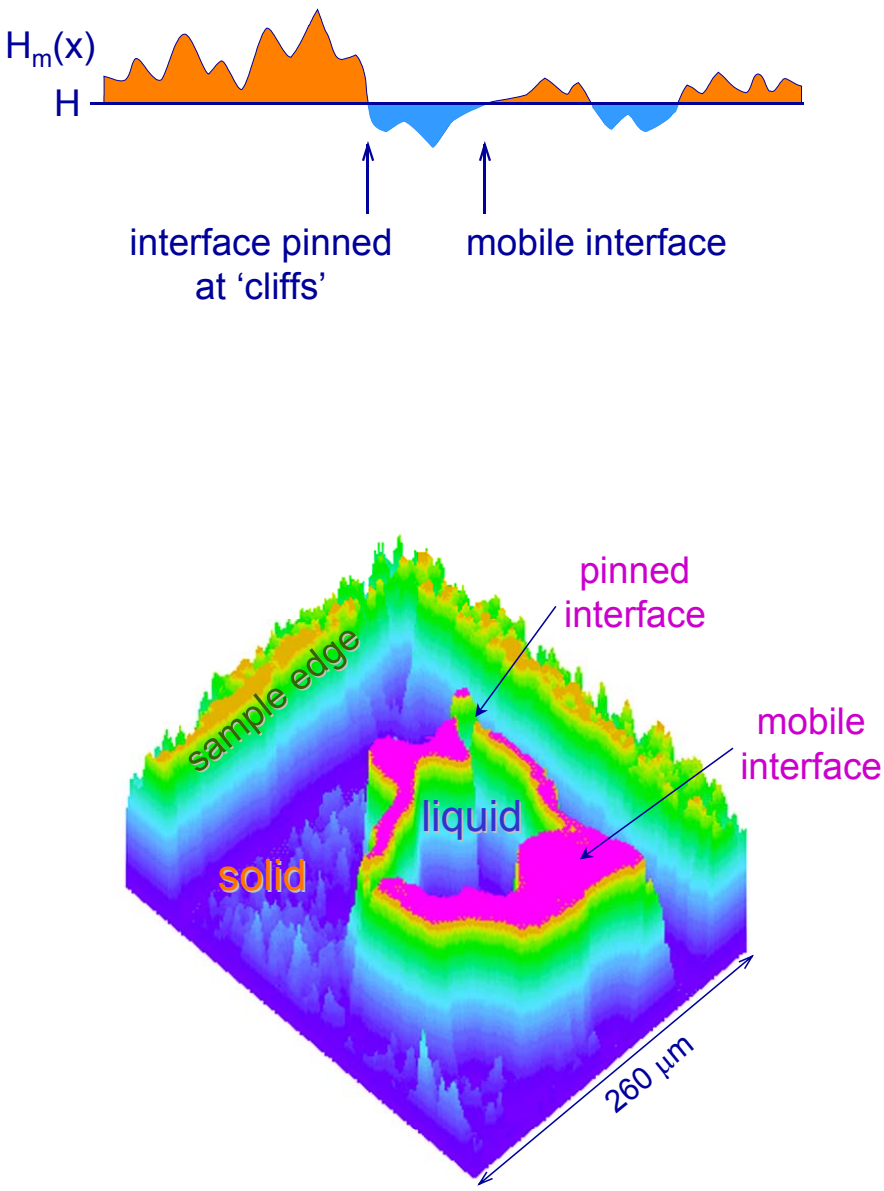

Figure 4.1.5.3. a) (Top) Schematic plot of $H_m(x)$ landscape which illustrates the melting propagation behavior. b) (Bottom) An irregular vortex liquid region surrounded by vortex solid is shown in three-dimensional representation. Outer edges of the sample are seen along the top sides of the image. H_a = 83 Oe, δH_a = 0.5 Oe, and T = 70 K. Image area is 0.26 × 0.34 mm^2.

As the field H_a is further increased large liquid regions are formed with a very irregular shape and the solid-liquid interface is often seen to be pinned. This behavior is due to the rough landscape of the melting field H_m. In the regions where the landscape varies gradually (shallow and smooth shores), the interface is highly mobile

and expands significantly in response to a small increase in applied field (Fig. 4.1.5.3a). At "steep cliffs", in contrast, the solid-liquid interface is effectively pinned, and does not propagate upon small variation of the field.

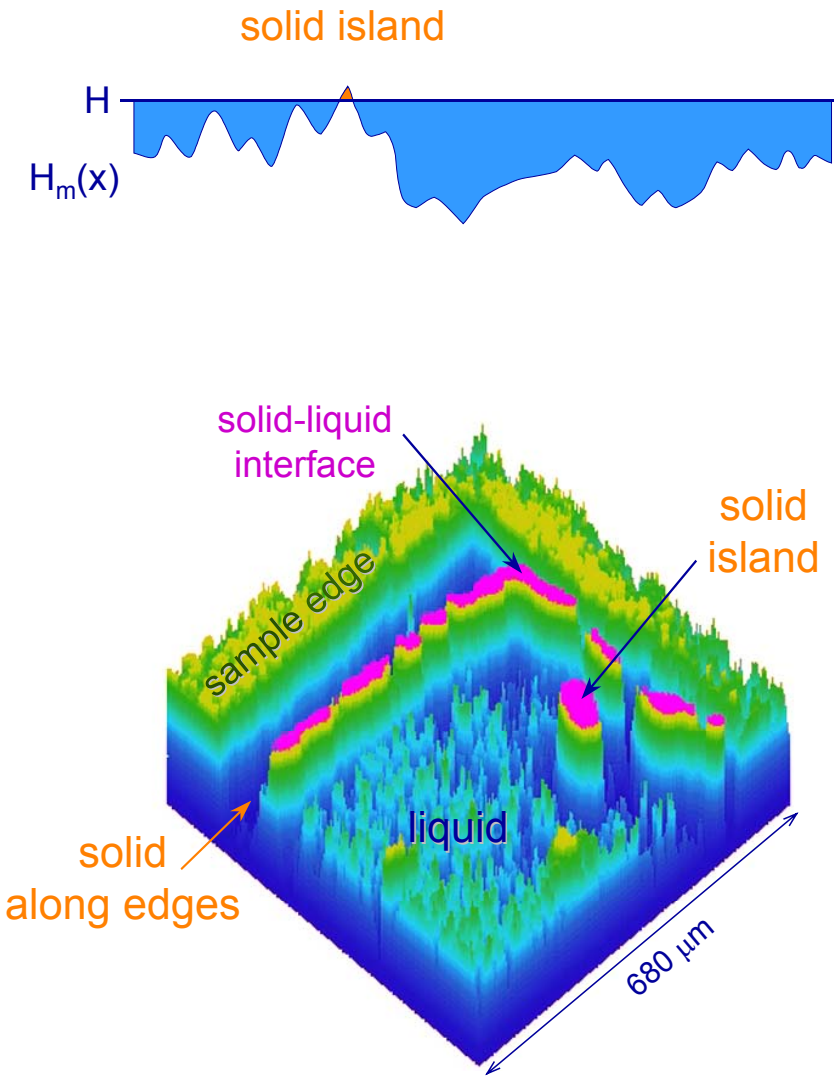

Figure 4.1.5.4. a) Schematic plot of $H_m(x)$ landscape at the formation of a solid island. b) A small vortex-solid island surrounded by vortex liquid. The liquid phase is in turn surrounded by vortex solid along the sample edges. The solid-liquid interface near the edges (magenta rim) appears highly nonuniform and discontinuous due to the alternating regions of mobile and pinned interface. Image area 0.68 × 0.68 mm^2, H_a = 69.5 Oe, δH_a = 0.5 Oe, and T = 75 K.

The example of such situation is demonstrated in Fig. 4.1.5.3b. Here a highly irregular ring separates the vortex liquid from the surrounding solid. The local width of the ring is a direct measure of the distance the interface expands due to δH_a. In some parts the ring is very broad, showing the locations where $H_m(x,y)$ has smooth, gradual behavior, resulting in a very mobile interface. In contrast, in other places where the ring appears to have discontinuities, the solid-liquid interface is effectively pinned due to steep $H_m(x,y)$ and does not move in response to the field modulation, resulting in zero differential signal at these points.

As the liquid domains expand with H_a, the peaks in $H_m(x,y)$ melt last, forming solid islands within the liquid (see Fig. 4.1.5.4a). Figure 4.1.5.4b depicts such a small solid island completely surrounded by vortex liquid, which in turn is surrounded by vortex solid along the edges of the crystal. The solid-liquid interface near the edges (magenta rim) appears highly nonuniform and discontinuous due to the alternating regions of mobile and pinned interface. The melting and freezing process of this solid island is characterized by a high degree of hysteresis, as described below in §4.1.7.

4.1.6 Evaluation of the solid-liquid surface tension

The solid-liquid surface tension is a key element in the stability considerations in the presence of disorder[37]. The characteristic size of the nucleating liquid domains is set by competition between the positive surface energy of the solid-liquid interface and the energy gain of liquid formation. Also the global rounding of the transition is determined by interplay between the width of H_m distribution and surface tension. Our experimental results allow evaluation of the surface tension σ of the solid-liquid interface. Theoretically, the surface tension can be estimated as follows. At the first-order transition the discontinuous change in the internal energy is compensated by a change in the entropy, such that the free energy remains continuous. The jump in the energy density is roughly equal to $H_m \Delta B/4\pi$. If the solid-liquid interface has a width of the order of the inter-vortex spacing a_0, then within this width the system is neither liquid nor solid. Thus the energy cost per unit area of this interface can be estimated as $\sigma = \eta a_0 H_m \Delta B/4\pi$, where η is unknown numerical factor presumed to be of order unity. When H exceeds a local minimum by $h = H-H_m$, a liquid droplet should be formed in a solid, provided the energy gain in melting is larger or equal to the energy cost of forming an interface. Assuming that the droplet is of radius r and that it extends throughout the thickness d of the sample, the energy gain is given

approximately by $(\partial F_s/\partial H - \partial F_l/\partial H)h\pi r^2 d = \Delta B h r^2 d/4$. Here $\partial F_s/\partial H$ and $\partial F_l/\partial H$ are the derivatives of the free energies of the solid and liquid phases respectively, and we have used the fact that $\partial F_s/\partial H - \partial F_l/\partial H = \Delta B/4\pi$ at the melting transition. By comparing this gain with the interface energy $2\pi\sigma r d$, we obtain the minimum nucleation radius $r_{min} \approx 2\eta a_0 H_m/h$. Figure 4.1.5.1 shows the existence of very small liquid droplets with $r_{min} \approx 3a_0$. By analyzing the expansion of the droplets due to δH_a and upon varying H_a, we estimate the superheating h to be less than 0.5 Oe for a typical H_m of 50 Oe, which results in $\eta \leq 10^{-2}$. Thus assuming that $H_m(x,y)$ exhibits smooth local behavior, our measurements indicate that σ is two orders of magnitude lower than rough theoretical estimates. Such a low surface tension implies that the vortex melting process is completely governed by disorder and that the stabilizing influence of the interface can be neglected. The reason for such a low surface tension is not clear at present. In §4.2 we discuss the possible change of the surface tension, as well as of the disorder-induced melting landscape along the melting line and the resulting temperature dependence of the melting patterns.

4.1.7 Hysteresis and supercooling

Hysteretic supercooling and superheating is an inherent property of a first-order transition[51], but the precise mechanism on a microscopic level is not clear. We are able to spatially resolve this unique feature, as shown in Fig. 4.1.7.1. We find that the hysteresis occurs only at the local maxima of $H_m(x,y)$, indicating that disorder is an important factor also in the nonequilibrium properties. In the top left image, at 68.50 Oe, a few vortex-solid islands are visible within the liquid in the upper part. As the field is increased, these solid islands split into smaller ones, and gradually shrink and disappear. At 69.50 Oe only one small island is left, visible as a bright spot, which fully melts at 69.75 Oe. A better view of the top-left corner of the sample including this island is shown in Fig. 4.1.5.4b.

Upon decreasing H_a, the bright interface along the sample edges, separating the large central liquid region and the outer solid strips, behaves completely reversibly (compare the melting and freezing images at the same field). The inner solid islands, in contrast, are *absent* upon freezing, and then suddenly reappear at a lower field of 68.50 Oe. Once formed, the islands extend to their full size at the corresponding field, and proceed to behave reversibly as long as they are not fully melted again. (It is

interesting to note that at the nucleation of the solid islands at H_a = 68.50 Oe on freezing we see only the outer boundary of the islands. This bright boundary reflects the motion of the solid-liquid interface as in corresponding image in the melting sequence. We do not observe the initial nucleation of the entire island because each image is an average of approximately 100 up-down modulations (§3.2). The relatively large island nucleates only at the first modulation and after that, only the island boundary moves in response to the field modulation. The signal due to island nucleation is captured only in the first frame out of approximately 100 frames and is therefore averaged out completely).

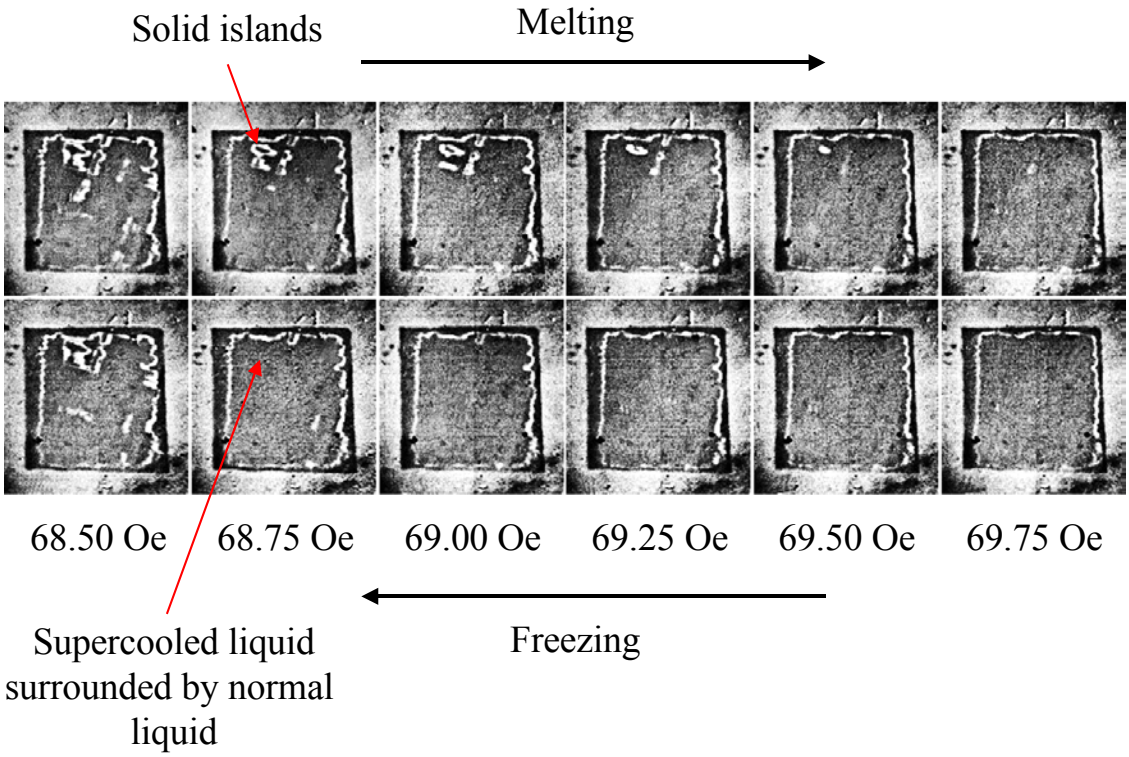

Figure 4.1.7.1. Direct visualization of the local supercooling and hysteresis process. The top row of images shows the melting sequence upon increasing the field, while the bottom is the freezing process at the same values of decreasing field. Sample size is 1.1 × 1.2 × 0.025 mm^3, T=75 K and δH_a = 0.5 Oe. Small dark and bright spots that do not vary with field are defects in the MO indicator.

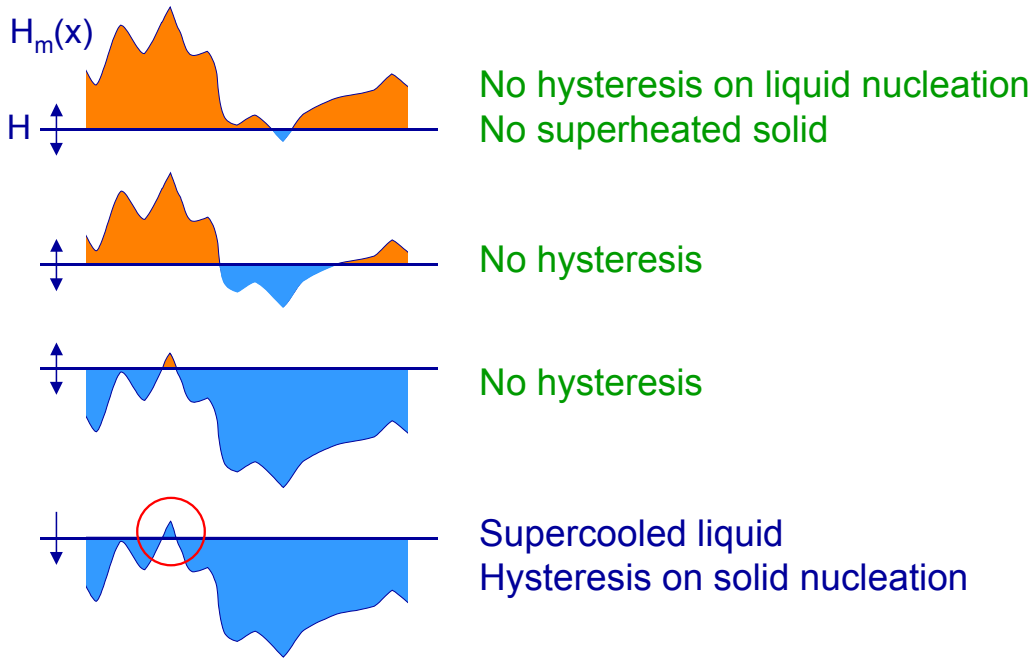

Figure 4.1.7.2. Schematic plot of $H_m(x)$ summarizing the observed hysteresis.

Reversible behavior most likely reflects an equilibrium state of the system. The above results therefore imply that there is no supercooling or superheating when the solid-liquid interface is located in regions where the $H_m(x,y)$ landscape varies monotonically, as summarized in Fig. 4.1.7.2. The hysteresis is not observed upon nucleation of vortex liquid droplets within a solid, and superheating of a solid does not occur. At higher fields, when the phases are separated into larger domains, there is no hysteresis either. Also when small solid islands are left the behavior is reversible as long as they do not melt completely. So whenever a solid-liquid interface is already present, its expansion and contraction is reversible. The hysteretic behavior occurs only when a new interface has to be formed, but only if this new interface surrounds a solid rather than a liquid. Hence, after a complete melting, upon reducing H to below a local maximum of $H_m(x,y)$, the solid island is not readily formed (see lower panel of Fig. 4.1.7.2). In this regime a unique situation occurs: metastable *supercooled* liquid domains, which are present instead of the 'missing' solid islands, coexist with the surrounding *equilibrium* liquid. Only when the supercooling becomes sufficiently large, does sudden nucleation occur, upon which the solid abruptly occupies the entire

volume of the supercooled domains. This nonequilibrium process is observed only at local maxima of $H_m(x,y)$. One would expect a symmetric nonequilibrium mechanism to be present at minima of $H_m(x,y)$, where superheated solid would transform hysteretically into a liquid droplet, but such hysteresis is not found. The asymmetry between the supercooling and superheating on a macroscopic scale is usually ascribed to the surface wetting process, which prevents solid superheating[51]. In our case mesoscopic vortex droplets are formed *within* a solid and therefore such an asymmetry should not be expected. Nevertheless, the tips of the vortices near the top and bottom surfaces of the crystal experience a reduced elastic confinement potential due to the absence of the lattice outside the sample. As a result, the vortex tips may undergo a premelting transition similar to the surface wetting in atomic solids, which may prevent the superheating of the vortex solid. In contrast to atoms, however, each vortex tip is attached to a solid vortex in the bulk, and therefore is restricted in space and may not exhibit liquid properties.

4.2 Temperature variation of the vortex-lattice melting landscape

As discussed above, the presence of disorder modifies the properties of the vortex lattice melting. In particular, weak point disorder shifts the vortex-lattice melting transition to lower temperatures while preserving its first-order nature[34,52]. Correlated disorder, on other hand, tends to shift the transition to higher temperatures[26,53]. Oxygen doping is another important parameter that governs the location of the melting line. Doping modifies the critical temperature T_c as well as the material anisotropy, which significantly changes the slope of the melting line[35,49]. All these parameters, which determine the location of the mean-field transition line $T_m(H)$ on the H-T phase diagram, may also have significant variations in their local values. As a result the local melting temperature $T_m(H,r)$ is expected to exhibit significant space fluctuations[37].

In this part we present a detailed study of the melting process at various points along the first-order transition line. In contrast to what one may expect, the disorder-induced landscape is not invariant but rather varies profoundly with changing the temperature along the melting line. It is found that the valleys of the landscape may turn into peaks and that the characteristic lengthscale of the potential fluctuations increases by an order of magnitude with decreasing temperature. These unexpected changes in the melting landscape are shown to arise from competing contributions of various types of disorder, which influence the melting transition differently.

Figure 4.2.1 shows four examples of the differential melting patterns at four different points along the melting line. All images reflect a situation in which approximately 50% of the crystal volume is occupied by the liquid phase. There are two striking observations in these images: one is that the characteristic lengthscale of the melting patterns changes dramatically with increasing the field, and the other is that in most of the sample area there is little correlation between the patterns at low and high fields. At H_a=20 Oe the liquid regions form arc-like patterns in the vertical direction. At lower fields, 10 Oe, the arcs fracture into microscopic droplets each containing just few tens of vortices. At higher fields in contrast, the patterns become much more coarse (40 and 75 Oe images) and gradually lose correlation with the low-field patterns. About 75 Oe and up to our highest field of 300 Oe, the melting patterns show only little change with field (not shown).

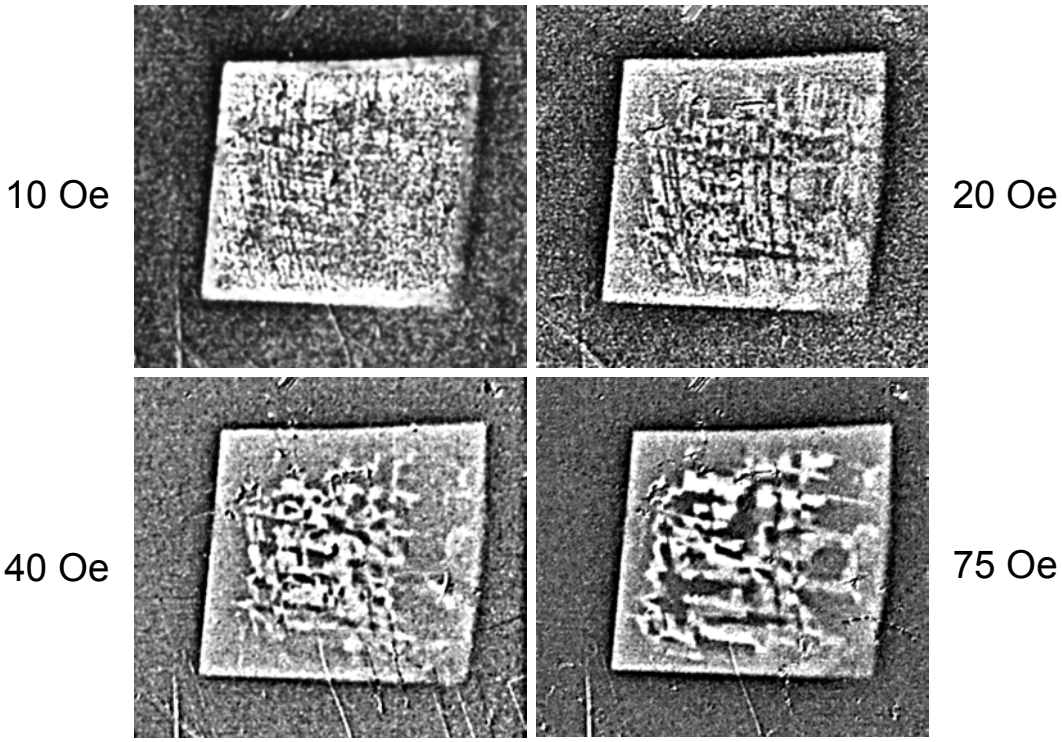

Figure 4.2.1. Differential MO images of the vortex-lattice melting in BSCCO crystal at four points along the melting line $H_m(T)$: 10 Oe (89.5 K), 20 Oe (86.75 K), 40 Oe (82.0 K), and 75 Oe (75.25 K). The differential images are obtained by subtracting the image at T-δT/2 from image at T-δT/2, with δT = 0.25 K.

Figures 4.2.2a and 4.2.2b present the details of lattice melting process, where the different colors show the areas that the liquid phase progressively occupies as T is increased in increments of 0.25 K. Material disorder modifies the local melting temperature, thus forming a complicated $T_m(H,r)$ landscape. Figures 4.2.2a and 4.2.2b can thus be viewed as 'topographical maps' of this landscape at H_a of 20 and 75 Oe respectively. The minima points and the valleys of the landscape melt first (blue) whereas the peaks of the landscape melt last (red). The two landscapes in Fig. 4.2.2 are substantially different. In addition to the significant change in the characteristic lenghscale and the roughness of the landscape, there are many regions in the sample that show qualitatively different properties. For example, at 20 Oe the valley in a form of an arc along the 'O-O' dashed line has three narrow and long blue segments. At 75 Oe, in contrast, the blue minima have a form of rather circular spots. Also, at 75 Oe in the lower-right corner of the sample, to the right of the 'O-O' valley a number of blue and cyan minima are visible. At 20 Oe, on the other hand, this region is rather

'elevated' characterized by green and yellow colors. In the top part of the sample a yellow 'ridge' is clearly visible along 'P-P' line in Fig. 2b, whereas in Fig. 2a this ridge is absent. At 75 Oe on the right-hand-side of the ridge there is an extended orange peak, whereas in the corresponding region at 20 Oe blue and green valleys are seen. Also, importantly, the width of the transition or the valley-to-peak height, changes significantly. At 20 Oe the entire sample melts within about 1 K whereas at 75 Oe the melting process spans almost twice this range.

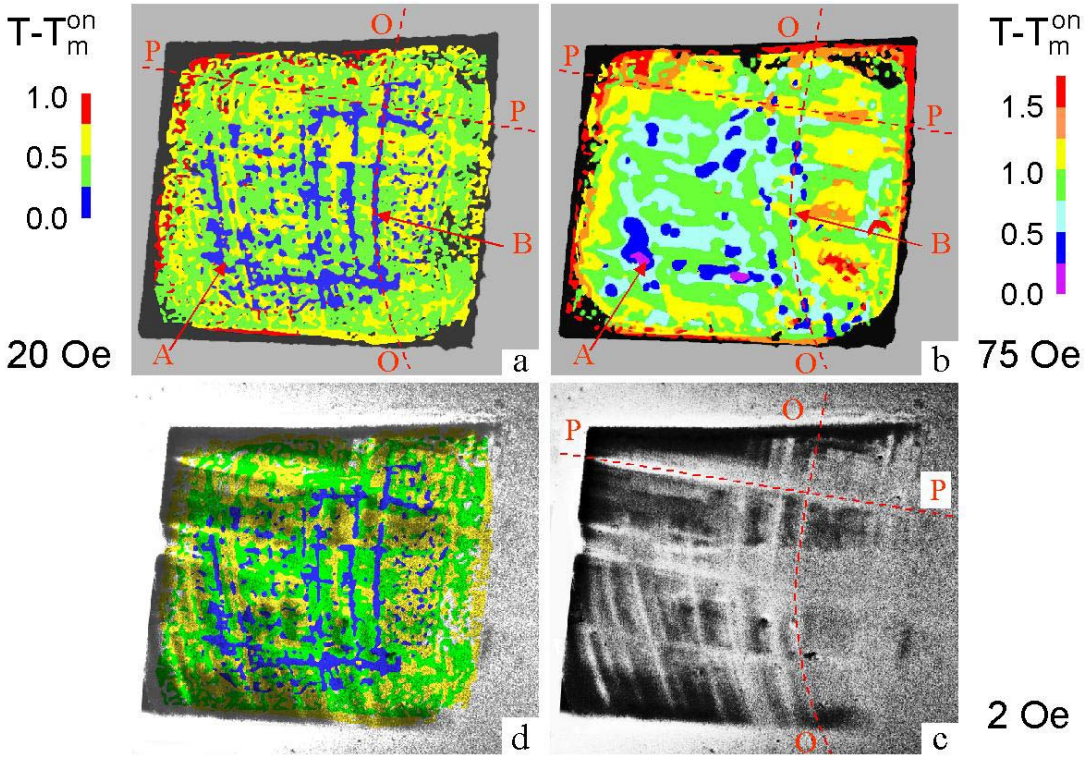

Figure 4.2.2. Contours of the melting propagation at H_a = 20 Oe (a, T_m^{on} = 86.25 K) and 75 Oe (b, T_m^{on} = 74.25 K). The color code describes the location of the liquid domains as they expand with increasing the temperature in 0.25 K steps. c) Differential magneto-optical image of the magnetic field penetration at H_a = 2 Oe, T = 89 K, δH_a = 1 Oe. d) Superposition of (a) and (c).

For a more quantitative analysis we have inspected the melting behavior at several points, like for example points A and B in Fig. 4.2.2. The melting lines $T_m(H)$ of these two points are shown in Fig. 4.2.3a. There is a systematic deviation between the two melting lines that is seen more clearly in the main panel in the form of their difference T_{mB}-T_{mA} versus the mean-field T_m. Close to T_c, point B melts about 0.5 K below point A whereas at lower temperatures the behavior is inverted and point B melts about 2 K above point A. The two melting lines intersect at about 85 K. There

are numerous other points in the sample that show intersecting melting lines, which means that regions which are valleys of the landscape at low fields may turn into peaks at high fields and vice versa. Figure 4.2.3c shows the measured full width of the transition in the entire sample. At high temperatures the vortex lattice melts within about 1 K whereas at low temperatures the transition width reaches about 5 K. All these findings show that the apparent melting landscape changes significantly along the melting line.

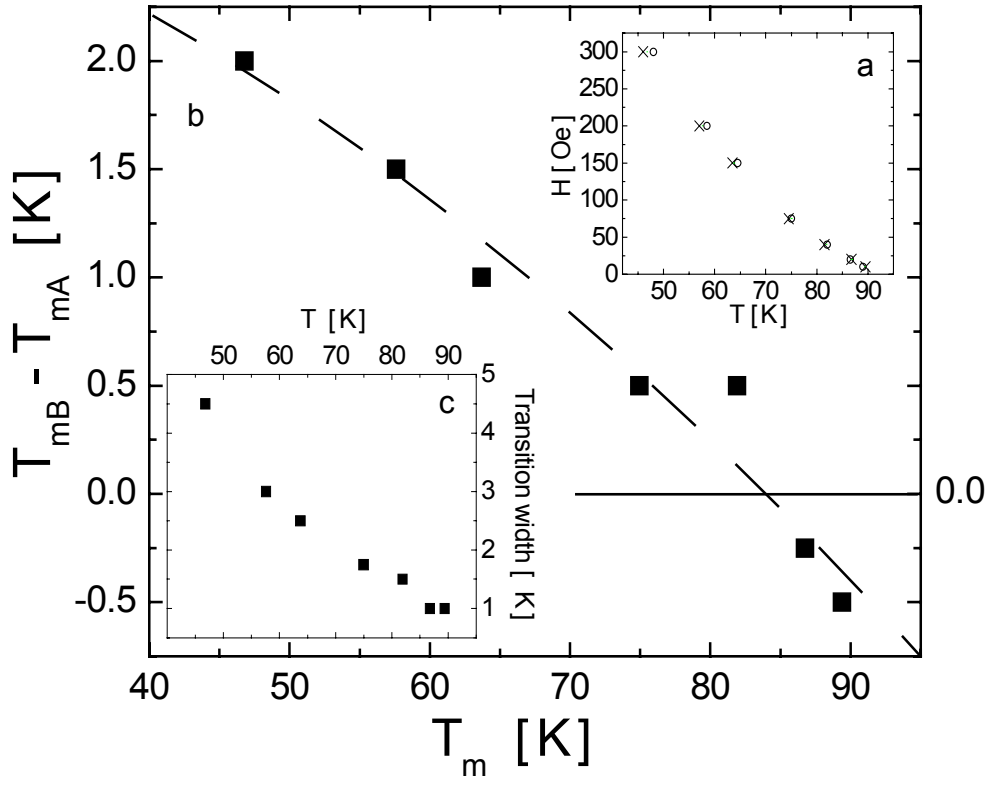

Figure. 4.3.3. a) Local melting lines at points A (×) and B (○) indicated in Fig. 2. b) Difference of the melting temperature at points B and A vs. the average melting temperature. c) The full width of the melting transition vs. temperature.

There are two main factors that determine the apparent melting landscape; one is the disorder-induced potential landscape and the other is the solid-liquid surface tension σ. We analyze first the effects of surface tension. The minimum nucleation radius r of a liquid droplet is determined by the balance between the free energy gain at the transition $\Delta F = (\partial F_s/\partial H - \partial F_l/\partial H)\, h\pi r^2 d = \Delta B h r^2 d/4$ and the energy cost of the

interface creation $2\pi\sigma rd$, which results in $r = 8\pi\sigma\Delta Bh$. Here $h = H\text{-}H_m(T)$ is the degree of superheating, d is the thickness of the sample, and $\partial F_s/\partial H$ and $\partial F_l/\partial H$ are the derivatives of the free energies in the solid and liquid phases, which are related by $\partial F_s/\partial H - \partial F_l/\partial H = \Delta B/4\pi$. The surface tension can be estimated (§4.1.6) as $\sigma \approx \eta a_0 H_m \Delta B/4\pi$, where η is a numerical prefactor, $a_0 \approx (\phi_0/H)^{1/2}$ is the intervortex spacing, and ϕ_0 is the flux quantum. σ is thus expected to grow as $H_m^{1/2}$ and hence the size of the nucleating liquid droplets should increase accordingly as $r \approx 2\eta(\phi_0 H_m)^{1/2}/h$. Thus the increase in the characteristic size of the liquid patterns in Figs. 4.2.1 and 4.2.2 with the field could perhaps be attributed to the increase in the surface tension. However the above estimate of the contribution of the surface tension was carried out without disorder. In the presence of disorder the variations in the nucleation radius due to change in σ are expected to be reduced. In contrast, inspection of 10 and 75 Oe patterns in Fig. 4.2.1, for example, indicates that the increase in the characteristic droplet sizes is substantially larger than the expected $7.5^{1/2}$=2.74. Furthermore, the fact that above 75 Oe up to 300 Oe the scale does not change with field is inconsistent with the surface tension scenario. Yet the most compelling argument against a dominant role of surface tension is the following. For a given potential landscape a larger σ should smear out the fine structure of the landscape, acting as a short-range filter, but preserving the long-range correlations. Analysis of the melting patterns shows that this is not the case and both the short and long range correlations are lost with increasing H_a. In addition, it is highly unlikely that surface tension can cause the local melting lines to cross as in Fig. 4.2.3 and to change the macroscopic valleys into peaks and vice versa. Finally, a larger σ should sharpen the overall melting transition by cutting off the tails of the disorder-induced distribution function of the melting landscape[37], in contrast to our observation of the broadening of the transition with increasing H_a (Fig. 4.2.3c). We therefore conclude that the observed changes in the melting patterns are mainly the result of the changes in the disorder-induced potential landscape. This conclusion is consistent with the previous assessment of a very low solid-liquid surface tension (§4.1.6).

We now address the possible mechanisms of the variation of the potential landscape. For this it is convenient to parameterize the local melting curves using the generic expression of the melting transition[54] $H_m(T,r)=H_0(r)(1\text{-}T/T_c(r))^{\alpha(r)}$. We find that $\alpha(r)$ depends only weakly on the location and therefore set $\alpha(r)= \alpha$ for simplicity.

Defining $T_c(r)=T_c+\Delta T_c(r)$ and $H_0(r)=H_0+\Delta H_0(r)$, we rewrite $H_m(T,r)=H_m(T)+\Delta H_m(T,r)$, where $H_m(T)= H_0(1-T/T_c)^{\alpha}$ is the mean-field melting line, and $\Delta H_m(T,r)\cong(\Delta H_0(r)+\alpha H_0\Delta T_c(r)/(T_c-T))(1-T/T_c)^{\alpha}$ describes the disorder-induced melting landscape. $\Delta H_m(T,r)$ has two terms, the first results from variations in the slope of the melting line $\Delta H_0(r)$ and the second from variations in the local T_c. Due to the diverging T_c-T denominator the second term becomes dominant near T_c whereas the first term is dominant at low temperatures. Analysis of the local melting lines at various locations across the sample results in the following parameters: H_0 = 900 Oe, ΔH_0 = 80 Oe, T_c = 95 K, ΔT_c = 0.7 K and α = 1.6. Using these values we find that the two terms of $\Delta H_m(T,r)$ become comparable at $T \approx$ 82 K. This result explains a number of observed features: Since at low temperatures $\Delta H_0(r)$ is the dominant term, the form of the landscape becomes temperature and field independent explaining the invariance of the melting patterns above 75 Oe. However the amplitude of the landscape fluctuations increases as $(1-T/T_c)^{\alpha}$ with decreasing temperature explaining the continuous broadening of the transition width in Fig. 4.2.3c. When the two terms of $\Delta H_m(T,r)$ become comparable above about 80 K the form of the landscape changes because of the superposition of two different landscape shapes generated by each term. As a result the melting patterns change significantly and loose their spatial correlations as seen in Fig. 4.2.1. At higher temperatures the local variations in T_c should eventually become the dominant parameter that governs the melting patterns. One can check the self-consistency of this argument as follows. At high temperatures ΔT_c should also modify the local critical field $H_{c1}(r)$ and the corresponding value of the local penetration field. Figure 4.2.2c shows a high sensitivity image of the initial field penetration into the sample at H_a = 2 Oe and T = 89 K. A strong correlation between the penetration form and the melting patterns at low fields is readily visible. For a more accurate comparison Fig. 4.2.2d presents a superposition of the penetration image with the melting patterns at 20 Oe. The color in the image is given by the melting contours, while the brightness is defined by the penetration field. It is clearly seen, that most of the macroscopic blue regions of liquid nucleation coincide with the bright areas where the field penetrates first. In particular, the correspondence between the arc structures of the penetration field and the melting contours is remarkable. This correspondence indicates that the melting propagation at low fields is indeed governed by the local variations in T_c. It is interesting to note that a

comparison of the penetration image with the melting contours at H_a = 75 Oe results in a surprisingly largely anti-correlation behavior: the regions in which the field penetrates first are the last ones to melt. Such anti-correlation is clearly seen for example for the 'P-P' strip, which is bright in Fig. 4.2.2c but is mainly yellow and orange in Fig. 4.2.2d. Such anti-correlation behavior causes the observed crossing of the local melting lines as in Fig. 4.2.3 and results in the variable melting landscape.

It is interesting to understand which types of material disorder contribute to the different trends of the melting landscape. Variations in pinning by point disorder may locally destabilize the lattice resulting in landscape minima. Local correlated disorder, in contrast, is expected to stabilize the lattice creating maxima points of the landscape. However such pinning disorder is not expected to cause appreciable ΔT_c variations, nor should it results in crossing of the local melting lines. Variations in the oxygen stoichiometry or in cation ratio, on the other hand, could give rise to both effects. Oxygen doping modifies both the T_c and the anisotropy. In overdoped domains T_c is suppressed, but the corresponding reduction in anisotropy results in a larger slope of $H_m(T)$ which may lead to the crossing of the local melting lines. Our analysis of the crystal growth conditions indicates that the arc structures in Fig. 4.2.2 are related to slight modulation in material composition and the curved form of the meniscus between the solid and liquid phases of BSCCO during the floating zone crystallization process. We have also carried out preliminary X-ray spectroscopy microanalysis[55], which indicates some correlation between small variations in the Sr/Cu ratio and the melting patterns. This finding further indicates that the complexity of the melting is related to the sample disorder and inhomogeneities. However the specific influence of the disorder still requires further investigations since the same variation in Sr concentration, for example, can have different microscopic effects depending on the exact sited occupied by excess Sr.

4.3 Melting propagation in selectively irradiated crystals

So far we have studied the vortex-lattice melting only in crystals with weak intrinsic disorder. As discussed above, the presence of such kind of disorder results in complex nucleation and propagation of the vortex-lattice melting transition. Furthermore, the properties of the transition vary significantly along the melting line due to the nontrivial variation of the local melting parameters with the temperature. The intrinsic disorder is apparently caused by small composition variations during the crystal growth process. These variations can modify the local values of λ and ξ, but still the origin of the disorder as well as the role of the different chemical elements is poorly understood.

In order to evaluate the mechanism governing the properties of the vortex-lattice melting, we have created localized regions of correlated disorder in the crystal and studied the resulting propagation of the transition. The correlated disorder is created by irradiation of the crystals with heavy ions. The high-energy ions create columnar defects along their trajectory on passing through the crystal. The experimental procedure is described in detail in §3.4. The crystal is covered by mask prior to the irradiation in order to produce the defects only in specific regions (Fig. 3.4). The application of mask makes possible to compare the irradiated and non-irradiated regions located in proximity to each other. The comparison between neighbouring regions avoids possible differences in the melting behaviour arising from intrinsic inhomogeneities of the sample.

The columnar defects created by heavy ions serve as strong pinning centers, each columnar defect pins one vortex. It has been shown that high concentration of columnar defects destroys the long-range order of the Bragg glass and form instead the Bose-glass phase[56]. The Bose-glass phase is governed by the pinning energy rather than by the elastic energy and it melts through continuous transition into a liquid phase. On the other hand, a low concentration of columns preserves the first-order transition but can shift it to higher temperatures[26]. The columnar defects reduce the wandering of the flux lines and suppress thermal fluctuations resulting in a higher melting temperature.

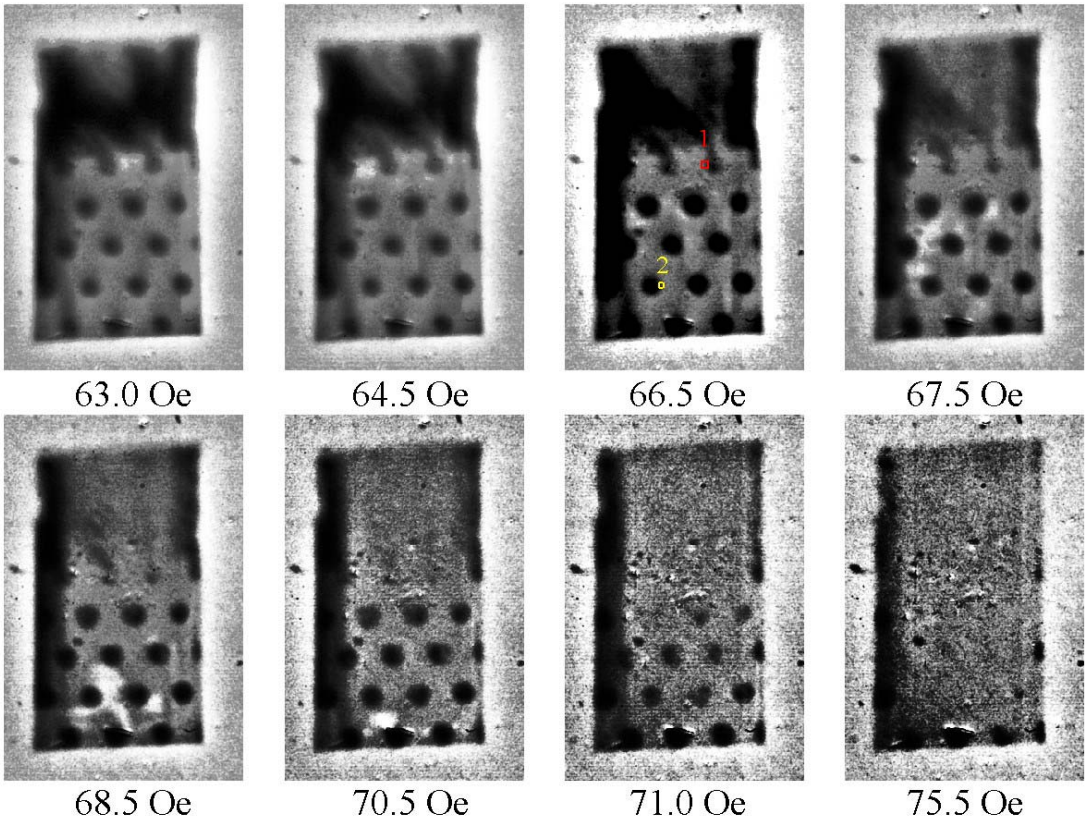

Figure 4.3.1. Differential magneto-optical images of the vortex lattice melting process in selectively irradiated BSCCO crystal of area 0.55 × 1.0 mm^2 at T=70 K using field modulation of δH_a=1 Oe. The equivalent dose of the irradiation is 10 G, which means that at B = 10 G the density of vortices equals to the average density of the columnar defects.

Figure 4.3.1 shows the propagation of the vortex-lattice melting in selectively irradiated BSCCO crystal of area 0.55 × 1.0 mm^2 at T=70 K. The equivalent dose of the irradiation is 10 G, which corresponds to an average distance of one and a half microns between the columnar defects. The irradiated regions (dark) are the areas inside the holes and the top part of the crystal. The diameter of the holes is about 100 μm. We can see the contrast between the irradiated and non-irradiated parts due to the difference in the pinning between them. The irradiated parts screen the change in the external magnetic field δH_a better than non-irradiated parts, which results in the observed contrast between them. The melting first starts in non-irradiated parts of the crystal, near the border with the top irradiated part of the crystal, H_a = 63.0 and 64.5 Oe. With increasing of the magnetic field, liquid phase expands downward through the non-irradiated part of the sample and the melting front (bright) propagates around irradiated holes, H_a = 66.5, 67.5, 68.5, and 70.5 Oe. The image of H_a = 68.5 Oe clearly shows how the liquid phase expands around the irradiated holes without penetrating into them. At higher fields the contrast between the irradiated and non-

irradiated parts starts to disappear, which indicates the expansion of the solid-liquid transition into the irradiated parts, H_a = 71.0 Oe. Finally, almost the entire crystal is in the liquid phase at H_a = 75.5 Oe and the contrast between the irradiated and non-irradiated parts vanishes. The role of disorder in the liquid phase is much less important than in the solid and it is demonstrated by the disappearance of the contrast at the transition. The melting process measured by field modulation demonstrates an upward shift of the transition by correlated disorder but does not reveal the order of the transition.

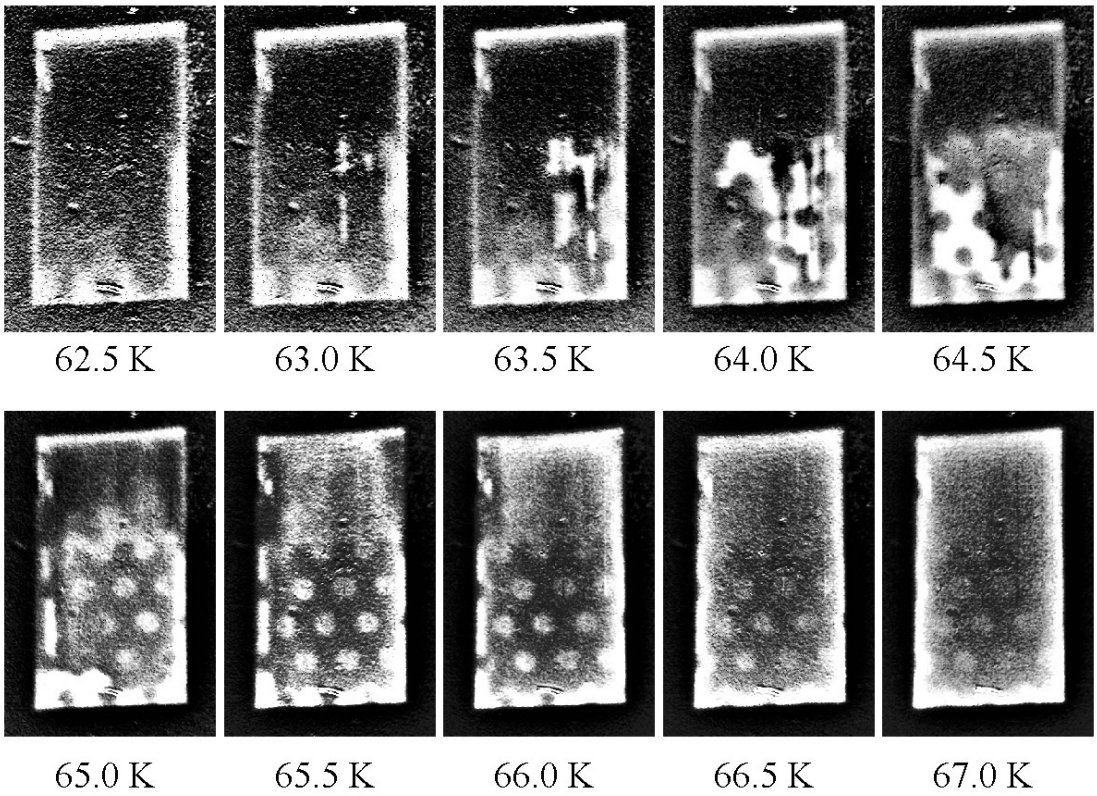

Figure 4.3.2. Differential magneto-optical images of the vortex lattice melting process in selectively irradiated BSCCO crystal of area 0.55 × 1.0 mm^2 using temperature modulation of δT =0.5 K at H_a = 120 Oe.

We have performed another measurement to check the order of the transition in the irradiated regions, in which the temperature was swept instead of the magnetic field and a small temperature modulation was used to obtain the differential image. Figure 4.3.2 shows the differential images of the melting process in the same crystal at H_a = 120.0 Oe using temperature modulation of δT = 0.5 K. At T = 62.5 K the entire crystal is in the solid phase and there is no contrast between the irradiated and non-irradiated parts. At higher temperatures the melting nucleates and propagates in

the non-irradiated parts, which also show several defect structures in the form of vertical lines (bright). At the initial stages the melting front expands around the irradiated holes (T = 63.5, 64.0, 64.5 K). For example, the image at T = 64.5 K shows the formation of the liquid phase around several irradiated holes while the vortices inside the holes remain in the solid phase due to the presence of correlated disorder which stabilizes the vortex solid.

As the temperature is increased further, and after most of the unirradiated regions have melted, the melting starts to occur inside the irradiated holes, T = 65.0, 65.5, 66.0, and 66.5 K. The bright signal inside the holes reveals the enhancement of the local magnetic field at melting that manifests the first-order nature of the transition. However, there are some differences in the melting process in the irradiated and non-irradiated parts. The melting in the irradiated parts is smeared over a wider range of temperatures compare to the melting in the non-irradiated parts. The melting signal inside the holes can be seen in four images, T = 65.0 – 66.5 K, showing the broadening of the transition over $\Delta T \approx 2$ K. In contrast, the melting in non-irradiated parts in each region is seen only during one single image, namely $\Delta T < 0.5$ K. Furthermore, the melting signal in the irradiated regions is weaker. One possible explanation for this phenomenon can be the following. Since the columnar defects are located at random positions their average density may vary from place to place. As a result small domains, each having its own melting temperature are to be expected. The spatial resolution of our measurement in this crystal is about 10μm due to relatively high noise in the images. If the melting nucleates in domains with characteristic sizes less than 10μm, the individual domains cannot be resolved, and instead smearing of the transition should be observed similar to our results. It is important to note that a domain of size $10\times10\mu m^2$ contains on the average 10 columnar defects and about 600 vortices at applied field of H_a = 120 Oe.

Figure 4.3.3 shows the local melting line of the irradiated and non-irradiated parts of the sample in regions in the vicinity of points 1 and 2, marked in Fig. 4.3.1. The melting transition in the irradiated areas is shifted to higher fields relative to the pristine value, and the difference increases with decreasing temperature. The shift caused by the irradiation is small, less than 2 K. Such shift is comparable to the fluctuations in the melting temperature resulting from the intrinsic inhomogeneities in the crystals. The role of intrinsic inhomogeneities becomes more apparent at higher

temperatures as shown in Fig. 4.3.4. The melting in irradiated parts is still shifted to higher temperatures at H_a = 30 Oe as compared to the neighboring locations, but the shift is of the order of the variation in the melting temperature caused by the intrinsic inhomogeneities. For example, at T = 81.0 K the melting happens simultaneously in irradiated and non-irradiated parts as shown correspondingly by blue and red arrows.

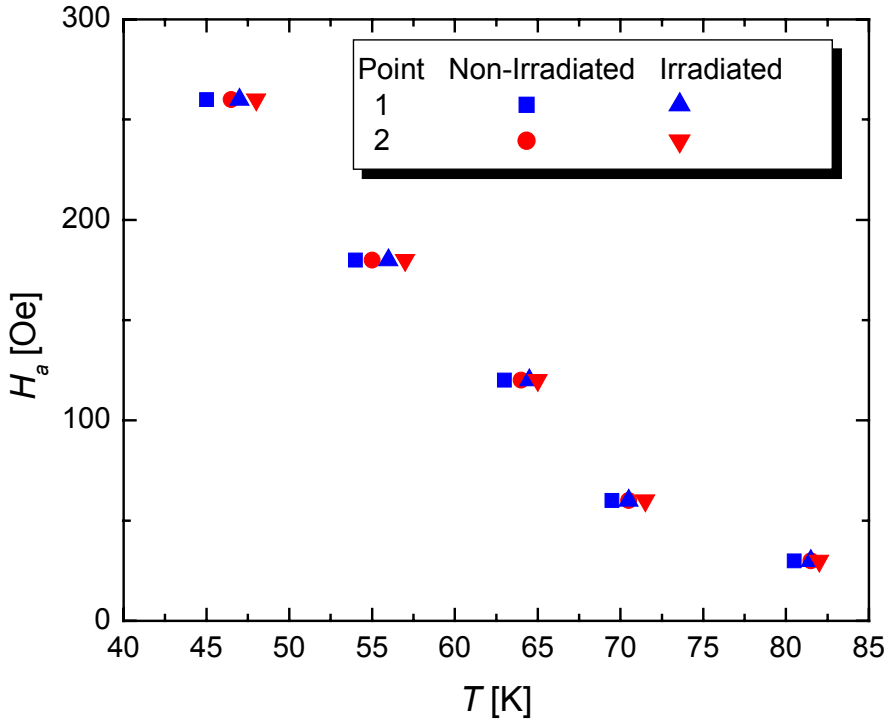

Figure 4.3.3. The local melting field vs. temperature in the irradiated and non-irradiated areas in regions 1 and 2, marked in Fig. 4.3.1.

We have also investigated selectively irradiated crystal with irradiation dose of 100 G (not shown). We have found that the solid-liquid transition in the irradiated regions is apparently of the second order and happens at significantly higher fields. This result is in good agreement with the previous reports[26].

The study of the melting propagation in selectively irradiated crystals demonstrates that a small dose of correlated disorder shifts the melting transition to higher fields and modifies the melting propagation, but preserves the first-order nature of the transition. The analysis of the melting patterns confirms that changes in the pinning strength play a major role in the propagation of the transition at low

temperatures while T_c variations govern the transition at high temperatures. A higher irradiation dose destroys the vortex-lattice melting and results in a second order solid-liquid transition.

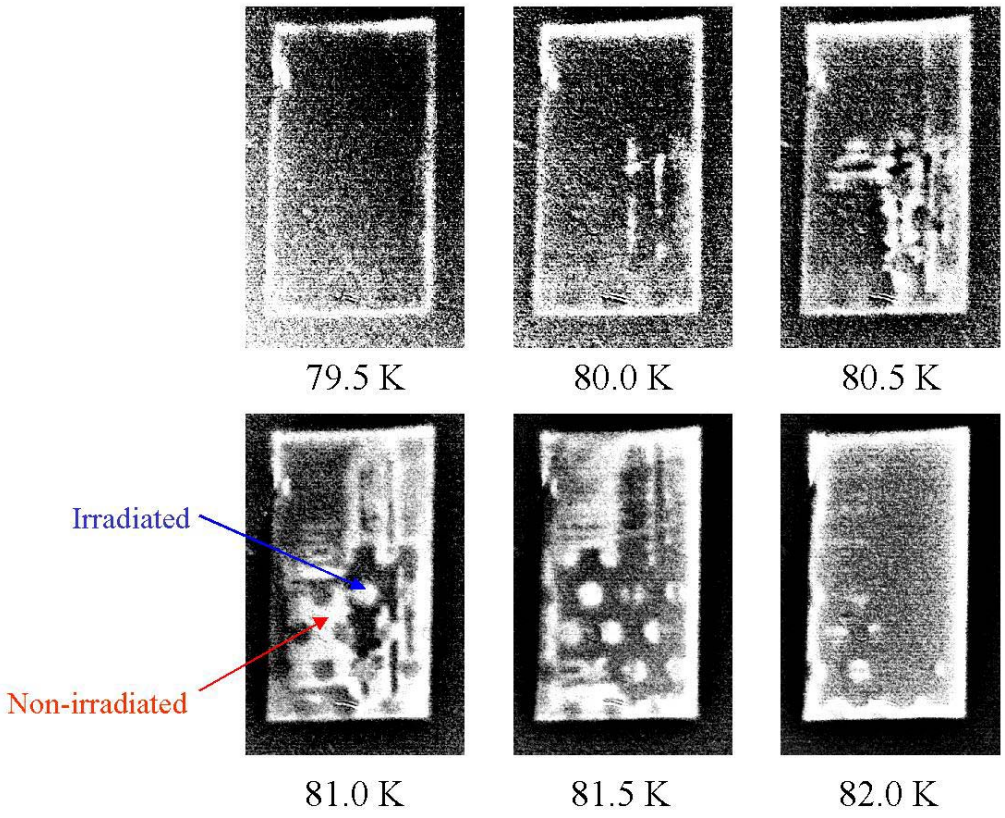

Figure 4.3.4. Differential magneto-optical images of the vortex-lattice melting process in selectively irradiated BSCCO crystal of area 0.55 × 1.0 mm^2 at H_a = 30 Oe, δT = 0.5 K.

5. Appendices

5.1 Appendix I: Intrinsic instability of vortex-lattice melting

We now discuss the intrinsic instability of the vortex-lattice melting and possible formation of solid-liquid laminar structure in a *clean* crystal. The intrinsic instability of the vortex-lattice melting is similar to the intermediate state situation in type-I superconductor. In a thin type-I superconductor sample in perpendicular applied field no uniform solution for the internal field B can be found[57] when the edge field slightly exceeds the critical field H_c. As a result, an intermediate state with complex laminar patterns of intercalated superconductor and normal regions is formed[58]. A similar intrinsic instability of the solid-liquid interface should occur in the melting case, as shown in Fig. 5.1.1. A self-consistent solution for both B and H fields at melting has to be found. Consider that the crystal is in the solid phase, and the corresponding thermodynamic B and H fields across the sample are shown schematically in blue and red correspondingly (Fig. 5.1.1a). If the melting field H_m is less than $H(x)$ in the center, as shown in the figure, a liquid droplet should be formed in the center of the sample where H exceeds H_m. If we solve for the corresponding B and H with the liquid droplet, we find that the increase in B resulting from vortex-lattice melting causes a decrease in H (Fig. 5.1.1b). The resulting H is now lower than H_m which means that we should be back in the solid phase instead of a liquid. Under certain conditions there is no self-consistent solution to this problem[59,60], which may results in instability and in formation of a laminar structure of solid and liquid domains.

Figure 5.1.2 depicts the calculated fields B and H across such a laminar structure for the case of an infinite platelet sample in perpendicular applied field B_a, such that the solid and liquid domains are of equal sizes for example. This Landau type laminar structure may be present in large thin samples where the dome-shaped equilibrium field profile is very flat in the central part of the sample.

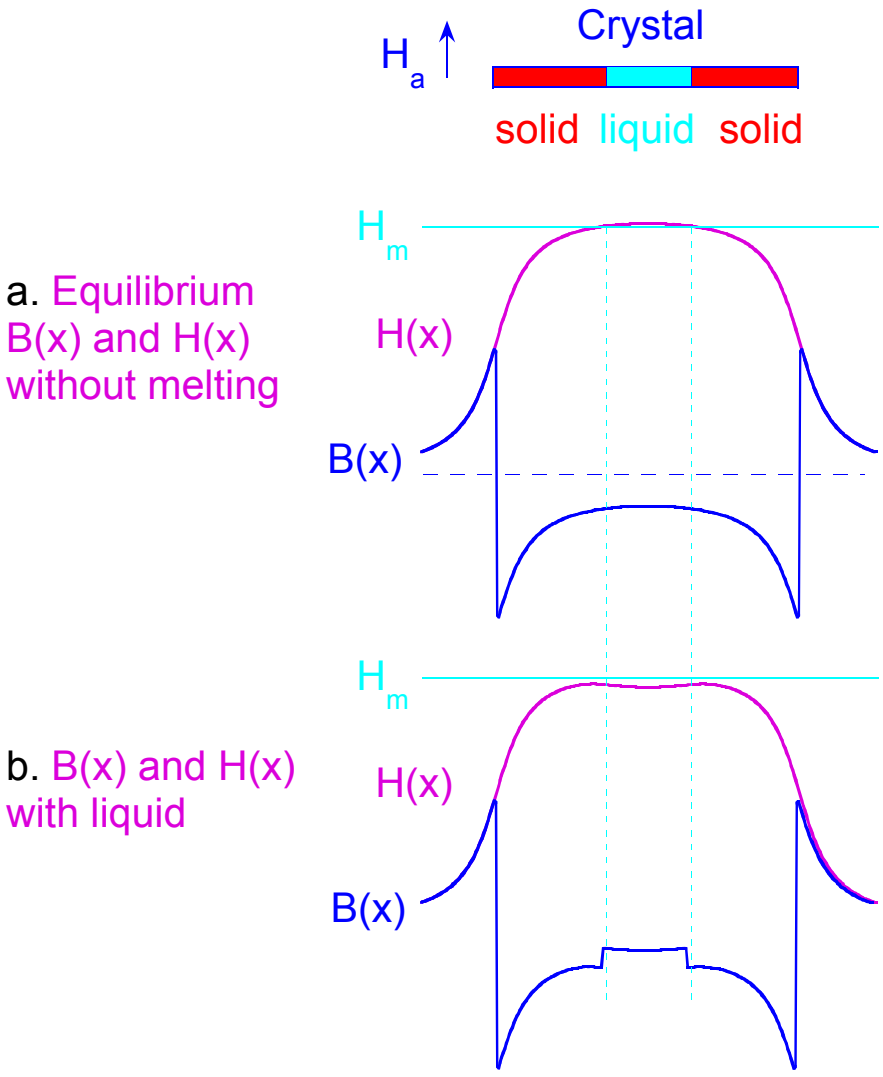

Figure 5.1.1. Illustration of the intrinsic instability at vortex-lattice melting.

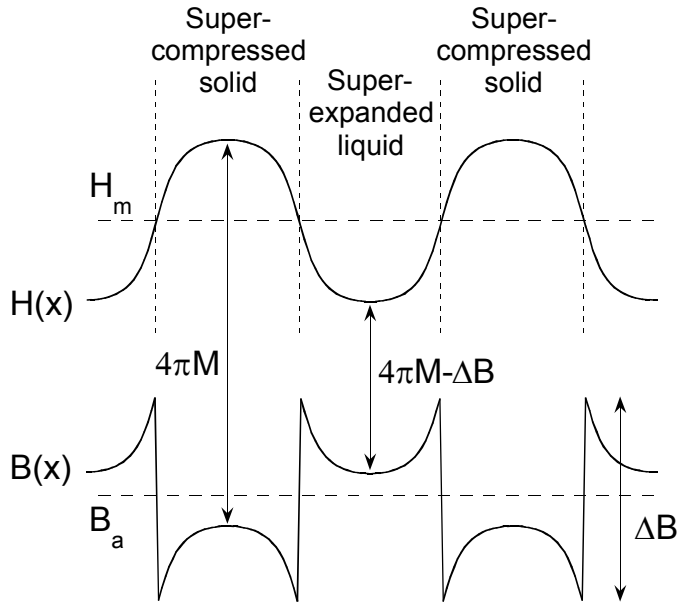

Figure 5.1.2. Calculated *B* and *H* field profiles of a laminar solid-liquid structure in thin infinite sample. The ratio between the laminar period and the sample thickness is *a/d*=8.

Fig. 5.1.3 shows an example of a large BSCCO crystal at $T = 75$ K and $H_a = 67.5$ Oe, where part of the sample resembles a laminar state with numerous periodic solid and liquid domains. In the intermediate state of type-I superconductors the Meissner currents are allowed to flow on the top and bottom surfaces of the superconducting regions, resulting in a uniform $B = 0$ inside the superconducting domains and a uniform $H = H_c$ within the bulk of the entire sample. In our case the situation is quite different since both phases are dissipative, and the current is allowed to flow only along the solid-liquid interface. The field H is continuous across the interface, while the field B has a discontinuous jump of ΔB, see Fig. 5.1.2. This field step, however, is not maintained far from the interfaces due to the two-dimensional geometry of the sample. In particular, in the liquid phase the field B *decreases* away from the interface with a characteristic dependence of d/x, where d is the sample thickness and x is the distance from the interface. Similar, but opposite behavior occurs within the solid phase. The decay of B is accompanied by a corresponding variation of H through the relation $H\text{-}B=4\pi|M|$, where $4\pi|M|$ is the absolute value of the equilibrium magnetization in the solid phase, whereas in the liquid it is reduced to

$4\pi|M|$-ΔB. As a result a *superexpanded* (or supercoold) liquid is formed, in which the field H is *below* H_m, where thermodynamically a solid phase should be present. Similarly, the solid domain is *supercompressed* (or superheated), having H *above* H_m. Thus a very unusual periodic laminar structure of superexpanded liquid and supercompressed solid is formed.

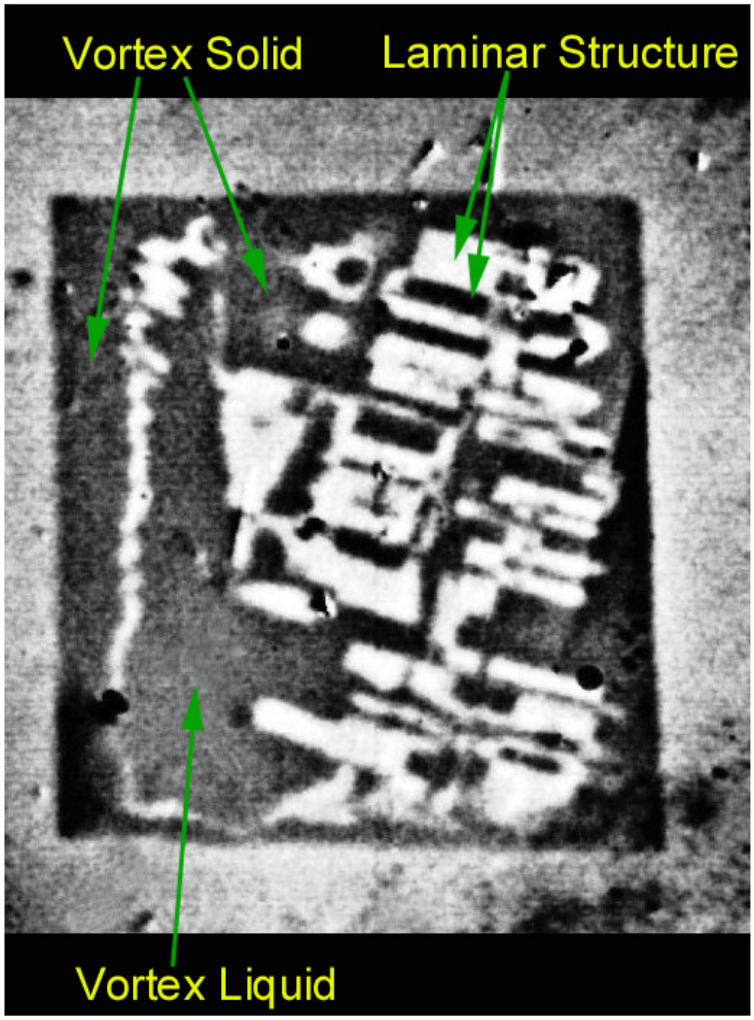

Figure 5.1.3. Solid-liquid domains structure in a large BSCCO crystal of about 1mm aside at T=75 K, H_a= 67.5 Oe.

The intermediate solid-liquid state has been recently studied numerically[59,60]. The one-dimensional electrodynamics calculations of the field profiles show that indeed no self-consistent solution satisfying the required boundary conditions for both

B and H fields can be found, and as a result a dense laminar structure is formed[60] in which the laminar period a is small compared to the sample thickness d. In order to obtain a more realistic estimate of the characteristic laminar period one has to minimize the total free energy[57]. The three dominant energy contributions are the surface tension of the solid-liquid interface, the supercompression and superexpansion of the solid and liquid domains, and the magnetic energy of the field modulation both inside and outside the sample.

Having a laminar structure of period a, the surface tension contributes energy of $E_\sigma \approx 2\sigma d/a$ per unit area of the sample, where surface tension is given by $\sigma \approx \eta a_0 H_m \Delta B/4\pi$. The supercompression / superexpansion term is given by:

$$E_S \approx (d/a)_0 \int^{a/2} (\partial F_s/\partial H - \partial F_l/\partial H)(H(x)-H_m)dx$$

where $\partial F/\partial H$ is the derivative of the free energy in the solid and liquid phases respectively. Using the fact that $\partial F_s/\partial H - \partial F_l/\partial H = \Delta B/4\pi$ we find that in the symmetric case of Fig. 5.1.2, $E_S \approx (\Delta B^2 d/4\pi^2)[\pi/2 - \tan^{-1}(d/a) - (d/2a)\ln(1+a^2/d^2)]$.

Finally, the nonuniform redistribution of the field outside the sample gives rise to the magnetic energy term, which is given by:

$$E_m \approx \int dV(\mathbf{H}\mathbf{h}(\mathbf{r})/4\pi + \mathbf{h}(\mathbf{r})^2/8\pi)/a$$

per unit area of the sample, where $\boldsymbol{H}$ is the uniform field part and $\boldsymbol{h(r)}$ is the spatially variant induced field modulation. The first term here is zero because of the flux conservation $\int dS\boldsymbol{h(r)}=0$. For small a/d the magnetic energy is given by $E_m \approx \Delta B^2 a/8\pi^2$ similar to the type-I superconductor case. For large laminar periods, however, the energy scales as $E_m \approx \Delta B^2 d^2 \ln(a/d)/8\pi^2 a$ due to the d/r decay of the field.

Combining all three energy terms $E_\sigma + E_m + E_S$ and minimizing with respect to the laminar period a, we find $a/d \approx \exp(4\pi\eta H_m a_0/\Delta B d)$ for large a/d, and it reduces to $a/d \approx 10(\eta H_m a_0/\Delta B d)^{1/2}$ in the limit of small a/d. Thus a is very sensitive to the exact prefactors of the various energies. Generally, however, in order to obtain a Landau type laminar structure the surface tension should be small. For large surface tension, in contrast, the resulting a is larger than typical sample size, meaning no laminar structure should be formed and a large volume of supercompressed solid should transform discontinuously into a superexpanded liquid. Also, the above derivation predicts a significant increase of the laminar period as H_m is increased along the melting line.

The formation of the laminar structure due to intrinsic instability of the vortex-lattice melting may be important in the absence of disorder. We have found that laminar structure is irrelevant in our measurements and the disorder is the dominant factor in the properties of the transition. The presence of disorder results in disorder-induced melting landscape $H_m(x,y)$ which governs the vortex-lattice melting (§4.1). The introduction of the position dependent melting landscape $H_m(x,y)$ does not fully solve the problem of intrinsic instability, but the above analysis of the laminar structure becomes irrelevant. Instead, the melting transition should be described by the theory of first-order transition in disordered systems[37]. The solid-liquid patterns seen in Fig. 5.1.3 reflect the underlying disorder-induced melting landscape $H_m(x,y)$ rather than formation of the laminar structure due to instability. Furthermore, the observed change of the melting patterns along the phase-transition line results from the variation of $H_m(x,y)$ with temperature as described in §4.2, and does not follow from the increase of the laminar period with H_m.

5.2 Appendix II: Visualization of the transport current

The origin of finite resistivity in type-II superconductors is the vortex motion induced by transport current. The current flowing in the superconductor exerts a Lorentz force on the flux lines. The competition between the Lorentz force and the pinning of the vortices by disorder determines the resistivity of type-II superconductors. The pinning depends strongly on the vortex phase and therefore the resistivity measurements are a common investigation tool in type-II superconductors. In order to understand the property of the vortex matter from the transport measurements, the flow pattern of the current needs to be known. In most of the experiments the current flow is assumed to be uniform across the sample like in a normal metal. However, it has been demonstrated recently[61,62,63] that the current flow is not uniform and it changes with field and temperature. Furthermore, the current distribution depends not only on the phase of the vortex matter but also on other mechanisms, like surface barriers, which cause a highly non-uniform flow. These findings are of significant importance for proper interpretation of the resistivity measurements.

The previous studies[61,62,63] were carried out using Hall sensor technique, which provides only one dimensional profile of the current flow. The obtained profiles were insufficient to give a complete explanation for the observed data. In particular, it was not possible to evaluate the influence of disorder and inhomogeneities on the current flow. We have applied the developed differential magneto-optical technique to study how the transport current flows in BSCCO crystals. The main advantage of the developed method is the ability to provide a two-dimensional visualization of the flow of small transport currents with extremely high resolution. It is important to note that conventional MO technique was successfully applied only for study of current flow in HTS tapes and films where large currents can be applied[64]. These devices are of major importance for practical applications of superconductors.

The procedure for current visualization with differential MO technique is described in §3.2.4. In brief, the difference between the magneto-optical images taken with and without the current flowing in the crystal, results in an image of the self-induced magnetic field generated by the current. In fact, in order to avoid any possible

temperature variations due to heating at the contacts with and without current, the images are taken instead with positive and negative applied current and subtracted accordingly. The resulting differential images of the self-induced magnetic field have to be calibrated in order to derive magnetic field values from the grayscale of MO image as described in §3.2.5. The two-dimensional current flow can be calculated from the self-field by inversion of the Biot-Savart law. We have used the fast inversion scheme developed by Wijngaarden *et. al.*[43,44] and the inversion programs were generously provided by the authors. The programs were slightly modified in order to run under the IDL program instead of Matlab.

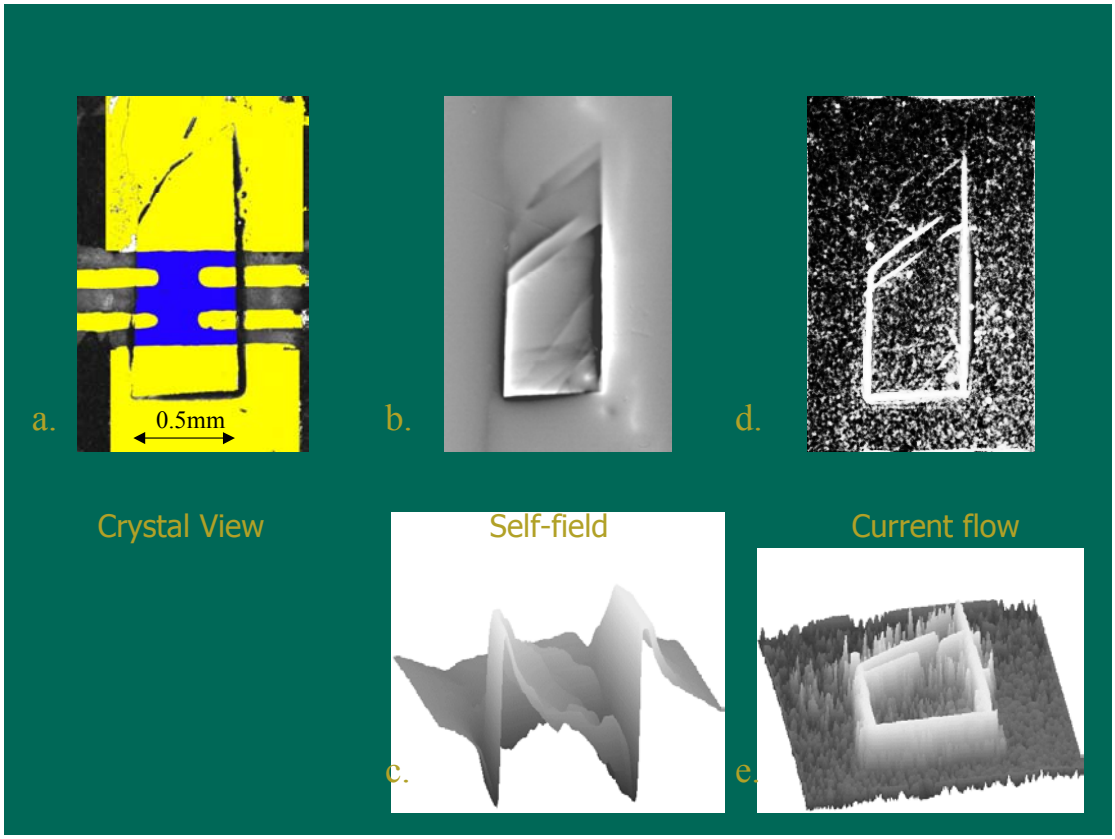

Figure 5.2.1. a) Image of BSCCO crystal (blue) with evaporated gold contacts (yellow). The large top and bottom contacts are used for current injection and the narrow contacts are for voltage measurements. b) Images of the self-field, created by a current of I = 30 mA flowing in the crystal at T = 75 K and H_a = 25 Oe. c) 3d presentation of the self-field image in the central part of the sample. d) The current distribution calculated from self-field image by inversion of Biot-Savart law. e) Schematic 3d presentation of the current distribution.

Figure 5.2.1a shows image of BSCCO crystal (blue) with evaporated gold contacts (yellow). The current contacts are in the top and bottom parts of the image, and the contact resistance is about 2 Ohm. Figure 5.2.1b is the differential magneto-optical image of the self-field, generated by a current of I = 30 mA flowing in the

crystal at T = 75 K in the presence of an applied field of H_a = 25 Oe. The bright color corresponds to a positive magnetic field directed upward and dark corresponds to magnetic field in the opposite direction, while a zero field is middle-gray. A schematic 3d representation of the self-field in the central part of the sample is presented in Fig. 5.2.1c. The amplitude of the self-field is very low, about 300 mGauss, which can be measured only by our differential method.

The image of the self-field shows a highly non uniform current flow in the crystal and reveals the influence of defects and disorder. Several line defects, which are not detectable by other measurement techniques, are clearly visible. Figure 5.2.1.d shows the current density derived from the self-field by inversion of the Biot-Savart law as described above. The 3d representation of the current density is given in Fig. 5.2.1e. The current flows at the edges of the crystal due to the surface barriers[61] and in the upper part of the sample the current flows into the contact along the defects. This image reveals that defects modify the current flow in type-II superconductors and therefore should play an important role in the interpritation of the transport measurements.

An interesting phenomenon is found at the contacts. The gold current contacts cover significant area of the crystal. Yet the edges of the crystal and the crystallographic defects under the contacts are clearly seen in the images. This indicates that current enters into the sample mainly at the edges or along the defects. In the bottom contact, which apparently is not perfect, most of the current enters at the right-bottom corner and flows upward along the right edge and to the left along the bottom edge. In the top contact, the current exits along the right edge and along the line defects. Furthermore, the entrance point of the current into the sample is found to change with temperature or the applied field as described below.

Figure 5.2.2 shows images of the self-field taken at several temperatures at constant applied magnetic field H_a = 25 Oe. The images at the bottom are the calculated current flow patterns. At high temperatures, above and below T_c = 91 K, the current flows almost uniformly between the bottom and the top electrical contacts and the current flow does not change below the superconductivity transition T_c. Some crystallographic defects, which distort the current flow, are clearly visible in the images. At the vortex-lattice melting temperature, T = 85 K, the current flows within the crystal along the defects and along the edges. At T = 75 K the current flows mainly along the edges due to the surface barriers, and in the upper part current enters

into the contact along the defects. It is interesting to note that at high temperature, above and below T_c, the current avoids the defects (dark regions in the current image) whereas below T_c opposite behavior is found in which the current is attracted towards the defects (bright lines). This effect can be explained as following. At high temperatures, above and below T_c, when the current flow is uniform, the defect has a low conductivity compared to the bulk and therefore the current avoids it. At low temperatures vortex pinning becomes important and the defect serves as a strong pinning center. The enhanced critical current along the defect, which is required to induce vortex motion perpendicular to the defect, results in low resistivity and thus the current redistributes itself to flow along the defect.

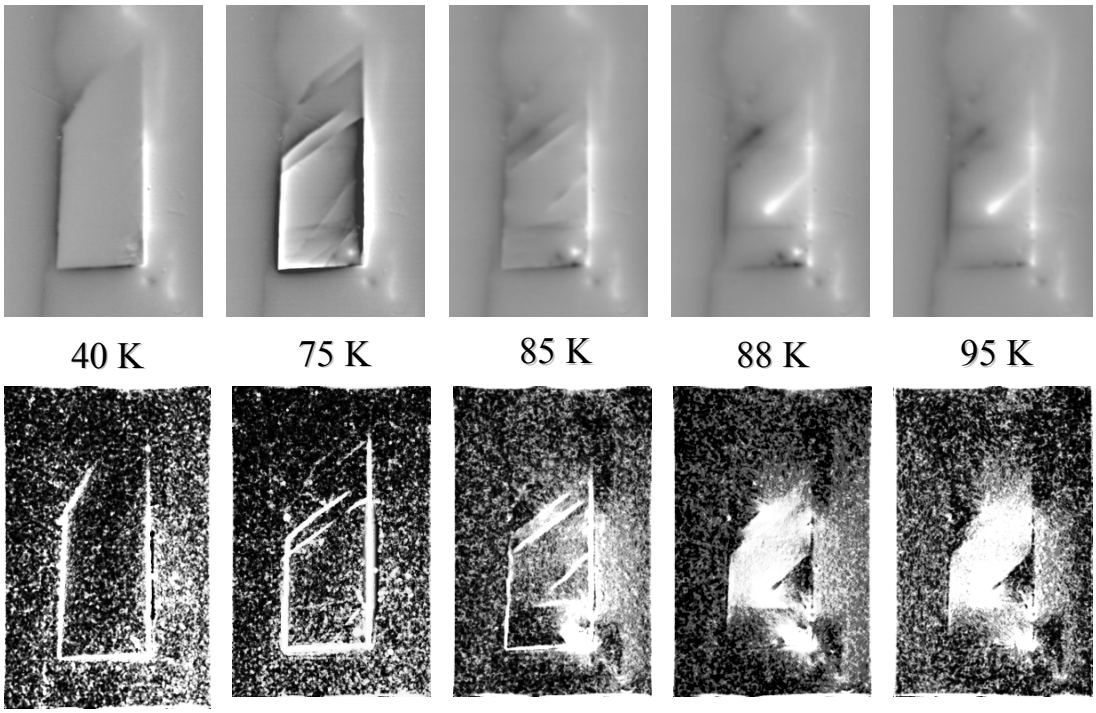

Figure 5.2.2. The images of the self-field (I = 30 mA) taken at several temperatures at H_a = 25 Oe (top) and the corresponding calculated current distribution (bottom).

As the temperature is decreased to 40 K, the current flows mainly near the edges. In contrast to the apparent similarity between the current flow at T = 75 and 40 K, the field distribution is completely different. It can be seen by comparing the images of the self-field at T = 75 K and 40 K. At T = 40 K the vortices are immobile

and the transport current flows as a Meissner current which completely screens the self-field and results in zero value of the self-field in the entire volume of the sample. In the 'Meissner state', the current flows not only at the edges, but also on the top and bottom surfaces of the crystal. The effective sheet current density decays rapidly but continuously from the edges of the crystal, in contrast to the current distribution given by a δ-function near the edges in the case of surface barriers.

The injection of the current from the contacts into the sample also changes with temperature. When the flow in the sample is uniform, at T = 88 K and 95 K, the current injection from the bottom contact is almost uniform and occurs mainly along the upper boundary of the contact. At lower temperature T = 75 K, when the current flows along the edges and pinning become significant, the current enters at the corner along the edges, or along the defects. At T = 40 K all the current enters along the edges from the lower right corner.

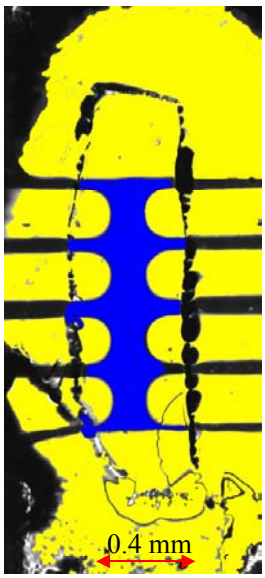

Figure 5.2.3. Image of additional BSCCO crystal with evaporated gold contacts. The large top and bottom contacts are used for current injection and the narrow contacts are for voltage measurements.

We have studied the current distribution in another crystal shown in Fig. 5.2.3. The top row of images in Fig. 5.2.4 are the self-field created by the transport current I

= 10 mA at several temperatures at constant applied magnetic field H_a = 25 Oe. The images at the bottom are the current distributions obtained by inversion of the self-field. At high temperature T = 95 and 90 K, which are above and below T_c = 91 K, the current flows almost uniformly between the top and the bottom current contacts. At these temperatures, the current distortion is clearly seen in the upper part of the crystal where the current flow avoids the macroscopic defect. As the temperature is decreased to T = 80 K, the current flows along the edges and along the defect. The influence of the defect on the current flow decreases with the temperature and most of the current flows along the edges, T = 70 and 60 K. Finally, at T = 40 K the transport current flows as a Meissner current and the self-field is zero in the entire volume of the crystal. The changes in the current flow are exactly the same as observed in the first crystal discussed in the beginning of this appendix. Yet the exact current distribution differs between the crystals and is defined by underlying sample disorder.

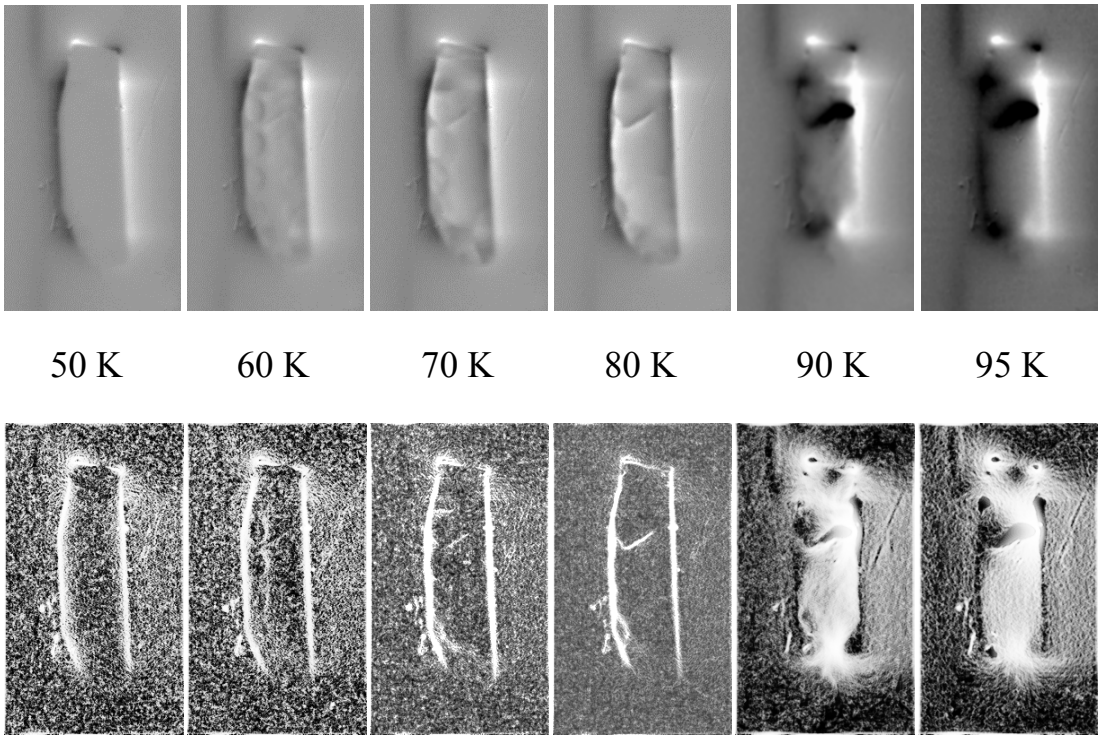

Figure 5.2.4. The images of the self-field (I = 10 mA) taken at several temperatures at H_a = 25 Oe (top) and the corresponding current distributions (bottom).

Our measurements confirm the recently published work[61], which demonstrated the change of the current distribution from uniform to the edge flow. In addition to the

current redistribution due to the presence of surface barrier, however, our measurements have revealed that disorder again plays an important role and modifies the current distribution. The MO images of the current flow also demonstrate the difficulties in proper interpretation of the resistivity data. Since the current flow is so complex, the resistivity does not necessarily reflects the property of the vortex state but rather the sophisticated mixture of different parameters such as the exact current patterns, properties of the surface barriers, and the defect structure.

5.3 Appendix III: Simultaneous MO and transport measurements

The resistivity measurements are an important tool for probing the properties of the vortex matter. The first indications of the vortex-lattice melting transition have been obtained by the observation of the sharp resistivity drop at the transition[5,6,7]. The drop in the resistivity was associated with the onset of pinning in the vortex solid. Since the discovery of the equilibrium magnetization step at the vortex-lattice melting, there were several attempts to find the correlation between the magnetic and transport properties at the transition[9,65,66]. It has been demonstrated that the magnetization step and resistivity onset occur concurrently at the first-order vortex-lattice phase transition in BSCCO[9,66]. But as discussed in §4.1, the presence of disorder results in the disorder-induced melting landscape that smears the vortex-lattice melting transition. The disorder results in a complicated propagation of the transition and in coexistence of the solid and liquid domains. The vortex potential landscape is determined by the intrinsic disorder, which is quenched during the crystal growth process and is uniquely defined for each sample. Furthermore, a proper interpretation of the transport measurements requires knowledge of the current flow. The flow of the current changes with the temperature and the applied magnetic field and depends not only on the phase of the vortex matter but also on the surface barriers and the disorder.

The relation between the propagation of the vortex-lattice melting transition and the transport properties may depend on the disorder distribution as well as on the geometry of the sample. On other hand, the vortex-lattice melting is associated with an abrupt change in the pining properties. The change in the pinning is reflected in the resistivity and thus a correlation between the melting propagation and the transport measurements is expected to be found. In order to find this correlation, the melting transition, current flow, and resistivity have to be measured simultaneously. The developed differential MO technique allows two-dimensional visualization of the vortex-lattice melting as well as of the current distribution on a microscopic scale across the entire crystal. The MO imaging in combination with the resistivity measurement presents therefore a unique tool, which allows simultaneous study of all the relevant parameters. We have explored the advantages of the combined MO and

transport measurements to study the melting propagation and the resistivity simultaneously.

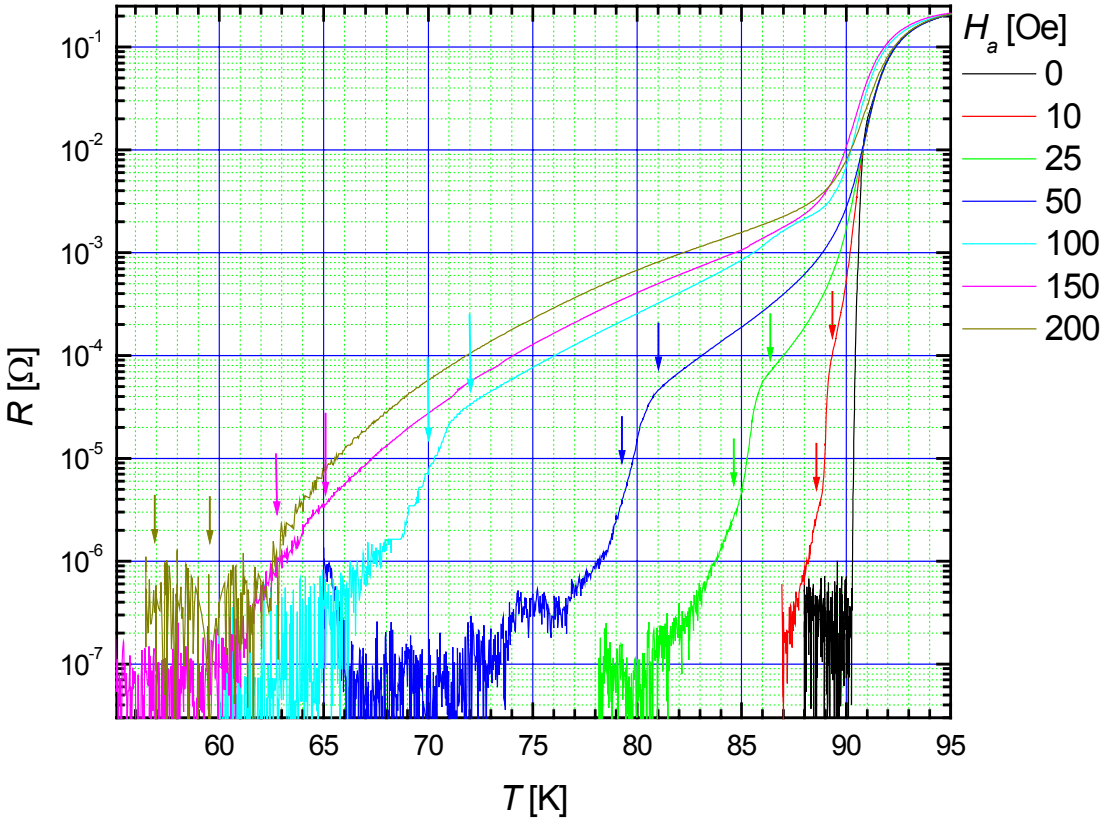

Figure 5.3.1. Simultaneous MO and resistivity measurements in BSCCO crystal shown in Fig 5.2.3. The resistivity is plotted on a logarithmic scale vs. temperature at various applied magnetic fields. The arrows show the nucleation (left arrow) and completion (right arrow) of the vortex-lattice melting. The color of the arrows matches the corresponding resistivity curves.

Figure 5.3.1 shows the results of simultaneous MO and resistivity measurements in BSCCO crystal shown in Fig 5.2.3. The resistance is plotted on a logarithmic scale vs. temperature at various applied magnetic fields. The transport current I = 10 or 30 mA flows between the top and bottom contacts, while the voltage is measured between the side contacts using lock-in technique. For each field arrows show the temperature of nucleation and completion of the vortex-lattice melting transition as visualized by the differential MO technique. The left arrow corresponds to the nucleation of the first liquid droplets while the right arrow marks when the entire crystal is in the liquid phase.

The resistance drop at the melting transition is clearly seen at low fields H_a = 10, 25, 50 Oe. As the magnetic field is increased and the vortex-lattice melting occurs at lower temperature, the resistance changes at the transition become smaller, H_a = 100 Oe. At H_a = 150 Oe no pronounced change in the resistance is observed at melting. Finally, at H_a = 200 Oe the resistance in the liquid phase in the vicinity of transition is very small, less than 10^{-7} Ohm, which is below our resolution. Still the melting propagation is clearly seen in MO imaging up to fields of about H_a = 300 Oe. Figure 5.3.2 presents the values of the resistance at the nucleation and at the end of the vortex lattice melting. The relative change of the resistance at the transition decreases more than by order of magnitude as we go down along the melting line from H_a = 10 Oe (T = 89 K) to H_a = 150 Oe (T = 63 K). Also the resistance in the liquid phase just prior to solidification decreases significantly, falling down below our resolution at H_a = 200 Oe. At low fields, a finite resistivity below the transition in the solid phase can be measured since the current is rather high and non-linear effects are important[62].

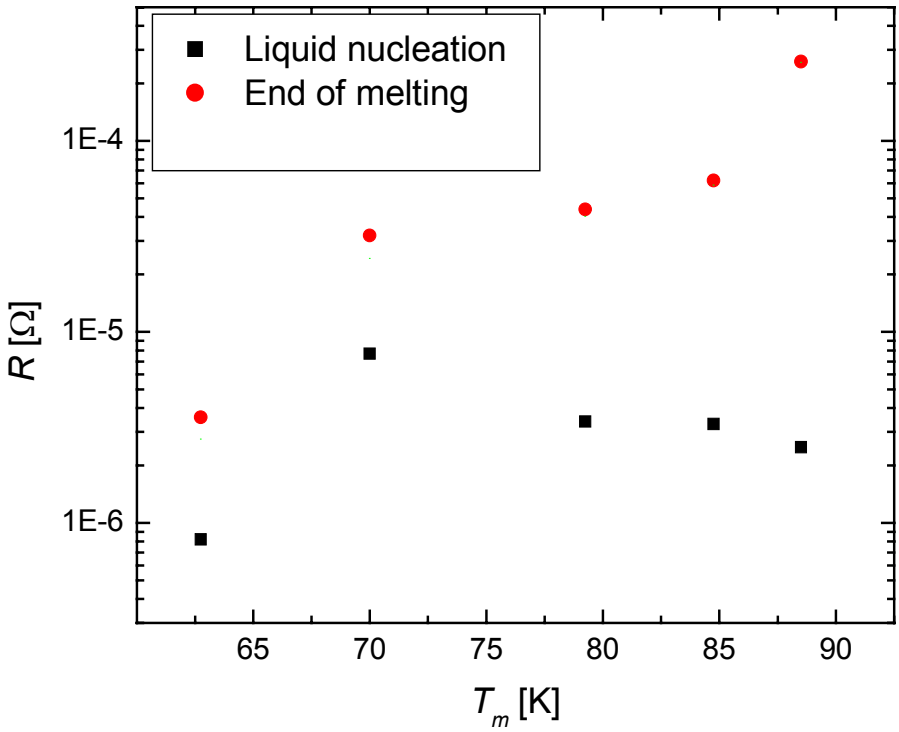

Figure 5.3.2. The resistance at nucleation and at the end of the vortex-lattice melting plotted on a logarithmic scale vs. the mean-field transition temperature. The difference between the resistance at the end of the melting and at the nucleation is the resistance drop at the transition.

The current distribution should be analyzed first in order to make proper interpretation of the resistivity measurements. The current flow in this crystal is shown in Fig. 5.2.4 over a wide interval of temperatures and discussed in §5.2. Here we want to concentrate in particular on the change in the current distribution in the vicinity of the vortex-lattice melting. Figure 5.3.3 shows the profiles of the self-field across the crystal in the central region of the sample. The self-field images were taken simultaneously with the melting visualization and the resistivity measurements at H_a = 25 Oe. At T = 86.5 K, when the entire crystal is in the liquid phase, the field distribution corresponds to a uniform current flow across the crystal. As the temperature is decreased, the freezing starts near the edges and a vortex solid phase is formed in these regions. The surface barrier increases significantly in the solid phase[67] and the resistivity in the solid is much smaller than in the liquid. The current prefers to flow along the edges where the resistivity is low and the redistribution of the current from uniform to the surface flow is observed at T = 85.5 and 85.0 K. After the freezing is completed and the entire crystal is in the solid phase at T = 84.5 K, almost all of the current flows along the edges. The observed change in resistivity at the transition therefore reflects not only the onset of pinning in the solid phase but also the increase of the surface barriers and the redistribution of the current from uniform to edge flow.

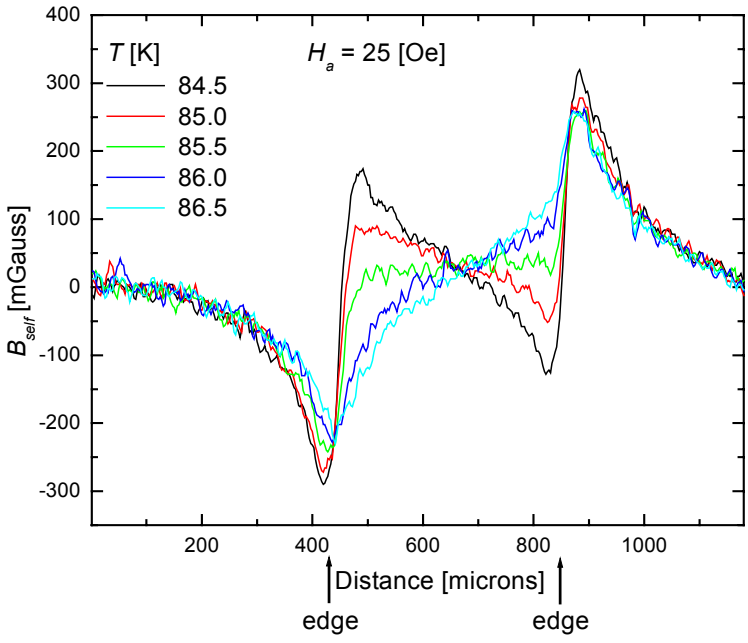

Figure 5.3.3. The profiles of the self-field across the middle of the crystal at various temperatures, H_a = 25 Oe and I = 10 mA.

The surface barriers also exist in the liquid phase and their role grows as the temperature is decreased[61]. At H_a = 100 Oe, the current flow above the melting is superposition of a uniform and edge currents as shown in Fig. 5.3.4 at T = 73.27 K. The redistribution of the current due to a defect is seen as a small bump of the self-field in the left part of the crystal. This defect apparently results from the contact evaporation and can be seen in the Fig. 5.2.4 image at T = 60 K as a series of half-circles. As the temperature is decreased, the freezing occurs and current flow gradually changes. At T = 69.27 the entire crystal is in the solid phase and the current flows primarily along the edges. The observed current redistribution at the transition is small since a significant part of a current already flows along the edges even in the liquid phase. The resistivity reflects not only the properties of the bulk but also transmittivity of the vortices through the surface barrier. The surface barrier lowers the resistivity and reduces the change in the resistivity upon freezing, as shown in Figs. 5.3.1 and 5.3.2.

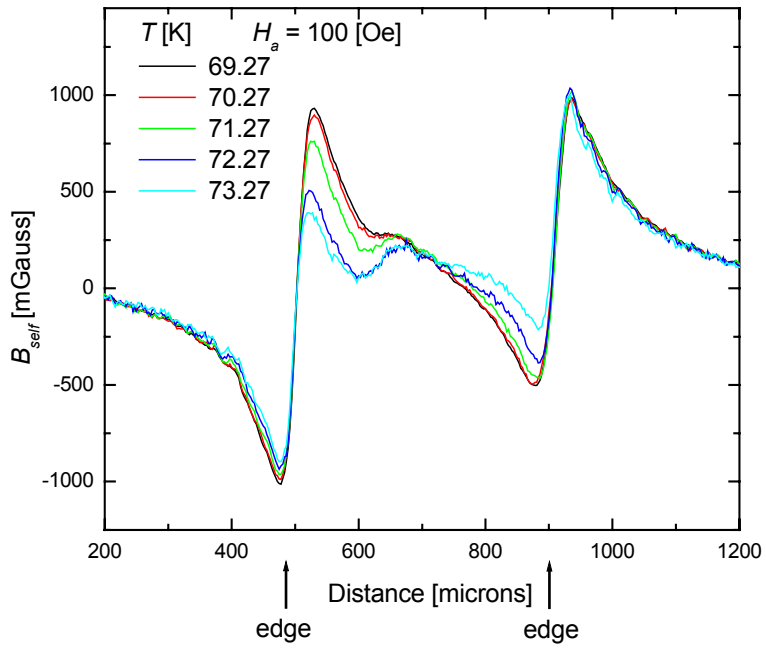

Figure 5.3.4. The profiles of the self-field across the middle of the crystal at various temperatures, H_a = 100 Oe and I = 30 mA.

At higher fields most of the current starts to flow along the edges already in the liquid phase. Figure 5.3.5 shows the self-field profiles in the vicinity of the vortex-

lattice melting at H_a = 150 Oe. At T = 65 K when the entire crystal is in the liquid phase, the current flows along the edges and along the defect. The current flow across the crystal does not change significantly upon freezing. There is only a minor redistribution of the current between the left edge and the defect, but the constant profiles of self-field in the center and in the right part of the crystal clearly demonstrate that the current distribution does not change appreciably across the transition. The surface barrier is expected to increases significantly in the solid phase. Thus the changes in the resistivity should be observed, but apparently it is too small at elevated fields.

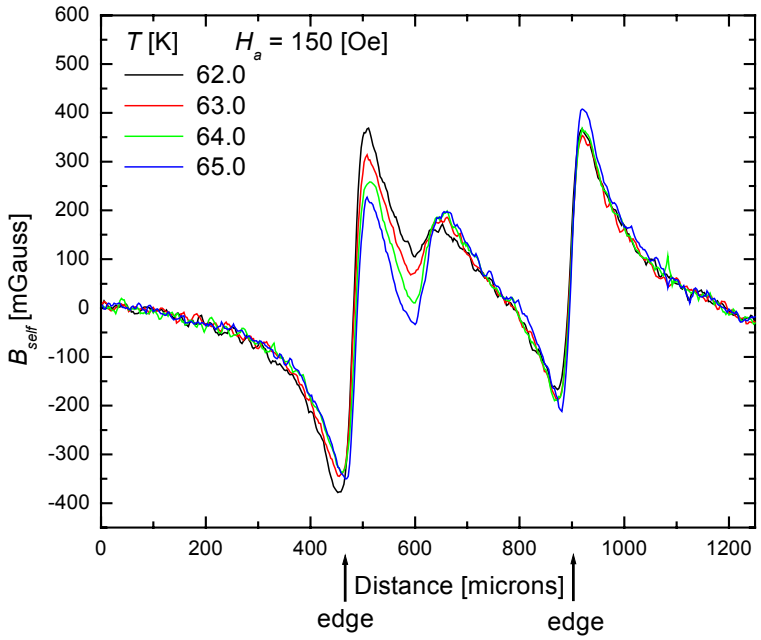

Figure 5.3.5. The profiles of the self-field across the middle of the crystal at various temperatures, H_a = 150 Oe and I = 10 mA.

Finally, the resistivity in the liquid phase becomes too small to be resolved due to the increase of the surface barriers at low temperature. At H_a = 200 Oe, the resistance drops below our resolution at $T \sim 61$ K, while the freezing starts only at T = 59.5 K.

We now analyze in more detail the correlation between the propagation of the vortex-lattice melting transition and the changes in the resistivity. The correlation should be more pronounced at low fields where the surface barrier is small and does

not govern the transport properties. Figure 5.3.6 shows the contours of the liquid phase as function of temperature at H_a = 25 Oe. When the solid phase forms near the edges at T = 85.5-86.0 K, the resistivity starts to drop sharply as shown in Fig. 5.3.7. At T = 85 K the solid phase exists only in thin strip along the edges, but already more than half of the current redistributes to flow at the edges as compared to the uniform flow at T = 86.0 K (inset of Fig. 5.3.7.) The main change in the resistivity occurs in the interval T = 85.0 – 85.5 K, when the bulk melts (green-yellow-orange-red contours) and current has almost completed the redistribution to the surface flow. At temperatures below 85.0 K, there are still several liquid droplets present. Apparently their influence is small, and the resistivity decreases smoothly and does not exhibit pronounced changes upon the completion of freezing. The small modification of the current flow is still observed below T = 85 K due to the increase of the surface barrier with decreasing temperature.

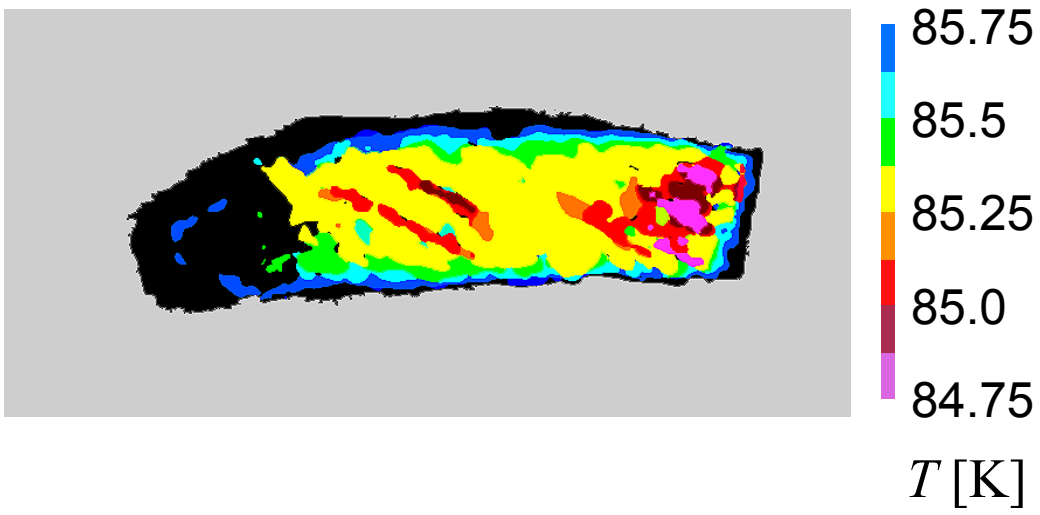

Figure 5.3.6. Contours of the liquid phase at various temperatures at 0.125 K intervals, H_a = 25 Oe.

The simultaneous MO and transport measurements have revealed the complex correlation between the melting propagation and the resistivity change at the transition. It has been demonstrated that when the melting occurs at high temperature

and low fields then the onset of the surface barrier governs the transport properties. The enhancement of the surface barrier changes the current flow from uniform to edge flow and results in a significant resistivity drop at the transition. The current redistribution starts when the solid phase forms near the edges and the main change in the resistivity happens when the bulk undergoes the transition. At higher fields a significant part of the current flows along the edges even in the liquid phase. Thus the observed current redistribution as well as the resistivity drop is much less pronounced at higher fields. At still higher fields the surface barrier shunts almost the entire current and reduces the resistivity beyond our resolution. Also the current distribution shows almost no change at the transition.

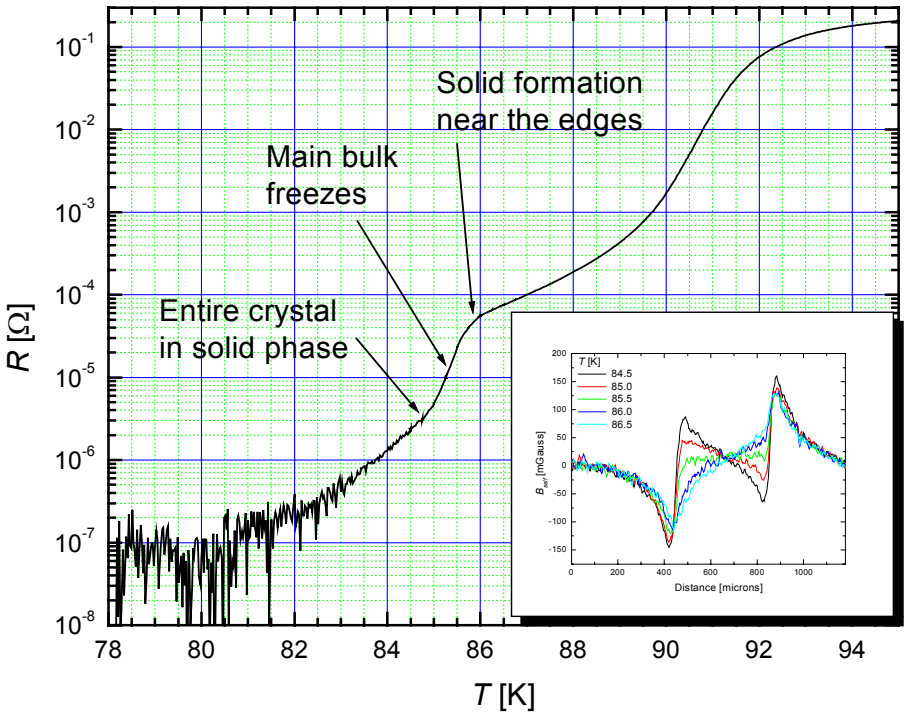

Figure 5.3.7. The resistance is plotted on a logarithmic scale vs. temperature at H_a = 25 Oe, I = 10 mA. The arrows designate the stages of the vortex-lattice melting as extracted from the melting contours, Fig. 5.3.6. Inset: The profiles of the self-field at various temperatures, H_a = 25 Oe and I = 10 mA (from Fig. 5.3.3).

5.4 Appendix IV: Current redistribution near T_c

While visualizing the current flow in BSCCO, we have found an unexpected current redistribution near the superconductivity transition. Figure 5.4.1 shows the images of the self-field (top row) generated by the transport current I = 30 mA in BSCCO crystal at H_a = 25 Oe at various temperatures in the vicinity of T_c = 91 K. The bottom row presents the images of the current density derived from the self-field by inversion of the Biot-Savart law (§5.2). The image of the crystal with evaporated contacts is shown in Fig. 5.2.1a. The current redistribution over a wider range of temperatures is demonstrated in Fig. 5.2.2 and discussed in §5.2. Here we want to concentrate only on the behavior near T_c.

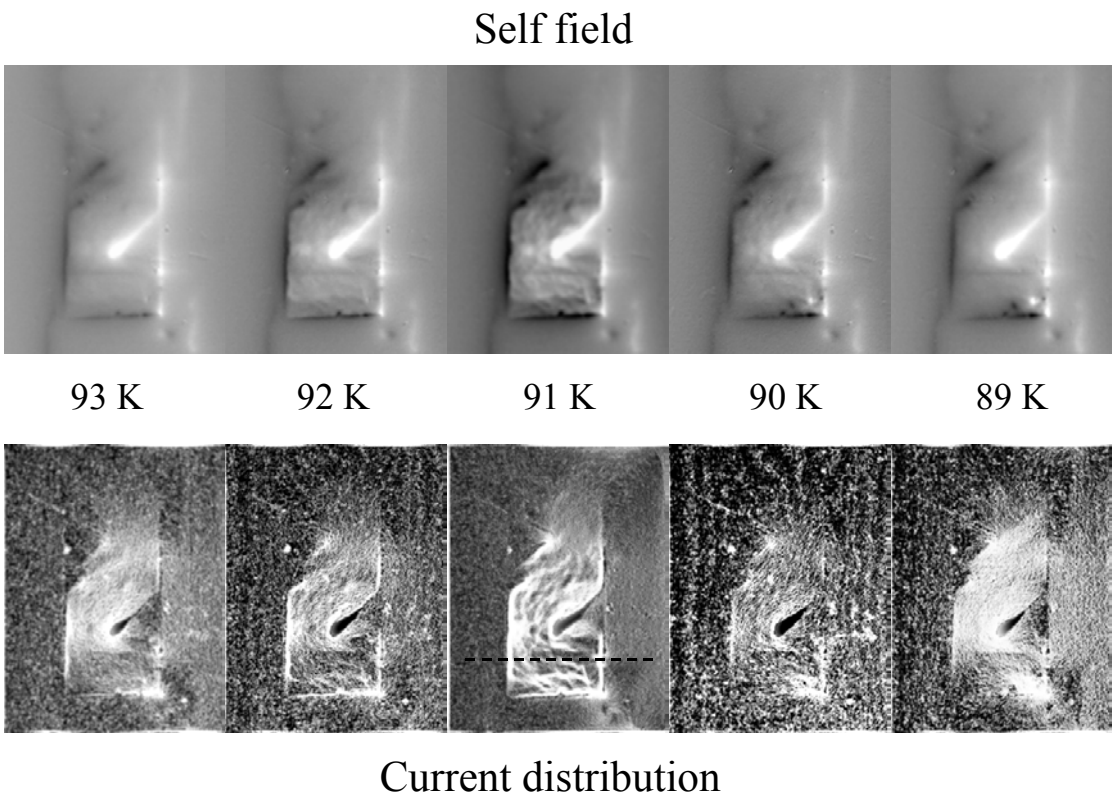

Figure 5.4.1. Images of self-field (I = 30 mA) taken at several temperatures at constant applied magnetic field H_a = 25 Oe (top) and the derived corresponding current distribution (bottom).

Slightly above and below T_c, at T = 93 and 89 K, the current flows almost uniformly between the bottom and the top electrical contacts, except the distortion of the current due to the presence of the macroscopic defects as discussed in §5.2. As the temperature approaches T_c, the current flow starts to change and becomes non-

homogeneous, see T = 92 and 90 K images. The current distribution reaches maximum inhomogeneity near T_c = 91 K where the formation of channel-like structures is clearly seen in the self-field and the current density images. The local variation in the current density at T_c are very significant as seen in Fig. 5.4.2, which shows the profiles of the current density along the dashed line marked in T = 91 K image in Fig. 5.4.1. The local current density at T_c = 91 K varies by a larger factor across the crystal and, in addition, a large fraction of the current flows at the edges of the sample.

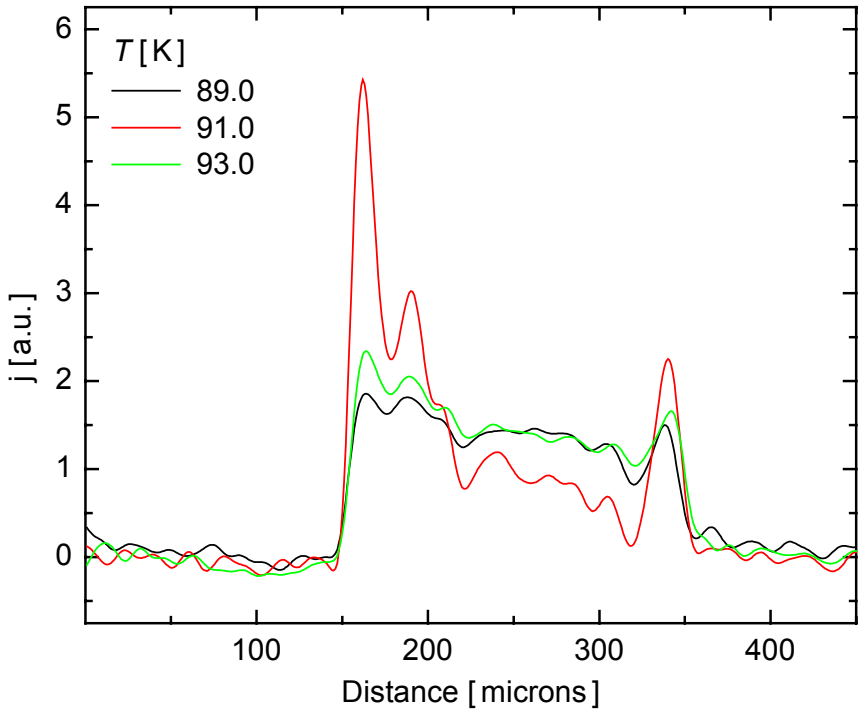

Figure 5.4.2. The profile of the current sheet density at H_a = 25 Oe and T = 91 K along the line marked in Fig. 5.4.1.

The observed current redistribution apparently does not depend on the amplitude of current. The images of the self-field generated by current of 10 and 30 mA at T = 91 K and H_a = 50 Oe are presented in Fig. 5.4.3. The increase of the current results in higher values of the self-field (see gray-scale bar), but does not modify significantly the current redistribution. A detailed analysis of the self-field images at I = 10 and 30 mA reveals that the current continues to flow along the same channels.

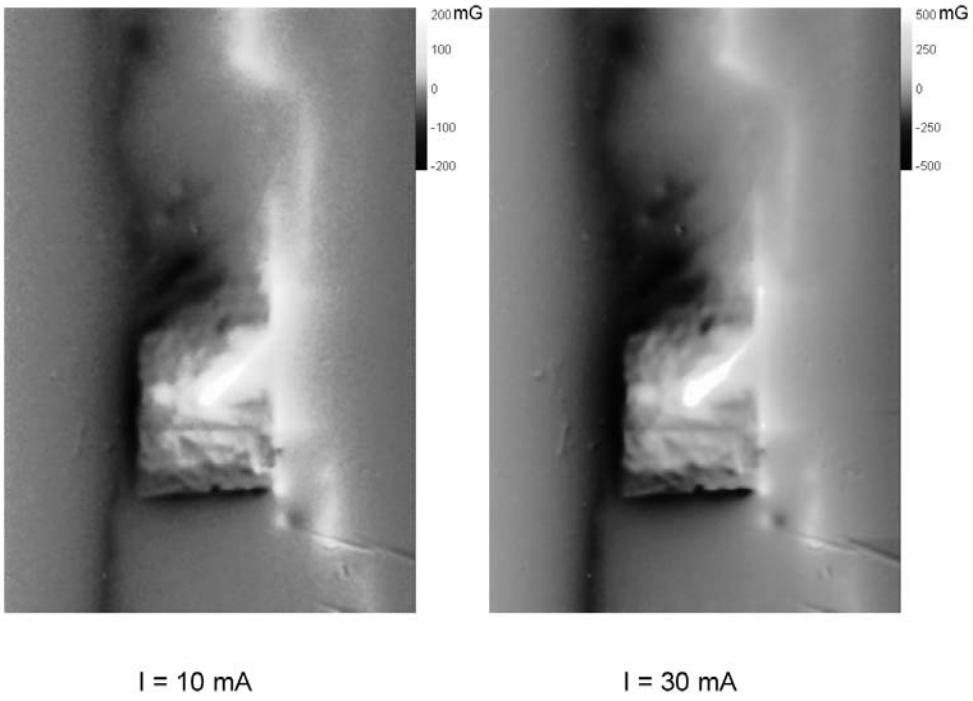

Figure 5.4.3 Images of the self-field generated by current I = 10 and 30 mA at T = 91 K and H_a = 50 Oe.

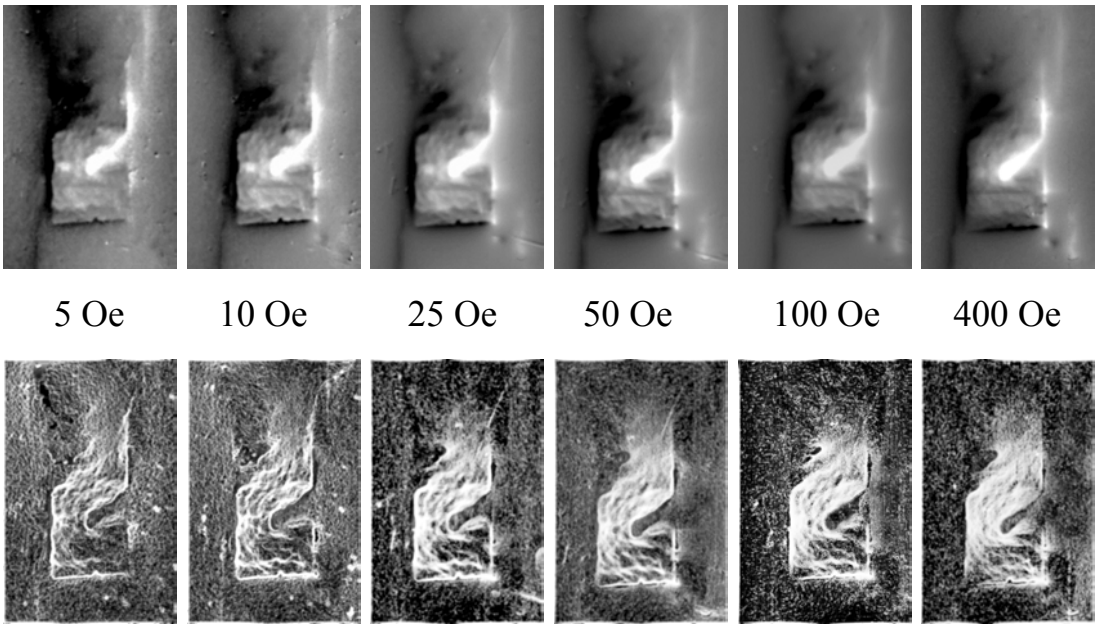

Figure 5.4.4. Images of the self-field and of the calculated current distributions at T = 91 K at various applied magnetic fields, I = 30 mA.

Furthermore, this current redistribution has been observed in a wide range of magnetic fields. Figure 5.4.4 shows the images of the self-field and of the current distribution at $T = 91$ K at various applied magnetic fields between 5 and 400 Oe. The highly non-uniform current flow is clearly seen at all fields. Comparison of the current distribution at different fields demonstrates a pronounced similarity in the flow patterns. The locations of the main current channels are fixed in space and can be found at all images. However some of the additional minor channels are formed only with increasing field and the contrast between the channels fades.

The fixed location of the current channels apparently indicates that crystal inhomogeneity is responsible for the observed current redistribution. As discussed earlier, the presence of disorder results in variation of T_c across the sample. We have estimated the variations of T_c to be of the order of 1 K in this crystal. The resistivity of superconductors exhibits a sharp drop at T_c, as demonstrated in Fig. 5.4.5 where the resistivity of BSCCO crystal is plotted on logarithmic scale versus T at various applied magnetic fields. The measurements were performed simultaneously with MO visualization of the current redistribution. Local variations in T_c of about 1 K may induce significant differences in the resistivity across the crystal. The inset in Fig. 5.4.5 shows the ratio of the resistivities measured at $T = 91.5$ and 90.5 K vs. applied magnetic field. This ratio over 1 K interval may provide an estimate of possible variations in local resistivity due to possible local variations in T_c.

The observed channel formation may apparently reflect differences in the local resistivity across the crystal caused by local variations in T_c. The T_c variations also modify the local lower critical field $H_{c1}(r)$ and the corresponding value of the local penetration field, as discussed in §4.2. In order to find the correlation between the current patterns and T_c variations, we have visualized initial field penetration into the sample. The images of the field penetration have not shown any pronounced features and have not revealed clear correlations between the current patterns and T_c inhomogeneities. Furthermore, the observed current redistribution shows additional puzzling feature. At T_c large fraction of the current flows at the edges. The surface barrier, which may cause edge flow as discussed earlier, is not relevant here and the origin of this current enhancement near the edges is not clear. More work is needed in order to study the details of the revealed phenomenon of non-uniform current flow at T_c.

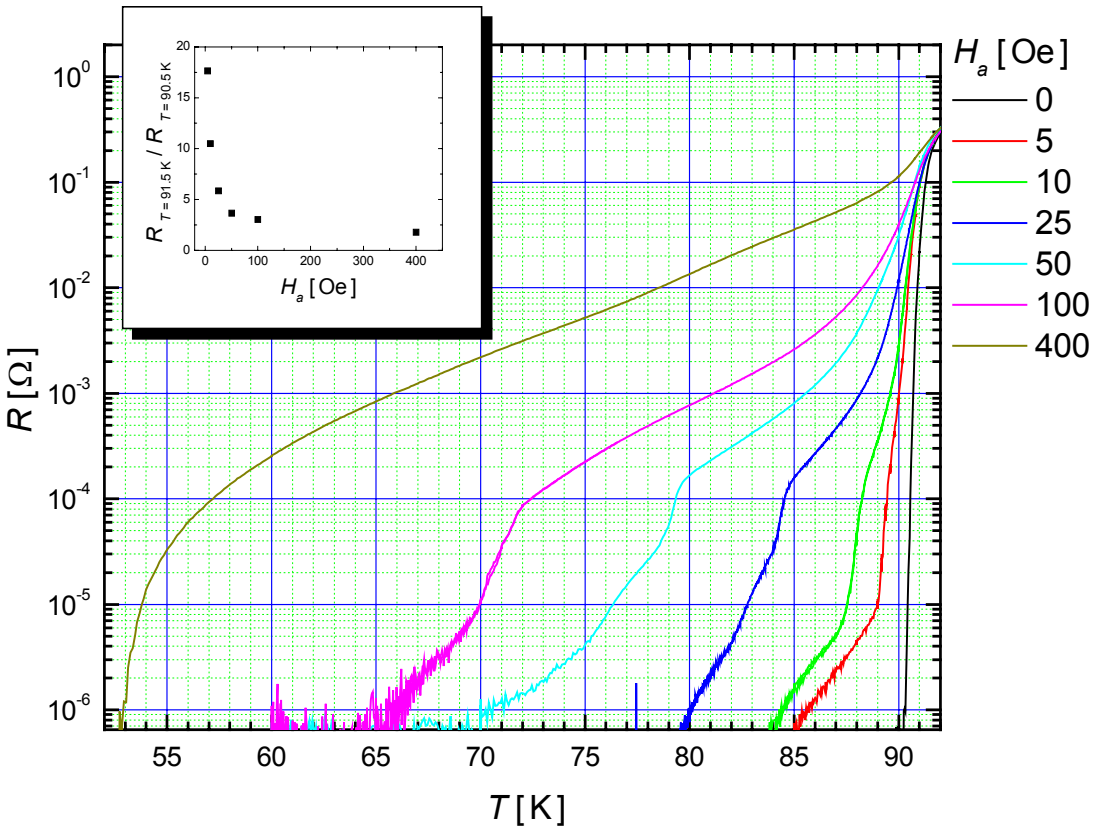

Figure 5.4.5. The resistance of BSCCO crystal is plotted on logarithmic scale vs. temperature at various applied magnetic fields. Inset: The ratio of the resistivities measured at $T = 91.5$ and 90.5 K vs. applied magnetic field.

6. Summary

We have developed a novel differential magneto-optical imaging technique that provides resolution of local magnetic fields as low as 30 mGauss. By use of this technique a direct experimental visualization of the melting process in BSCCO crystals is obtained, revealing the complex behavior of the first-order transition in the presence of disorder. Although locally the melting is found to be of a first order, a global rounding of the transition is observed due to a broad disorder-induced distribution of local melting temperatures down to mesoscopic dimensions. The resulting 'movies' of the melting transition reveal a variety of complicated phenomena, including nucleation, solid-liquid phase separation, pattern formation, as well as interface coarsening, pinning, and instabilities. Furthermore, we have resolved local hysteresis and supercooling of microscopic liquid domains. This non-equilibrium process occurs only at selected sites where the disorder-modified melting temperature has a local maximum. The revealed nucleation process allows for experimental evaluation of the solid-liquid surface tension.

By visualizing the melting process at different points along the melting line we have observed that the melting patterns change significantly with temperature. The scale of the melting patterns is very different and there is little general correlation between the various images. By analyzing the melting patterns at different points along the melting line, we have found that the disorder-induced melting landscape is not constant, and instead a significant variation with temperature and applied magnetic field is observed. This dependence of the melting landscape on H_a and T apparently causes the pronounced variations in the melting patterns along the transition line.

The differential MO imaging of selectively irradiated crystals visualizes the complex propagation of the solid-liquid transition in such crystals. The transition starts in the non-irradiated regions and penetrates into the areas of localized disorder as we increase the field or temperature. The exact nature of the transition depends on the dose of irradiation: the crystals with low dose of irradiation exhibit first-order melting while at high dose the transition apparently turns into a second order.

The differential magneto-optical technique allows two-dimensional visualization of the transport current and reveals complex patterns of the current flow.

The change in the current distribution from uniform to edge flow was demonstrated which occurs due to formation of the surface barriers and enhancement of pinning. In addition, the distortion of the current flow due to presence of inhomogeneities has been observed. We also found an unexpected redistribution of the current flow at the superconductivity transition. The current redistribution was attributed to the variations in T_c across the crystal due to disorder, which induce pronounced changes in the local resistivity, but this issue requires further investigations.

Simultaneous magneto-optical and resistivity measurements show complex correlation between the melting propagation and the drop in the resistivity. The change in the resistivity does not depend only on the propagation of the vortex-lattice melting, but is strongly influenced by the current flow. When the melting occurs at high temperatures and low fields, the current redistribution from uniform to edge flow results in a large resistivity drop at the transition. At lower temperatures and higher fields a significant part of the current flows along the edges even in the liquid phase. Thus the observed current redistribution as well as the resistivity drop is much less pronounced at higher fields. The observed features depend on the applied field and temperature as well as on the geometry of the crystal and the location of electrical contacts.

7. List of Publications

A. Soibel, E. Zeldov, M. Rappaport, Y. Myasoedov, T. Tamegai, S. Ooi, M. Konczykowski, and V. B. Geshkenbein.
Imaging the vortex-lattice melting process in the presence of disorder. *Nature* **406**, 282 (2000).

A. Soibel, M. Rappaport, Y. Myasoedov, S. Banarje, E. Zeldov and T. Tamegai.
Temperature variation of the vortex-lattice melting landscape. Submitted to *Phys. Rev. Lett.*

8. References

[1] Abrikosov, A., *JETP* **5**, 1174 (1957).
[2] Tinkham, M., *Introduction to superconductivity* (McGraw-Hill, Inc, 1996).
[3] Nelson, D. R., *Phys. Rev. Lett.* **60**, 1973 (1988).
[4] Crabtree, G.W. and Nelson, D.R., *Physics Today* **50***,* 38 (1997).
[5] Safar, H. *et al*., *Phys. Rev. Lett.* **69**, 824 (1992).
[6] Kwok, W. K. *et al*., *Phys. Rev. Lett.* **69**, 3370 (1992).
[7] Charalambous, M. *et al*., *Phys. Rev. B*. **45**, 5091 (1992).
[8] Watauchi, S. *et al*., *Physica C* **259**, 373 (1996).
[9] Fuchs, D. T. *et al.*, *Phys. Rev. B*. **54**, R796 (1996).
[10] Zeldov, E. *et al., Nature* **375**, 373 (1995).
[11] Pastoriza, H. *et al., Phys. Rev. B*. **54**, R (1994).
[12] Liang, R. *et al.*, *Phys. Rev. Lett.* **76**, 835 (1996).
[13] Welp, U. *et al.*, *Phys. Rev. Lett.* **76**, 4809 (1996).
[14] Schilling, A. *et al*, *Nature* **382**, 791 (1996).
[15] Roulin, M. *et al.*, *Phys. Rev. Lett.* **80**, 1722 (1998).
[16] Clem, J. R., *Phys. Rev. B* **43,** 7837 (1991).
[17] Lopez, D. *et al.*, *Phys. Rev. Lett.* **76**, 4034 (1996).
[18] Fuchs, D. T. *et al.*, *Phys. Rev. B* **54**, R6156 (1997).
[19] Matsuda, Y. *et al.*, *Phys. Rev. Lett.* **75**, 4512 (1995).
[20] Shibauchi, T. *et al., Phys. Rev. Lett.* **83**, 1010 (1999).
[21] Gaifullin, M. B. *et al., Phys. Rev. Lett.* **84**, 2945 (2000).
[22] Larkin, A. I. and Ovchinikov Yu. N., *J. Low. Temp. Phys.* **34**, 409 (1979).
[23] Fisher M.P.A., *Phys. Rev. Lett.* **62**, 1415 (1989).
[24] Fisher D. S., Fisher M.P.A., and Huse, D. A. *Phys. Rev. B.* **43**, 130 (1991).
[25] Fendrich, J. A. *et al., Phys. Rev. Lett.* **74**, 1210 (1995).
[26] Khaykovich, B. *et al.*, *Phys. Rev. B* **57**, R14088 (1998).
[27] Natterman, T., *Phys. Rev. Lett.* **64**, 2454 (1990).
[28] Giamarchi, T. and Le Doussal, P., *Phys. Rev. Lett.* **72**, 1530 (1994) .
[29] Giamarchi, T. and Le Doussal, P., *Phys. Rev. B* **52**, 1242 (1995).
[30] Nattermann, T. and Scheidl, S., *Advances in physics* **49**, 607 (2000).
[31] Cubitt, R. *et al*., *Nature* **365**, 6445 (1993).
[32] Lee, S. L. *et al*., *Phys. Rev. Lett.* **71**, 3862 (1993).

[33] Kes, P. H. *et al*., *Journal de Physique* **12**, 2327 (1996).

[34] Khaykovich, B. *et al.*, *Phys. Rev. B* **56**, R517 (1997).

[35] Khaykovich, B. *et al*., *Phys. Rev. Lett.* **76**, 2555 (1996).

[36] Imry, Y. and Ma, S.-k., *Phys. Rev. Lett.* **35**, 1399 (1975).

[37] Imry, Y. and Wortis, M., *Phys. Rev. B* **19**, 3580 (1980).

[38] Vinokur, V. *et al*., *Physica C* **295**, 209 (1998).

[39] Ertas, D. and Nelson, D. R., *Physica C* **272**, 79 (1996).

[40] Avraham, N. *et al*., *to be published in Nature*.

[41] For a recent review see: Polyanskii, A. A. *et al*, NATO Science Series 3/72, 353 (Kluwer Academic Publishers, Dordrecht, 1999); Vlasko-Vlasov, V. K. *et al*, Phys. and Mater. Sci. of Vortex States, Flux Pinning, and Dynamics: Proc. of the NATO Adv. Study. Inst., Kusadasi, Turkey, July 26 – Aug. 8, 1998, edited by S. Bose and R. Kossowski (Kluwer, 1999).

[42] Brandt, E. H., *Phys. Rev. B* **46**, 8628 (1992).

[43] Wijngaarden, R. J. *et al*., *Phys. Rev. B* **54**, 6742 (1996).

[44] Wijngaarden, R. J. *et al*., *Physica C,* **295**, 177-85 (1998).

[45] Hardy, V. *et al.*, *Nucl. Instr. Meth. B* **54**, 472 (1991).

[46] Ziegler, J. F., Biersack, J. P. and Littmark, U. *Stopping and Ranges of Ions in Matter*, (Pergamon Press, NY, 1985).

[47] Zeldov E. *et al.*, *Phys. Rev. Lett.* **73**, 1428 (1994).

[48] Morozov, N., *et al.*, *Phys. Rev. B* **54**, R3784 (1996).

[49] Ooi, S. *et al.*, *Physica* C **302**, 339 (1998).

[50] Li, T. W. *et al.*, *J. Cryst. Growth* **135**, 481 (1994).

[51] Landau, L. D. and Lifshitz, E. M. *Statistical Physics*, 3rd ed., (Pergamon Press, Oxford, 1993).

[52] Paulius, C. M *et al.*, *Phys. Rev. B* **61**, R11910 (2000).

[53] Kwok, W. K. *et al.*, *Phys. Rev. Lett.* **84**, 9706 (2000).

[54] Blatter, G. *et al*., *Rev. Mod. Phys.* **66**, 1125 (1994).

[55] Tamegai, T. *et al*., *to be published in Physica C*.

[56] Nelson, D. R. and Vinokur V. M., *Phys. Rev. B* **48**, 13060 (1993).

[57] Landau, L. D., Lifshitz. E. M., and Pitaevskii, L. P., *Electrodynamics of continuous media*, 2nd ed., (Butterworth-Heinenann, Oxford, 1984, p. 194).

[58] Huebener, R. P., *Magnetic Flux Structures in Superconductors,* (Springer-Verlag, Berlin, 1979).

[59] Rae, A.I.M, Forgan, E. M., Doyle, R. A., *Physica* C **301**, 301 (1998).

[60] Doyle, T. B., Labusch, R., and Doyle, R. A., Phys. and Mater. Sci. of Vortex States, Flux Pinning, and Dynamics: Proc. of the NATO Adv. Study Inst., Kusadasi, Turkey, July 26-Aug. 8, 1998, edited by S. Bose and R. Kossowski (Kluwer, 1999).

[61] Fuchs, D. *et al*., *Nature* **391**, 373 (1998).

[62] Fuchs, D. *et al.*, *Phys. Rev. Lett*. **81**, 3944 (1998).

[63] Paltiel, Y. *et al.*, *Phys. Rev. B* **58**, R14763 (1998).
[64] Welp, U. *et al., Nature* **376**, 44 (1995).
[65] Welp, U. *et al.*, *Phys. Rev. Lett*. **76**, 4809 (1996).
[66] Tsuboi, T., Hanaguri, T., and Maeda, A., *Phys. Rev. B* **55**, R8709 (1997).
[67] Fuchs, D. *et al.*, *Phys. Rev. Lett*. **80**, 4971 (1998).